TESIS DE LA UNIVERSIDAD DE ZARAGOZA
2024
46

Diego Sainz De Mena

New tools and methods to inform patient-specific cancer models

Director/es
García Aznar, José Manuel
Pérez Ansón, María Ángeles

ISSN 2254-7606

Prensas de la Universidad
Universidad Zaragoza

ISSN 2254-7606

Universidad Zaragoza
1542

Tesis Doctoral

NEW TOOLS AND METHODS TO INFORM PATIENT-SPECIFIC CANCER MODELS

Autor

Diego Sainz De Mena

Director/es

García Aznar, José Manuel
Pérez Ansón, María Ángeles

UNIVERSIDAD DE ZARAGOZA
Escuela de Doctorado

Programa de Doctorado en Ingeniería Biomédica

2023

New tools and methods to inform patient-specific cancer models

DISSERTATION

submitted in partial fulfillment of the requirements for the degree of

DOCTOR OF PHILOSOPHY

in Biomedical Engineering

by

DIEGO SAINZ DE MENA

Faculty advisors

JOSÉ MANUEL GARCÍA AZNAR
MARÍA ÁNGELES PÉREZ ANSÓN

Department of Mechanical Engineering, University of Zaragoza, Spain

Zaragoza, June 2023

A mis padres

El modo de dar una vez en el clavo es dar cien veces en la herradura.
Miguel de Unamuno

Abstract

Cancer is a major global health challenge that requires the development of innovative tools to improve our understanding and treatment of the disease. Patient-specific modeling has emerged as one of the key techniques in this quest. The field of *in silico* medicine holds great promise for predicting patient-specific cancer progression, treatment response and overall prognosis. However, the development of accurate patient-specific models requires the availability of precise data and an efficient, streamlined process for transforming image data into these models.

This dissertation presents several contributions that improve patient-specific cancer modeling. Primarily, a novel pharmacokinetic model is presented that effectively incorporates diffusion phenomena and allows for the extraction of more accurate data from dynamic contrast-enhanced magnetic resonance sequences. Two innovative methods are proposed to fit this model to the acquired data. The first method, a gradient-based approach, uses the Finite Element Method to compute the gradient semi-analytically, significantly reducing the computational cost compared to other approaches. The proposed alternative method employs Physics Informed Neural Networks to overcome the limitations of the previous method and improve the accuracy of the retrieved parameters.

In addition to the aforementioned model and fitting methods, this research also includes the development of a comprehensive Python library specifically designed to automate the generation of input data for patient-specific models. This library introduces a streamlined workflow that significantly reduces the manual effort required to create patient-specific models from imaging data. By using this Python library, researchers are provided with a straightforward and efficient means of generating the necessary input data, thereby accelerating the modeling process.

In summary, this dissertation provides a significant contribution to the advancement of patient-specific cancer modeling through the introduction of novel tools and methods. The proposed pharmacokinetic model and fitting methods serve as key components in this effort, enabling the extraction of more precise data from dynamic contrast-enhanced magnetic resonance imaging sequences. In addition, the development of a dedicated Python library streamlines and automates the creation of patient-specific input models, simplifying the overall process. Taken together, these contributions provide valuable resources for the field of *in silico* medicine and can help accelerate cancer research efforts.

Resumen

El cáncer es un importante desafío global en salud que requiere el desarrollo de herramientas innovadoras para entender mejor esta enfermedad y mejorar los tratamientos. El modelado de paciente-específico es una de las herramientas clave en esta tarea. El campo de la medicina *in silico* es una de las grandes promesas para predecir la progresión del cáncer en cada paciente, la respuesta al tratamiento y el pronóstico de la enfermedad. Sin embargo, el desarrollo de modelos de paciente-específico necesita de datos precisos y un proceso eficiente y simplificado para incluir los datos obtenidos de imagen médica en estos modelos.

Esta tesis presenta varias aportaciones que contribuyen al desarrollo de modelos de paciente-específico aplicados al cáncer. En primer lugar, se presenta un nuevo modelo farmacocinético que incorpora el proceso de difusión del agente de contraste y permite extraer datos de la vascularización de los tumores más precisos a partir de las secuencias de resonancia magnética dinámica con contraste (DCE, por sus siglas en inglés). Se proponen dos nuevos métodos para ajustar este modelo a los datos adquiridos. El primero de ellos se basa en el método del gradiente y utiliza el método de los elementos finitos para calcular dicho gradiente de manera semianalítica, lo que reduce significativamente el coste computacional del algoritmo. El método alternativo propuesto utiliza redes neuronales informadas por la física (PINNs, por sus siglas en inglés) para superar las limitaciones del método anterior y mejorar la precisión de los parámetros obtenidos con el modelo.

Además del modelo y los algoritmos de ajuste mencionados anteriormente, esta tesis también incluye el desarrollo de una biblioteca en *Python* diseñada para automatizar la generación de datos de entrada para modelos de paciente-específico. En esta biblioteca se ha desarrollado un flujo de trabajo simplificado que reduce significativamente el trabajo manual necesario para crear este tipo de modelos. El objetivo de esta biblioteca es que los investigadores cuenten con un medio sencillo y eficiente para generar los datos de entrada necesarios para sus modelos, facilitando así la creación y desarrollo de nuevas metodologías.

En resumen, esta tesis contribuye al avance del modelado de paciente-específico en el campo del cáncer mediante la introducción de nuevas herramientas y métodos usados en el desarrollo de estos modelos. El modelo farmacocinético propuesto y los métodos de ajuste implementados permiten la extracción de datos más precisos de secuencias de resonancia magnética dinámica con contraste. Además, la biblioteca de *Python* desarrollada agiliza y automatiza la creación de estos modelos. En conjunto, estas contribuciones ofrecen nuevos recursos más eficientes para el campo de la medicina *in silico* y contribuyen a mejorar y acelerar los esfuerzos de investigación del cáncer.

Contents

List of Figures

List of Tables

List of symbols

1D One-Dimensional.

2D Two-Dimensional.

3D Three-Dimensional.

ADC Apparent Diffusion Coefficient.

AIF Arterial Input Function.

CA Contrast Agent.

CVXM Cross-Voxel Exchange Model.

D-ETM Diffusion-Corrected Extended Tofts Model.

DCE Dynamic Contrast Enhanced.

DL Deep Learning.

DP Diffusion-Perfusion.

EES Extravascular Extracellular Space.

ETM Extended Tofts Model.

FE Finite Element.

FEM Finite Element Method.

MRI Magnetic Resonance Imaging.

NN Neural Network.

PDE Partial Derivative Equation.

PINN Physics-Informed Neural Network.

PK Pharmacokinetic.

ROI Region of Interest.

RVE Representative Volume Element.

SI Signal intensity.

STM Standard Tofts Model.

Chapter 1

Introduction

In silico medicine has emerged as a promising tool for developing personalized treatments that can be customized to the specific needs of individual patients [1, 2]. This approach involves using computer simulations to model biological processes and predict how drugs and treatments will interact with the body. By creating virtual models of the human body and its various systems, researchers can test hypotheses and predict outcomes in a virtual environment before conducting clinical trials. This can reduce the cost and time required to bring new treatments to market and enable researchers to optimize existing treatments by identifying patient-specific factors that may affect drug efficacy and toxicity [3, 4].

In silico medicine has emerged as a powerful tool for advancing personalized healthcare. By tailoring medical treatments to the unique genetic, environmental, and lifestyle factors of individual patients, this innovative approach represents a significant departure from the traditional "one-size-fits-all" model of healthcare that assumes all patients with a given condition will respond similarly to the same treatment.

One of the key advantages of *in silico* medicine is its ability to simulate complex biological processes that are difficult or impossible to study *in vivo*. For example, computer simulations can be used to model the interactions between drugs and their molecular targets, as well as the physiological responses of different organs and systems in the body [5]. This can provide valuable insights into the mechanisms of disease and drug action, and can help researchers identify targets for the development of new drugs. *In silico* medicine has already demonstrated its potential in a wide range of applications, from drug development and optimiza-

tion [6] to the design of medical devices [7].

Patient-specific modeling is a key aspect of *in silico* medicine, and involves creating virtual models of individual patients based on their unique anatomy, physiology, and medical history. By using data from medical imaging, genetic testing, and other sources, researchers can create detailed models of individual organs, tissues, and systems, and simulate how these structures and processes interact in response to different treatments and interventions.

Patient-specific modeling has multiple applications in personalized medicine. For example, clinicians can design personalized radiation therapy plans that are optimized for each patient's tumor geometry and radiation sensitivity [8, 9]. Similarly, patient-specific models can be used to design and optimize medical implants and prosthetics, based on the individual anatomy and biomechanics of each patient [10, 11].

One of the most important applications of patient-specific modeling is the study of cancer. Despite the advances achieved in both the diagnosis and treatment of cancer, it remains the second leading cause of death globally, accounting for roughly one-sixth of all deaths [12]. This is due to the intricate and heterogeneous nature of the disease, which is influenced by a wide array of biological and mechanical factors that govern tumor growth, treatment efficacy, and metastasis, among other processes. Thanks to the advances in computational modeling, there has been a significant progress in providing new insights into the complex mechanisms of cancer [13]. These computational models can simulate different processes, from cellular scale to the progression and response to treatments of the whole tumor. Through the analysis of these models, patterns in cancer progression can be identified and risk factors can be better understood. Additionally, computational models can be used to evaluate the effectiveness of current treatments and predict the outcomes of future treatments [14].

Medical imaging plays a crucial role in the development of patient-specific models for cancer, as well as in the diagnosis and monitoring of the disease [15]. These imaging techniques enable clinicians and researchers to visualize the internal structures of the body and identify abnormalities that may indicate the presence of cancer. There are several types of medical imaging modalities, each with its own strengths and limitations. X-ray imaging, for example, is widely used for the detection of bone metastases [16], but in general is not very effective for imaging soft tissues. However, computed tomography (CT) scans provide high-resolution images of both soft and hard tissues, making it an important tool for cancer diagnosis and staging [17].

Magnetic resonance imaging (MRI) is another imaging modality that is commonly used in cancer diagnosis and research. MRI uses a strong magnetic field and radio waves to generate detailed images of internal structures, including organs and tissues. This non-invasive imaging technique is particularly useful for imaging soft tissues, such as the brain [18], liver [19], and prostate [20], among others. There are some advanced modalities that can provide further information about the tissue, such as cell density and blood perfusion. Among these techniques, diffusion weighted (DW) and dynamic contrast-enhanced (DCE) MRI are the most commonly employed to measure tumor properties and to evaluate its response to treatments. In addition, these two methods are used in combination with T1- and T2-weighted sequences in the so-called multiparametric MRI (mpMRI). This imaging modality was first introduced in the 1980s and, thanks to advances in imaging accuracy, has been steadily gaining attention, becoming one of the most commonly used tools in the diagnosis of prostate cancer [21, 22].

DW-MRI measures the Brownian motion of water molecules in a given tissue through the apparent diffusion coefficient (ADC). ADC maps are created by acquiring DWI images at multiple magnetic gradient strengths (known as b-values), which allow for the calculation of ADC values throughout the tissue. This technique can help to accurately identify cancerous lesions and guide treatment planning. In the context of patient-specific modeling, this type of sequence can be used to provide a quantitative measurement of the cellularity of the tumor, which is then used to initialize the mathematical model with patient-specific data.

Dynamic contrast-enhanced MRI (DCE-MRI) is a specialized type of MRI that is used to visualize the blood flow in tissues and organs. Given the importance of this sequence in this dissertation, the next section covers the fundamental aspects of this technique.

1.1 DCE-MRI: Fundamentals and limitations

DCE-MRI studies the way a tissue reacts over time to the introduction of a paramagnetic contrast agent (CA) into the vascular system. To accomplish this, a baseline image is taken before contrast is introduced, followed by a series of images taken over a few minutes during and after the CA arrives in the tissue being studied. These images create a time intensity curve that represents the tissue's response to the CA in terms of enhancement values. Analyzing this curve allows for the extraction of physiological properties such as vessel permeability, vessel surface area, and tissue volume fractions that relate to microvascular blood flow. The basic principle of DCE-MRI is straightforward: as the CA moves through

the tissue, it changes the MR signal intensity (SI) of the tissue based on its local concentration, although this relationship is not linear [23].

To study a region of interest (ROI), MR images are taken every few seconds before, during, and after intravenous injection of the CA. Each image corresponds to one time point, and each pixel generates its own intensity value curve. The variation in SI after injection is determined by tissue vascularization, vessel permeability, vessel surface area, extraction fraction, blood flow, and other factors. This information is used to create parametric maps of specific microvascular biomarkers. Using appropriate mathematical models, absolute values for these parameters can be extracted.

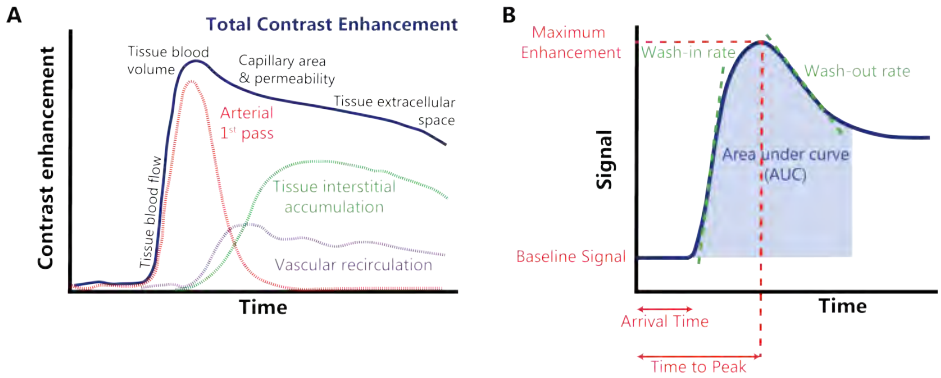

Figure 1.1: Diagram illustrating the morphologic and semi-quantitative analysis of DCE-MRI curves. **A** represents the insights of morphologic analysis. Different parts of the curve are associated with distinct physiological and anatomical features. **B** shows the main parameters extracted from a semi-quantitative analysis. In clinical practice, these variables are used to measure changes in vascularization between different patients (as a diagnostic tool) or between two temporal points for a certain patient (as a prognostic tool to evaluate the efficacy of treatments). Figure adapted from *Questions and answers in MRI*, by A. D. Elster, 2023, www.mriquestions.com

The analysis of DCE data can provide valuable information concerning the vascular status and perfusion. Analysis of the data can be performed using either: simple semi-quantitative methods, analysis of curve morphology or quantitative methods (Figure 1.1). Depending on the analysis method selected, the number of needed measurements vary. If one wants to perform a morphological analysis or a semi-quantitative analysis of the SI curves, it is only necessary to acquire a series of T1-weighted images during the injection of the CA [24, 25]. In case the curves to be analized are the CA concentration versus time curves, a pre-contrast

native T1 image should be acquired before any injection so the SI values can be converted to CA concentration [26]. Finally, for quantitative analysis of the curves it is necessary to perform the steps listed above (with a greater number of images acquired during CA injection) in addition to estimating the arterial input function (AIF).

The AIF represents the concentration of CA in the arterial blood that supplies the tissue of interest. Although in ideal conditions this function should be approximately an impulse function, in reality it differs greatly from this theoretical form. Therefore, it is necessary to estimate somehow this function, either using invasive techniques [27], acquiring it directly from the DCE-MRI dataset [28, 29] or computing an average AIF based on previous studies. Alternative methods that do not require AIF estimation have been also proposed, such as the reference region model [30, 31] or the step input method [32].

As stated below, three main approaches can be followed to analyse DCE-MRI data:

- **Morphologic analysis**: This method is based on a qualitative analysis of the SI curve, classifying it into different types according to the enhancement and relaxation patterns of the curve. This type of analysis is quite limited since it does not give any quantitative estimate of the perfusion parameters [26].

- **Semi-quantitative analysis**: This approach extracts quantitative metrics directly from SI or CA concentration curves. Although these metrics are quite difficult to correlate with physical parameters and are more sensitive than model-based metrics to differences in the acquisition protocols (such as sequence parameters or injection protocols), they have proved their value for assessing tumor angiogenesis [33].

- **Quantitative analysis**: In this case, mathematical models that aim to describe the physical phenomena governing the transport of CA in the tissue are used to fit the CA concentration curves, obtaining quantitative measurements directly related to physical parameters that describe the vascularization of the tissue.

Given its importance, this work will focus on the quantitative analysis of DCE-MRI curves. These mathematical models, known as pharmacokinetic (PK) models, are mostly linear compartmental models. They define a compartment as a theoretical volume in a tissue where CA distributes. The main assumption of

these models is the hypothesis of well-mixed compartments: the concentration of CA is considered homogeneous within each compartment; that is, there are no spatial gradients of CA inside a compartment, there is only a concentration gradient between each compartment.

Although there is a wide variety of compartmental models formulated for DCE-MRI analysis, this dissertation will focus on the most employed models in clinical practice: the standard Tofts model (STM) [34] and the extended Tofts model (ETM) [35]. Both are two-compartment models consisting of a intravascular compartment and an extravascular-extracellular space (EES). They consider that CA can only reach the tissue through blood perfusion, extravasating from the intravascular space to the EES due to the permeability of blood vessels, the vessel surface area, the blood flow, the CA concentration gradient across the vessel endothelium and the volume fractions of each of the compartments. The only difference between the STM and the ETM is that, although both consider the existence of the intravascular compartment, the STM disregards the fraction of volume occupied by this space in relation to the total volume of the voxel, whereas the ETM takes this contribution into account (Figure 1.2). This implies that, while the STM is only accurate in tissues where this hypothesis is valid (poorly vascularized tissues), the ETM increases its range of application, being accurate also in highly vascularized tissues.

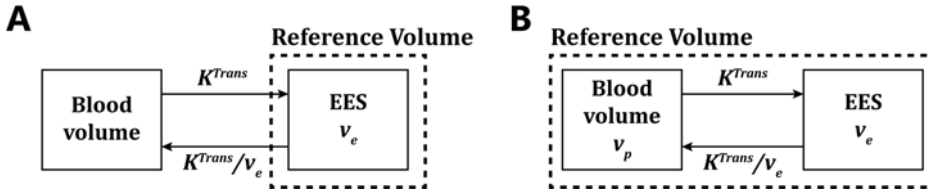

Figure 1.2: Schematic representation of the STM (**A**) and the ETM (**B**). The only difference between both models is the inclusion of the blood volume within the reference volume in the case of the ETM.

A complete review of these models (including their formulation and the definition of their parameters) will be presented in Chapter 2. For now it is sufficient to know that the parameters of these models are the volume fraction occupied by the EES (and that of the intravascular space in the ETM) and the extravasation ratio, known as K^{Trans}, which represents the combination of the permeability of blood vessels, the vessel surface area and the blood flow [36].

While they may appear to be oversimplified models, it should be kept in mind that (for any model in general, but especially in the case of DCE-MRI) increasing

model complexity leads to a detriment in model accuracy. The more parameters that need to be fitted in a model, the more inaccurate and sensitive to noise the model becomes. To compensate for these disadvantages, more sophisticated models require higher quality DCE-MRI data: greater signal to noise ratio, shorter image acquisition interval, etc. Therefore, although these more complex models are capable, for example, of separating the contribution of each of the variables represented by K^{Trans}, their greater complexity significantly reduces their use in clinical practice, where acquisition protocols cannot meet the quality requirements of these models.

Such simplifications and assumptions present certain limitations. Apart from the inherent limitations of quantitative analyses, such as the need to estimate the AIF or the accuracy in converting SI to CA concentration, these models are mainly limited by their considerations regarding CA transport. Recalling the essential parameters of the STM and ETM, it can be seen that K^{Trans} regulates the arrival of CA to the tissue. In other words, these models only consider active transport phenomena by perfusion, neglecting passive phenomena such as diffusion or convection of CA between adjacent voxels (inter-voxel transport). Aditionally, the hypothesis of well-mixed compartments upon which compartmental models are based implies that CA instantenously equilibrates within each compartment, neglecting intra-voxel diffusion of CA. Although this hypothesis may be considered valid for the case of the intravascular compartment, this is not the case for the EES compartment. With an estimated diffusivity coefficient of around 2.6 mm^2/s for gadopentetate dimeglumine (Gd-DTPA) CA [37] and an average voxel size of around 0.5 mm (even larger in clinical studies), it is clear that the time needed to achieve a homogeneous CA concentration is larger than the typical DCE-MRI acquisition scale, around 2 s [38].

The effects of disregarding intra-voxel transport of CA have been studied thoroughly previously in literature [38, 39]. However, since there are no clear solutions to quantify the heterogeneity of CA distribution within a voxel with current protocols and models, this dissertation will focus on inter-voxel transport. Several authors have proposed different formulations and mathematical methods to account for this phenomena. The following section presents a review of all these studies, which constitutes the state of the art in PK models that include passive transport phenomena.

1.1.1 Including passive transport phenomena into PK models

Although both convective and diffusive phenomena can influence the distribution of CA in a tumor, the latter have received notably more attention. Pellerin *et al.* [40] were the first to point out this limitation of conventional PK models and formulated the diffusion-perfusion (DP) model, in which they included a term describing CA diffusion in the STM formulation. In their work, the authors highlighted the limitations of the STM when fitting tumor regions where CA diffusion played an important role, such as the necrotic core observed in some tumors. The main limitations of this model were related to its high computational cost and its formulation of the diffusive term. Later on, Fluckiger *et al.* [41] developed the diffusion compensated Tofts model, which was based on the DP model. They modified the initial formulation to implement a voxel-wise approach to compute the diffusive term. This modification was based on certain assumptions and simplifications, such as homogeneity in cellularity and diffusivity among neighboring voxels, that might not apply to many types of tissues.

Other models proposed by Jia *et al.* [42] and Koh *et al.* [43] accounted for inter-voxel CA diffusion, but lacked information about other physiological properties, such as the extravasation rate or the volume fraction of each compartment.

Cantrell *et al.* [44] proposed a diffusion compensated Tofts model and applied it to intracranial aneurysms. This approach considered a known diffusivity coefficient and handled separately the contributions due to diffusion and to extravasation to reduce the computational cost. Since their method is based on the results obtained from the ETM, which may differ from true values in some tumors where there is significant CA diffusion, the accuracy of this model would be greatly affected in areas where diffusion is relevant.

All these previous approaches understimate the influence of interstitial transport of CA through convection, although this phenomenon may be relevant in some type of tissues [45]. Sourbron [46] developed the theoretical groundwork for a field theory of tracer kinetics by proposing mathematical models that account for various effects, such as convection, diffusion, decay, absorption, and leakage. This theoretical framework is probably the most comprehensive work developed to date for the study of CA transport through mathematical models. This formulation modelled each voxel as a system of multiple interacting tissue compartments, each with its own set of transport parameters, such as velocity and diffusivity, avoiding the well-mixed compartments hypothesis introduced by Tofts. Nevertheless, the high complexity of the model and the inherent limitations of DCE-MRI prevented from using this model on real data. Based on this work,

Sinno *et al.* [47] developed a new model, called the cross-voxel exchange model (CVXM), which includes both diffusive and convective phenomena into the formulation of the STM. In their work, they quantified the error in the parameters retrieved by the STM due to ignoring passive transport mechanisms, showing the importance of convective and diffusive processes in DCE-MRI data. They tested the model both on *in silico* and experimental xenograft data, considering only one-dimensional (1D) geometries.

It should be noted, however, that including convective phenomena increases the complexity of the model. This, as it was previously discussed, negatively affects the accuracy of the model. Despite the good results obtained with the CVXM in 1D geometries, it is to be expected that when moving to two-dimensional (2D) geometries similar to the real ones, the accuracy of the model will decrease and its computational cost will significantly increase.

Since most of the above mentioned models have focused on including diffusive phenomena in the PK models, this dissertation will also focus on that challenge, ignoring possible convective effects due to gradients in interstitial fluid pressure that may affect CA transport.

1.2 Including clinical data in patient-specific models

As it was previously discussed, the importance and necessity of patient-specific models in the study of cancer is becoming increasingly apparent. Despite its many advantages, patient-specific modeling of cancer also has some challenges and limitations that need to be addressed. One of the biggest challenges is the need for precise and reliable data to develop computer simulations. In order to build accurate models of individual patients and predict treatment outcomes, researchers need access to high-quality data from a variety of sources, including medical imaging, genetic testing, and clinical trials. In the specific case of cancer modeling, there is often no genetic information about the patient in their medical history. Typically, medical imaging data are the only data available to build mathematical models of tumor growth. It is clear then, the need to create new models and methods, such as those described in the previous section, that are capable of obtaining quantitative data from the images with much greater precision.

Usually, the task of building mathematical models from clinical data is often tedious and time-consuming. Researchers have to deal with imaging data that may come in different formats. Even when the tumor is already segmented (the ideal situation, although this is frequently not the case), geometry preparation,

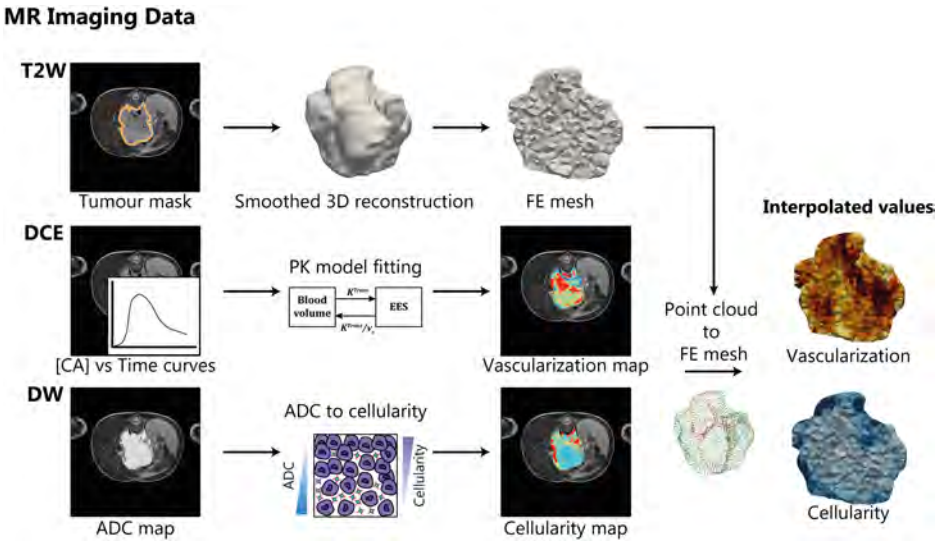

Figure 1.3: Workflow followed to build a patient-specific model of tumor growth from MR imaging data. This workflow assumes that the tumor is already segmented. If it is not the case, a previous segmentation step would be necessary before reconstructing the three-dimensional (3D) geometry. The process of reconstruction and meshing of the geometry often requires the use of different programs and tools, making it very time-consuming to perform this task. Besides, it is common for the tumor segmentation mask and the other sequences (DCE and DW) to have different image formats (DICOM, NIfTI, etc.), which complicates data integration.

finite element (FE) mesh generation and interpolation of the image data to this mesh are rather manual processes that consume considerable resources (Figure 1.3). Chapter 5 introduces a new tool implemented in Python that automates the development of patient-specific models from imaging data.

1.3 Motivation and objectives

The use of DCE-MRI in clinical practice and patient-specific modeling has become increasingly important in recent years. Patient-specific modeling is a powerful tool that enables clinicians to obtain a better understanding of the dynamics of cancer progression and how different therapies affect tumor response. However, the accuracy of patient-specific models heavily relies on the input data used to build them, and inaccurate data can lead to unreliable models.

Previous studies have shown that the commonly used PK models, such as the Standard Tofts Model (STM) and Extended Tofts Model (ETM), may not be accurate when applied to solid tumors where necrotic regions are present. As a result, there is a clear need for new models that incorporate passive transport phenomena and new methods to fit these models to real data. These new methods must be very efficient, minimizing the computational resources needed, while maximizing the accuracy of the model predictions.

In addition to high-quality data, the process of building a patient-specific model that incorporates clinical data is time-consuming and complex. However, the benefits of using patient-specific models in cancer research and treatment make this process necessary. These models provide clinicians with personalized information that can guide treatment decisions and improve patient outcomes.

To facilitate the creation of patient-specific models, new automated tools that deal with the preprocessing and preparation of clinical data are needed. These tools would minimize the time and effort required to develop a model, making patient-specific modeling a more feasible approach for clinical practice.

This dissertation has been developed within the context of the European PRIMAGE (PRedictive In-silico Multiscale Analytics to support cancer personalized diaGnosis and prognosis, Empowered by imaging biomarkers) Project [48]. PRIMAGE is currently one of the largest and more ambitious European research projects in medical imaging, artificial intelligence and childhood cancer, in particular, Neuroblastoma (NB) and the Diffuse Intrinsic Pontine Glioma (DIPG). Its main goal is to develop a decision support system combining retrospective clinical information and incorporating it into the diagnostic pipeline using AI and computational models.

Within this project, several patient-specific models have been developed to simulate the evolution of the tumor and predict its outcome [14, 49–51]. These models have been based primarily on the available MR images, which included tumor segmentations and DCE and DW sequences for each tumor. During the process of generating these models, the previously mentioned needs were identified (higher data quality and tools to automate the creation of the models), so we focused our efforts on solving these needs.

The first objective of this dissertation is, therefore, to develop new models that incorporate passive transport phenomena and to implement new methods to fit these models to DCE-MRI data accurately, obtaining high quality data that can be used in the tumor growth models. To this end, the formulation of a new PK model was first developed. Then, two different strategies have been devel-

oped to fit this new model to DCE-MRI sequences: the first one is based on the gradient descent method and the Finite Element Method (FEM), computing the Jacobian matrix through a semi-analytical approach. To overcome the limitations of this first method, an alternative approach based on Deep Learning (DL) was developed.

Additionally, the second goal of this dissertation is to create an automated tool to facilitate the creation of patient-specific models from clinical data, thereby improving the efficiency and accuracy of the modeling process.

By developing these new methods, this work aims to contribute to the field of patient-specific modeling and ultimately improve our understanding of tumor physiology, leading to better treatment outcomes for cancer patients.

1.4 Outline

This chapter presents some of the challenges faced in patient-specific modeling, including data quality and automatization of model development. More specifically, this chapter presents some key concepts and the state of the art that will serve as the basis for the next chapters.

- Chapter 2 presents the formulation of a new PK model based on the ETM that includes the phenomenon of CA diffusion based on the concept of effective diffusivity. This new model, named diffusion-corrected ETM (D-ETM), is the basis for the work presented in Chapters 3 and 4.

- In Chapter 3, a new inverse method based on the FE method (FEM) is developed to fit the D-ETM to the curves obtained from DCE-MRI sequences. This new method is tested on *in silico* cases that resemble clinical data.

- Chapter 4 describes a new alternative method to the one developed in Chapter 3. This approach makes use of a type of neural networks (NNs), called Physics-Informed Neural Networks (PINNs), to solve the inverse problem posed in the previous chapter, overcoming the limitations of the previous FE-based method on the 1D synthetic cases tested.

- Chapter 5 introduces a new Python library that automates the process of generating patient-specific models based on medical imaging data. Furthermore, an example of use is shown based on one of the cases of the PRIMAGE project in which this dissertation is framed.

- Finally, Chapter 6 summarizes the main results of this dissertation and describes the future lines of research that arise from this work.

Chapter 2

A new model to integrate diffusion into the Extended Tofts Model

This chapter is based on:

D. Sainz-DeMena et al. "A finite element based optimization algorithm to include diffusion into the analysis of DCE-MRI". in: *Engineering with Computers* 38.5 (Oct. 2022), pp. 3849–3865

2.1 Introduction

Dynamic contrast-enhanced magnetic resonance imaging (DCE-MRI) has long been used as a clinical tool to study the vasculature of different tissues, especially tumors. Recently, it has been employed to assess the efficacy of antiangiogenic treatments in tumors [53–55]. In summary, this technique consists on the acquisition of a series of T1-weighted images before, during, and after the intravenous injection of a CA. As the CA reaches the tissue of interest via arterial inflow, it decreases the native T1 relaxation time, producing an increase in the measured SI. The following removal of CA through venous blood flow results in a decrease in SI, returning to its baseline value. For each voxel, the outcome is a SI versus time curve. [56]. To fit any PK model it is necessary, as we have seen previously, to first convert these SI curves to CA concentration. This conversion can be done considering either linear or non-linear equations [57].

As we previously discussed, we will focus on the compartmental models developed by Tofts *et al.* [34, 35], given their importance in clinical practice [58]. These models assume that CA can only reach the ROI through blood perfusion, neglecting passive delivery. As several authors have pointed out [40–44, 46, 47], assuming no inter-voxel CA diffusion can lead to errors in the quantities estimated by the model, especially in weakly vascularized zones, such as necrotic regions in a tumor. Even though convective effects due to gradients in the interstitial fluid pressure may be relevant in some tissues, they will not be considered to reduce the complexity of the model.

These authors have proposed different models and fitting algorithms to include diffusive phenomena in Toft's compartmental models. Nonetheless, all of them present certain limitations: some did not obtain parameters describing vascularization [42, 43]; others assumed some hypotheses that limited the applicability of the model [41, 44] and the most complex and yet more accurate DP and CVXM models [40, 47], entailed an excessive computational cost.

Except Cantrell *et al.* [44], other authors based their works on the STM, which is only accurate in poorly vascularized tissues [59]. In order to extend the range of application of the diffusion-corrected models, we present a new formulation of diffusion-corrected CA transport based on the ETM, which is accurate on both weakly and highly vascularized regions.

2.2 Diffusion-corrected extended Tofts model (D-ETM)

The transport mechanisms in biological tissues have long been of interest among physicians and researchers. Nicholson and collaborators [60–65] studied thoroughly this process, establishing a general formulation for the diffusion of particles in the brain [62]. In this work, they compared the densely packed cells of the brain and their interstitial spaces to a porous medium with two phases, an intra- and extracellular phase. They then formulated the equations of the diffusive process in brain based on the general equation of diffusion in porous media, which is a process that has also been widely studied by many authors [66–68].

In the present work, this diffusion formulation is added to the general form of the ETM. There is a distinction between two different scales: a macro-scale, where the extravasation contribution to the concentration averaged in the representative volume element (RVE) as well as the diffusion of CA between adjacent RVEs are studied (Figure 2.1B); and the micro-scale, which is defined within the RVE and consists of a heterogeneous distribution of cells, vessels and EES (Figure 2.1A). The size of the RVE must be large enough to achieve length scale separation, containing sufficient number of cells and, at the same time, it must be small enough so that CA concentration can be averaged in it without adding significant error. Therefore, equation 2.1 describes the main transport mechanisms for a RVE:

$$\begin{aligned} \frac{\partial \overline{C_t}(\boldsymbol{x},t)}{\partial t} &= \boldsymbol{\nabla}\cdot\left(D_{eff}(\boldsymbol{x})\nabla\overline{C_t}(\boldsymbol{x},t)\right) \\ +K^{Trans}(\boldsymbol{x})\left(C_p(t)-\overline{C_e}(\boldsymbol{x},t)\right) &+ v_p(\boldsymbol{x})\frac{\mathrm{d}C_p(t)}{\mathrm{d}t} \end{aligned} \tag{2.1}$$

where:

- $\overline{C_t}(\boldsymbol{x},t)$ is the total CA concentration, averaged in the RVE (V_T)

$$\overline{C_t}(\boldsymbol{x},t) = \frac{1}{V_T}\int_{V_T} C_t(\boldsymbol{X},\boldsymbol{x},t)dV \tag{2.2}$$

  From now on, we will refer to $\overline{C_t}(\boldsymbol{x},t)$ as $C_t(\boldsymbol{x},t)$ in order to facilitate the formulation

- $\boldsymbol{x}$ is the coordinates vector in the macroscopic domain of the tissue

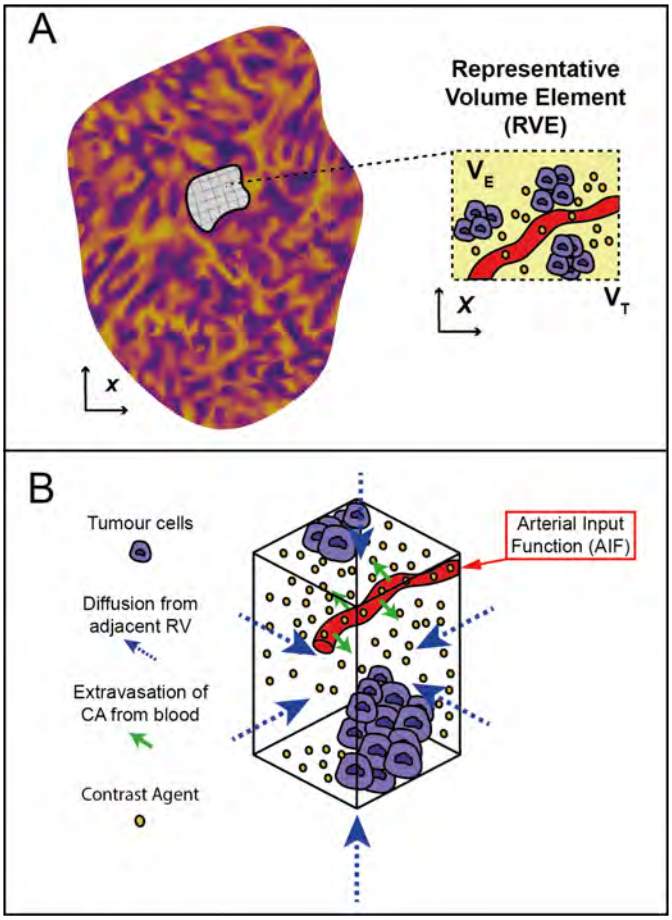

Figure 2.1: **A**. Insight on the different scales considered in the model. The RVE consists of a certain volume occupied by cells, another region which corresponds to the microvasculature and the rest of the volume (colored in light yellow), which is the EES (V_E). The concentration of CA within the EES volume of the RVE is averaged (equation 2.3). The two different coordinate systems ($\boldsymbol{x}$ and $\boldsymbol{X}$) are detailed.
B. Different processes taking place in the RVE (V_T) that are considered in the proposed model. Apart from the perfusion process (solid green arrows) and the contribution of microvasculature to the total concentration, diffusion between adjacent RVEs (dotted blue arrows) is included.

- $\boldsymbol{X}$ is the coordinates vector in the microscopic domain of the RVE

  The relation between the macroscopic ($\boldsymbol{x}$) and the microscopic ($\boldsymbol{X}$) coordinate systems is defined through the homogenization process defined in equations 2.2 and 2.3

- $D_{eff}(\boldsymbol{x})$ is the effective diffusion coefficient for that RVE. Considering that each RVE contains a heterogeneous distribution of cells and vessels, we can compare the diffusive process of CA to the diffusion in a porous medium, as stated previously [62, 65–69]. A further detailed study of this variable is included below (section 2.2.1)

- $K^{Trans}(\boldsymbol{x})$ is the extravasation rate for that RVE

- v_p $(\boldsymbol{x})$ is the volume fraction of blood plasma in the RVE

- $C_p(t)$ is the CA concentration in the blood plasma volume, which follows the same temporal function in every RVE and only varies with time

- $\overline{C_e}(\boldsymbol{x},t)$ is the averaged CA concentration in the extracellular subvolume (V_E) of the RVE. Considering that the microscopic scale is unknown (we have no information about the subvolume V_E of the RVE), we assume the hypothesis of well-mixed compartments presented by Tofts [35]. This hypothesis considers an infinite diffusivity coefficient of CA in the subvolume V_E, what implies that there cannot be any spatial gradient of C_e in the subvolume V_E. Therefore:

$$\overline{C_e}(\boldsymbol{x},t) = \frac{1}{V_E}\int_{V_E} C_e(\boldsymbol{X},\boldsymbol{x},t)dV \tag{2.3}$$

  From now on, we will refer to $\overline{C_e}(\boldsymbol{x},t)$ as $C_e(\boldsymbol{x},t)$ in order to facilitate the understanding of the equations

This well-mixed compartments hypothesis validates the Tofts equation for the compartmental model:

$$C_t(\boldsymbol{x},t) = v_e(\boldsymbol{x})C_e(\boldsymbol{x},t) + v_p(\boldsymbol{x})C_p(t) \tag{2.4}$$

where $v_e(\boldsymbol{x})$ is the volume fraction of the EES in the RVE, defined as $v_e = \frac{V_E}{V_T}$.

Substituting equation 2.4 in equation 2.1, we obtain equation 2.5, which is the general form of the diffusion-corrected ETM (D-ETM), formulated in terms of the

total concentration in the RVE:

$$\frac{\partial C_t(\boldsymbol{x},t)}{\partial t} = \boldsymbol{\nabla} \cdot (D_{eff}(\boldsymbol{x}) \nabla C_t(\boldsymbol{x},t)) + \frac{K^{Trans}}{v_e}(\boldsymbol{x}) \left(C_p(t)(v_e(\boldsymbol{x}) + v_p(\boldsymbol{x})) - C_t(\boldsymbol{x},t)\right) + v_p(\boldsymbol{x}) \frac{\mathrm{d}C_p(t)}{\mathrm{d}t} \tag{2.5}$$

Table 2.1 summarizes all model parameters, their definition and units. Note that although K^{Trans} is measured in s^{-1} in the model, results presented in Chapter 3 and Chapter 4 are shown in min^{-1} to facilitate its comparison with the literature [34, 40, 41, 44, 47].

Table 2.1: List of model parameters and their units.

Parameter	Definition	Units
C_t	Total CA concentration in the RVE	mM/mm^3
C_e	CA concentration in the EES volume within the RVE	mM/mm^3
C_p	CA concentration in blood plasma	mM/mm^3
K^{Trans}	Extravasation rate of CA from blood plasma to the EES	$1/s$
v_e	Volume fraction of EES within the RVE	1
v_p	Volume fraction of plasma within the RVE	1
D_{eff}	Effective diffusion coefficient	mm^2/s
D	Diffusion coefficient in free medium	mm^2/s

2.2.1 Effective diffusivity

Different authors have formulated equations that relate the effective diffusivity to different geometrical characteristics of the porous material [69–71]. Given that the geometrical structure of the solid phase (cells and vessels) is unknown, we assume that the equivalent diffusivity is related to the tortuosity [62]. Tortuosity (λ) quantifies the increase in path-length of a diffusing particle due to the existence of obstacles in its way [72], as shown in Figure 2.2. It is defined as:

$$\lambda = \sqrt{\frac{D}{D_{eff}}} \tag{2.6}$$

Tao and Nicholson [65] used the Monte Carlo method to simulate the diffusion of particles on different porous structures and different cell geometries and fitted the simulated data to obtain the value of D_{eff} for each case. Applying equation 2.6

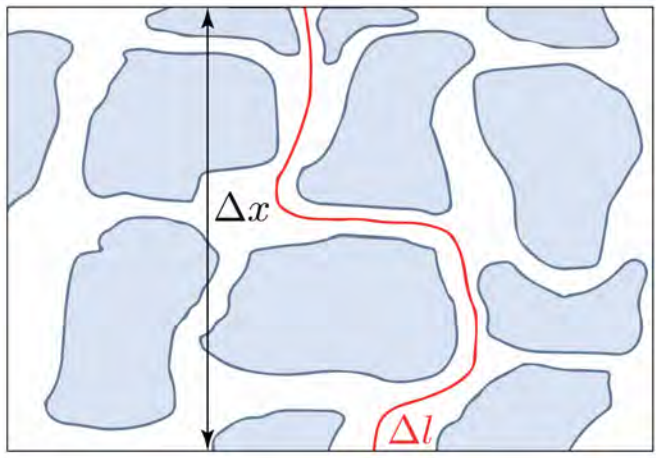

Figure 2.2: Diffusion path of a CA molecule within the tissue. Shapes in blue represent clusters of cells, while the red line corresponds to the path followed by the CA molecule. Tortuosity can be defined as the ratio of the actual distance (Δl) travelled by the species per unit length of the medium (Δx).

to these values, they obtained a value of tortuosity (λ) for each simulated structure and cell geometry and found that tortuosity was independent on the considered cell geometry and was only dependent on the porosity (ε) of the structure:

$$\lambda = \sqrt{\frac{3 - \mathcal{E}}{2}} \tag{2.7}$$

Substituting equation 2.7 in equation 2.6 we obtain the definition of the equivalent diffusivity (D_{eff}). Considering that porosity (ε) is defined as the volume fraction of "empty" space in the material, its equivalence to v_e is straightforward:

$$D_{eff} = \frac{2D}{3 - v_e} \tag{2.8}$$

Where D is the diffusion coefficient of CA in free medium, which is known. Using this formulation, we can consider different effective diffusion coefficients per element without adding more unknowns to the model.

2.3 Conclusion

All the previous works mentioned above follow the same formulation of the diffusive term (revised thoroughly in [40]). This formulation assumes that CA can diffuse freely through each of the voxel faces (this means that no obstacles, such as cells, are present in that faces). Depending on the cellularity level and the voxel size, this assumption may not be valid. The latest contribution by Sinno *et al.* [47] proposes a modified formulation of the diffusive term that, as well as the formulation presented in this work, avoids this simplification. In their work, the diffusivity coefficient is considered unknown but constant through the domain. As stated previously, this hypothesis may not be valid for some tissues, especially in tumor tissues, which are characterized by their strong heterogeneity.

The formulation of the diffusion process here proposed avoids this assumption by embracing the concept of effective diffusivity [62]. This concept implies that the diffusion of agents within biological tissues is similar to the diffusion of an agent in a porous medium [66–68]. Apart from providing a more accurate description of the diffusive process, this hypothesis links the effective diffusivity to the volume fraction of the EES (v_e), avoiding the generation of a new parameter (D) that needs to be fitted or extracted from data or literature, as it is the case in previous works [40, 41, 43, 44, 47].

Chapter 3

A Finite Element-based optimization algorithm for fitting the D-ETM to DCE-MRI data

This chapter is based on:

D. Sainz-DeMena et al. "A finite element based optimization algorithm to include diffusion into the analysis of DCE-MRI". in: *Engineering with Computers* 38.5 (Oct. 2022), pp. 3849–3865

3.1 Introduction

In the previous chapter, the D-ETM was introduced as a new PK model for analyzing DCE-MRI data that takes into account the effects of passive transport on the diffusion of CA within the tumor tissue. Fitting the D-ETM to DCE-MRI data requires solving an inverse problem that involves fitting a partial differential equation (PDE) to the data from all voxels in an image simultaneously. This presents a significant computational challenge due to the large number of parameters and the complexity of the PDE.

Various optimization methods are available to tackle this problem, including gradient-based, genetic algorithms [73], Bayesian optimization [74] or the simulated annealing algorithm presented in [40], among others. Gradient-based methods are particularly attractive due to their efficiency and effectiveness, relying on the calculation of the gradient of the objective function with respect to the model parameters. The gradient provides information on the direction of steepest descent and can be used to iteratively update the model parameters until convergence to a local minimum is achieved.

Although gradient-based methods present some limitations that should be considered, such as convergence to local minima, they can outperform other stochastic approaches in terms of speed if an efficient algorithm for computing the gradient is chosen. Given the complexity and non-linearity of the PDE in Eq. 2.5, we cannot obtain the gradient analytically, so we must use numerical methods, such as the finite difference method. This method, although being suitable for complex equations, requires a forward simulation of the problem for each parameter in each RVE. The computational cost associated with this method is unaffordable. To overcome these limitations, we describe here an alternative method for the gradient computation based on the FEM that retrieves the exact gradient and performs well on complex equations.

In this chapter we propose a FE-based implementation of the D-ETM to solve the inverse problem that arises when fitting any PK model to DCE-MRI curves. To achieve this aim, we first describe the implementation of the D-ETM using the FEM. Second, we develop a gradient-based optimization method to fit this model to the clinical imaging data to extract vascular properties. And third, we test the performance and accuracy of this inverse method in different simulated theoretical cases. Hence, this approach aims to benefit from the computational efficiency of the FEM to fit all analyzed volumes simultaneously while keeping an affordable computational cost. Thus, the modeling approach here proposed can be applied to analyze the heterogeneous behavior characteristic of tumors,

avoiding simplifications and approximations that reduce the range of application of the model.

3.2 Forward FE model

Equation 2.5 is implemented into *ANSYS* (Ansys Inc., TX, USA) diffusion module [75], including the extravasation term and the contribution of the blood plasma fraction as non-linear generation terms.

The numerical formulation obtained for equation 2.5 is defined as:

$$\boldsymbol{C_e^d}\dot{\boldsymbol{c}}_{\boldsymbol{e}} + \boldsymbol{K_e^d c_e} = \boldsymbol{r_e^g} \tag{3.1}$$

Where, for an element e:

- $\boldsymbol{c_e}$ is the nodal concentration vector and $\dot{\boldsymbol{c}}_{\boldsymbol{e}}$ is its temporal derivative
- $\boldsymbol{C_e^d}$ is the element diffusion damping matrix and it is defined as:

$$\boldsymbol{C_e^d} = \int_{\Omega^e} \boldsymbol{n}\boldsymbol{n}^T \, d(\Omega^e) \tag{3.2}$$

- $\boldsymbol{n}$ are the element shape functions
- $\boldsymbol{K_e^d}$ is the element diffusion conductivity matrix and it is defined as:

$$\boldsymbol{K_e^d} = \int_{\Omega^e} \left(\nabla \boldsymbol{n}^T\right)^T \boldsymbol{D} \nabla \boldsymbol{n}^T \, d(\Omega^e) \tag{3.3}$$

  where $\boldsymbol{D}$ is the diffusion coefficient matrix, further defined

- $\boldsymbol{r_e^g}$ is the element diffusing substance generation load vector and it is defined as:

$$\boldsymbol{r_e^g} = \int_{\Omega^e} \boldsymbol{g}\boldsymbol{n}^T \, d(\Omega^e) \tag{3.4}$$

  where $\boldsymbol{g}$ is the generation load vector

  The integration volume Ω^e corresponds to the volume of the finite element e.

The time discretization scheme is derived from the backward Euler implicit method and is defined as:

$$\boldsymbol{u_{n+1}} = \boldsymbol{u_n} + \theta \Delta t \, \dot{\boldsymbol{u}}_{\boldsymbol{n+1}} + (1-\theta)\, \Delta t \, \dot{\boldsymbol{u}}_{\boldsymbol{n}} \tag{3.5}$$

Where:

- $\boldsymbol{u_n}$ is the nodal degree of freedom (DOF) values at time t_n
- θ is the transient integration parameter. If $\theta = 0$ an explicit algorithm is used, whereas if $\theta = 1$ an implicit algorithm is employed
- $\Delta t = t_{n+1} - t_n$ is the time step size
- $\dot{\boldsymbol{u}}_{\boldsymbol{n}}$ is the time rate of the nodal DOF values at time t_n, computed at previous time point

Implementing this time discretization scheme on equation 3.1 leads to equation 3.6:

$$\begin{aligned} \boldsymbol{C^d} \frac{\boldsymbol{c^{t+1}} - \boldsymbol{c^t}}{\Delta t} = -\boldsymbol{K^d c^{t+1}} + \boldsymbol{R}\left((\boldsymbol{k^{Trans}} \oslash \boldsymbol{v_e}) \odot (\boldsymbol{v_e} + \boldsymbol{v_p}) c_p^{t+1} \right) \\ -\boldsymbol{R}\left((\boldsymbol{k^{Trans}} \oslash \boldsymbol{v_e}) \odot \boldsymbol{c^{t+1}} \right) + \boldsymbol{R v_p} \dot{c_p}^{t+1} \end{aligned} \tag{3.6}$$

Where $\boldsymbol{R}$ is the substance generation matrix and $\boldsymbol{K^d}$ is the assembled diffusion conductivity matrix. The terms $\boldsymbol{c^{t+1}}$ and $\boldsymbol{c^t}$ are the nodal concentration vectors resulting from evaluating the nodal concentration matrix ($\boldsymbol{C}$) at given time points. $\boldsymbol{k^{Trans}}$, $\boldsymbol{v_e}$ and $\boldsymbol{v_p}$ are the nodal variables vectors. Finally, c_p^{t+1} and $\dot{c_p}^{t+1}$ are the scalars resulting of evaluating the AIF and the derivative of the AIF vectors ($\boldsymbol{c_p}$ and $\dot{\boldsymbol{c_p}}$) at given time points. To distinguish between the regular dot product and the Hadamard operations, we employ a specific notation for the pointwise product ($\odot$) and division ($\oslash$). The diffusion coefficients matrix $\boldsymbol{D}$ for each element is:

$$\begin{bmatrix} \frac{2D_{xx}}{3-v_e^{elem}} & 0 & 0 \\ 0 & \frac{2D_{yy}}{3-v_e^{elem}} & 0 \\ 0 & 0 & \frac{2D_{zz}}{3-v_e^{elem}} \end{bmatrix}$$

Where ${v_e}^{elem}$ is the element average of the nodal v_e variable. Considering as a first approach isotropic diffusion, $D_{xx} = D_{yy} = D_{zz} = D$.

Due to the dynamic nature of the physical process, transient effects were included. Although the transient integration parameter was set to θ = 1, which makes the solution unconditionally stable, the influence of the transient effects still affected the accuracy of the solution depending on the time step (Δt). We conducted several experimental error analyses and concluded that a time step of 1s ensured the consistency of the solution, while keeping an affordable computational cost.

Initial values were provided to initialize the transient simulations. Both the nodal concentration and its time derivative were set to zero for t=0s ($C(t_0) = \dot{C}(t_0) = 0$).

The AIF is interpolated to match this time resolution. Since both generated curves and fitted curves are obtained using the same FE model, no interpolation is needed to perform the fitting process.

Regarding the boundary conditions, we assumed that no CA could diffuse across the boundaries of the geometry, considering the tumor as an "isolated" entity with respect to adjacent tissues. Although it may not be biologically correct for tissues that are not surrounded by physical barriers, this condition facilitates the formulation and is consistent with literature [34, 35, 40, 41].

3.3 Solving the inverse problem

Imaging data is usually processed as a voxelized geometry. However, the method proposed here can be applied to any complex geometry, like those obtained from imaging segmentation. Converting the data from a voxelized discretization to a FE mesh involves an approximation of this data. However, since the spatial resolution of the latter is expected to be equal to or higher than the spatial resolution of the former, the error added to the data due to this approximation is small.

After implementing the D-ETM equation in *ANSYS*, we can simulate the CA transport for a certain tissue. Therefore, the next step is fitting the model to the concentration-time curves obtained from imaging. This inverse problem of curve fitting is solved using an iterative method based on the non-linear least squares method [76].

Being a gradient based method, it needs to compute the derivative of the total concentration $C(t)$ with respect to each nodal parameter, known as the Jacobian matrix.

Typically, this matrix is obtained by using the numerical methods such as the

finite differences method. This option leads to an excessively high computational cost, since the number of simulations (N_{sim}) needed to compute this matrix increases linearly with the number of time points and nodal variables and quadratically with the number of nodes.

$$N_{sim} = {N_{nodes}}^2 N_{time} N_{parameters} \tag{3.7}$$

where N_{nodes} is the number of nodes in the model, N_{time} is the number of time points and $N_{parameters}$ is the number of unknowns to be fitted per node. Even for small cases, this numerical analysis requires an excessive computational cost that cannot be considered.

Therefore, we propose an alternative semi-analytical computation of the Jacobian matrix. We can re-write equation 3.6 as:

$$\boldsymbol{A}\boldsymbol{c}^{\boldsymbol{t+1}} = \Delta t\, \boldsymbol{R}\left((\boldsymbol{k}^{\boldsymbol{Trans}} \oslash \boldsymbol{v_e}) \odot (\boldsymbol{v_e} + \boldsymbol{v_p}) c_p^{t+1} + \boldsymbol{v_p} \dot{c_p}^{t+1}\right) + \boldsymbol{C}^{\boldsymbol{d}}\boldsymbol{c}^{\boldsymbol{t}} \tag{3.8}$$

where:

$$\boldsymbol{A} = \boldsymbol{C}^{\boldsymbol{d}} + \Delta t\, \boldsymbol{K}^{\boldsymbol{d}} + \Delta t\, \boldsymbol{R}(\boldsymbol{k}^{\boldsymbol{Trans}} \oslash \boldsymbol{v_e}) \tag{3.9}$$

The derivative of $\boldsymbol{C}$ with respect to the different parameters can be obtained from equation 3.8 by applying the product rule on the left hand side of the equation:

- For K^{Trans}:

$$\boldsymbol{A}\frac{\partial \boldsymbol{c}^{\boldsymbol{t+1}}}{\partial \boldsymbol{k}^{\boldsymbol{Trans}}} = \Delta t\, \boldsymbol{R} \odot \left(c_p^{t+1}(\boldsymbol{v_e} + \boldsymbol{v_p}) \oslash \boldsymbol{v_e} - \boldsymbol{c}^{\boldsymbol{t+1}} \oslash \boldsymbol{v_e}\right) + \boldsymbol{C}^{\boldsymbol{d}}\frac{\partial \boldsymbol{c}^{\boldsymbol{t}}}{\partial \boldsymbol{k}^{\boldsymbol{Trans}}} \tag{3.10}$$

- For v_e:

$$\boldsymbol{A}\frac{\partial \boldsymbol{c}^{\boldsymbol{t+1}}}{\partial \boldsymbol{v_e}} = -\Delta t\, \boldsymbol{K}^{\boldsymbol{d}}(\boldsymbol{v_e}) \odot \boldsymbol{c}^{\boldsymbol{t+1}} + \Delta t\, \left(\boldsymbol{R} \odot (\boldsymbol{k}^{\boldsymbol{Trans}} \oslash \boldsymbol{v_e}^2) \odot \boldsymbol{c}^{\boldsymbol{t+1}} - \boldsymbol{v_p} c_p^{t+1}\right) + \boldsymbol{C}^{\boldsymbol{d}}\frac{\partial \boldsymbol{c}^{\boldsymbol{t}}}{\partial \boldsymbol{v_e}} \tag{3.11}$$

  where $\boldsymbol{K}^{\boldsymbol{d}}(\boldsymbol{v_e}) = \frac{\partial \boldsymbol{K}^{\boldsymbol{d}}}{\partial v_e}$. $\boldsymbol{K}^{\boldsymbol{d}}$ is the assembled matrix of elemental diffusion conductivity matrices, which are defined by equation 3.3. To build these matrices, we define $\boldsymbol{D}$ as:

$$\begin{bmatrix} \frac{2D}{(3-{v_e}^e)} & 0 & 0 \\ 0 & \frac{2D}{(3-{v_e}^e)} & 0 \\ 0 & 0 & \frac{2D}{(3-{v_e}^e)} \end{bmatrix}$$

Where, for an element e, ${v_e}^e = \frac{1}{N}\sum_{i=0}^{N} {v_e}^i$. N is the number of nodes in the element and ${v_e}^i$ are the nodal values of v_e. The derivative of $\boldsymbol{K_e^d}$ with respect to nodal v_e ($\boldsymbol{K_e^d(v_e)}$) is exported from *ANSYS* by deriving the components of $\boldsymbol{D}$ with respect to the nodal v_e values, obtaining:

$$\begin{bmatrix} \frac{-2D}{N(3-\frac{1}{N}\sum_{i=0}^{N} {v_e}^i)^2} & 0 & 0 \\ 0 & \frac{-2D}{N(3-\frac{1}{N}\sum_{i=0}^{N} {v_e}^i)^2} & 0 \\ 0 & 0 & \frac{-2D}{N(3-\frac{1}{N}\sum_{i=0}^{N} {v_e}^i)^2} \end{bmatrix}$$

Each elemental matrix $\boldsymbol{K_e^d(v_e)}$ is generated introducing this matrix in equation 3.3. Finally, these elemental matrices are assembled to build the global matrix $\boldsymbol{K^d(v_e)}$.

- For v_p:

$$\boldsymbol{A}\frac{\partial \boldsymbol{c^{t+1}}}{\partial \boldsymbol{v_p}} = \Delta t \boldsymbol{R} \odot \left((\boldsymbol{k^{Trans}} \oslash \boldsymbol{v_e}) c_p^{t+1} \right) + \boldsymbol{RI}\dot{c_p}^{t+1} + \boldsymbol{C^d}\frac{\partial \boldsymbol{c^t}}{\partial \boldsymbol{v_p}} \quad (3.12)$$

To compute equations 3.10-3.12, matrices $\boldsymbol{C^d}$ and $\boldsymbol{R}$ are exported from *ANSYS* along with $\boldsymbol{K^d(v_e)}$. After solving these equations, the Jacobian matrix is obtained by concatenating the matrices computed in equations 3.10-3.12:

$$\begin{bmatrix} \frac{\partial c_1^1}{\partial k_1^{Trans}} & \cdots & \frac{\partial c_{nnode}^1}{\partial k_{nnode}^{Trans}} & \frac{\partial c_1^1}{\partial v_{e1}} & \cdots & \frac{\partial c_{nnode}^1}{\partial v_{e\,nnode}} & \frac{\partial c_1^1}{\partial v_{p_1}} & \cdots & \frac{\partial c_{nnode}^1}{\partial v_{p_{nnode}}} \\ & & & & \vdots & & & & \\ \frac{\partial c_1^{ntime}}{\partial k_1^{Trans}} & \cdots & \frac{\partial c_{nnode}^{ntime}}{\partial k_{nnode}^{Trans}} & \frac{\partial c_1^{ntime}}{\partial v_{e1}} & \cdots & \frac{\partial c_{nnode}^{ntime}}{\partial v_{e\,nnode}} & \frac{\partial c_1^{ntime}}{\partial v_{p_1}} & \cdots & \frac{\partial c_{nnode}^{ntime}}{\partial v_{p_{nnode}}} \end{bmatrix}$$

This matrix is included in the least-squares method to fit the CA concentration-time curves to equation 2.5. We tested this semi-analytical computation in small-sized models, comparing it to the numerically computed Jacobian. Results were promising, as both matrix and convergence were similar between the two methods. Further information about these results can be found in Appendix A.1.

The optimization algorithm developed takes as inputs an initial set of values of the unknowns, as well as the curves to be fitted. The model proposed defines a set of three parameters (K^{Trans}, v_e and v_p) per node. This implies that the algorithm needs to fit three times the number of nodes simultaneously. Starting from the initial seed provided, a forward simulation of the D-ETM is executed, obtaining a first set of curves that are then used to initialize the cost function. Then, the numerical matrices needed for the Jacobian computation ($\boldsymbol{C^d}$, $\boldsymbol{R}$ and $\boldsymbol{K^d(v_e)}$) are exported by running several scripts on *ANSYS*. Once the Jacobian is obtained, the minimization solver computes the updated set of parameters, finishing the first iteration. A schematic pseudocode of this process is presented in Algorithm 1.

The cost function (CF) defined for the method is a standard sum of squared differences (equation 3.13), which has proven to be effective in the simulated cases:

$$CF = \sum_{i=0}^{N_{time}} (y_i - f_i(\boldsymbol{x_j}))^2 \tag{3.13}$$

Where N_{time} is the total number of time points, y_i is the value of the reference concentration at time point i and $f_i(\boldsymbol{x_j})$ is the value at time point i of the curve obtained from running a simulation of D-ETM with given $\boldsymbol{x_j}$ vector of parameters.

Other cost functions that only consider a fraction of the time points, like those proposed in [40], were tested. Nevertheless, they showed convergence problems, leading to the algorithm getting caught in local minima distant from the global optimum.

The solver method chosen to perform the minimization was the Trust Region Reflective (TRF) algorithm [77]. Although the commonly used Levenberg-Marquardt (LM) [78] is also suitable for our purposes, the TRF algorithm (in its Scipy [79] implementation) handles sparse matrix. Given the nature of our problem, working with matrices in sparse format for the Jacobian computation dramatically reduced the use of system memory (around 98% reduction). We compared the performance of the LM algorithm against the TRF (converting the matrices to dense format for the LM method). Both methods retrieved accurately the reference values and the number of iterations needed was similar in both cases.

The proposed curve generation and curve fitting processes were executed in a cluster composed of 480 CPUs and 1088 GB of RAM. Specifically, the resources employed for the benchmark problem and the real tumor geometry were: 16 CPUs and 16GB RAM and 24 CPUs and 32GB RAM, respectively. The optimization time

of the benchmark problem was 1.5h on average (fitting 360 time points on 339 nodes) and for the tumor geometry was around 10h on average (fitting 360 time points on 955 nodes). The optimization algorithm was developed in Python and APDL and the forward simulations were generated on *ANSYS* 2019R2.

Algorithm 1 Pseudocode of the optimization process

1: Generate an initial set of parameters (P_0) ▷ Initial seed
2: **while** (CF $>$ Threshold 1) or (δ $>$Threshold 2) **do** ▷ Convergence criteria. δ is the increment to the parameter vector
3: Run forward FE model with the current set of parameters (P_i) ▷ Obtain fitted curves
4: Evaluate CF
5: Export numerical matrices from *ANSYS* ▷ Export $\boldsymbol{C^d}$, $\boldsymbol{R}$ and $\boldsymbol{K^d(v_e)}$
6: Compute Jacobian matrix
7: Define new set of parameters $P_{i+1} = P_i + \delta$ ▷ where δ is computed by the TRF [77] via the gradient
8: **end while**

3.4 *In silico* simulations

In order to test the performance of the optimization algorithm proposed and to compare the D-ETM to the ETM, two different sets of simulated tissue concentration time courses have been generated from the forward FE model of the D-ETM and some sets of known parameters (K^{Trans}, v_e, v_p and D).

The first case corresponds to a simple 2D geometry, where the distribution of parameters generates a CA distribution that is completely dependent on diffusion. The second case, on the other hand, is based on a more complex geometry inspired in clinical data of tumors [48].

Although the proposed method can be applied to both 2D and 3D cases, given the common resolution of imaging data (slice thickness is usually several times the pixel size), we focused on 2D geometries to keep the computational cost affordable. Due to this size difference, the effects of out-of-plane diffusion are expected to be negligible in comparison with the in-plane diffusion [41]. In terms of computation, it is dramatically faster (up to two orders of magnitude) to parallelize several 2D simulations rather than studying all of them as a 3D case.

The geometries correspondent to both cases were meshed using linear quadri-

lateral diffusion elements (PLANE238 in *ANSYS* manuals [80]) of size 0.15 mm, which generates a mesh of higher density than of most of the clinical and experimental imaging data.

Similarly to previous works [38], the diffusion coefficient D was given a value of 2.6E-04 mm^2/s, which is consistent with experimental measurements [37, 43]. Considering the formulation of the diffusive term of the model proposed here (equation 2.5), the diffusion coefficient was constant in both cases.

The AIF used in the simulations (Figure 3.1) was inspired on the clinical data collected within the European research Project PRIMAGE [48].

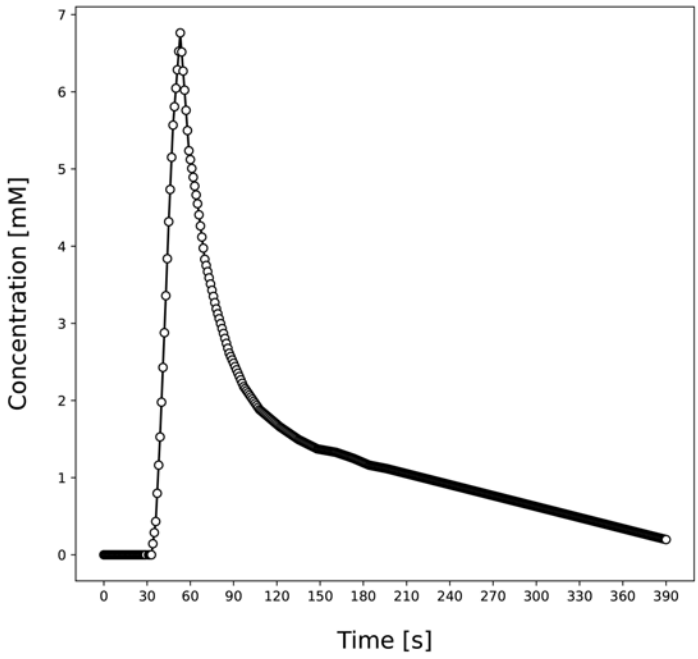

Figure 3.1: AIF used for the simulations.

3.4.1 Benchmark problem

This case is based on the one proposed by Pellerin *et al.* [40], which was also included in the work of Fluckiger *et al.* [41]. Given the importance of these

contributions into the study of CA diffusion process, we consider this case as a *benchmark problem* for PK models that incorporate diffusion.

Hence, we simulated a slice of a circular, radially symmetric, tissue. The definition of both the geometry and the distribution of parameters aims to generate an extreme case of a distribution of CA that is diffusion-limited. To do so, the circle is divided into two different regions: a highly perfused rim and a necrotic core.

Initially, the parameters values chosen were similar to those used by Fluckiger *et al.* [41]: K^{Trans} = 0.2 min^{-1} in the rim and 0.05 min^{-1} in the core; a constant value of v_e equal to 0.5 in the whole model; and, finally v_p = 0.05 in the rim and 0.005 in the core.

When running the optimization algorithm on this case, we observed that, although the cost function was reduced to values close to zero, the parameters returned were different from the true ones. Upon closer examination, we noticed the existence of several local minima close to the global optimum. Figure 3.2 shows two different nodes where the true values of the model parameters were the same, and so were the generated CA curves. However, although the fitted curve is almost identical to the reference one, the two sets of fitted parameters are different between them and both differ from the true values. It must be noted that some of the parameters retrieved are unphysical: K^{Trans} and v_p below zero in the second case of Figure 3.2. Even when applying bounds to keep the parameters within physical ranges (K^{Trans} greater than zero and v_e and v_p between zero and one), the optimization algorithm still got caught in a local minimum.

This meant that the success of the optimization process was dependent on the initial seed. The curves shown in Figure 3.2 were obtained using as initial seed a set of values that was a random distribution of values between 0.4 min^{-1} and 0, for K^{Trans}; between 0.2 and 0.8 for v_e; and between 0 and 0.1 for v_p. In this case, the optimization method retrieved accurate results only if the initial seed was very close to the true values.

We attribute this problem to the numerical instability produced by the radial symmetry, both in geometry and parameters, which produces a set of identical curves at nodes with similar values. To prove this hypothesis, we created two additional simulations. In the first one, the parameters were kept constant for each region, while the geometry was modified to suppress the axial symmetry. The results obtained from these simulations are detailed in Appendix A.2. In the second simulation, the geometry was preserved, while the parameters were changed by random distributions of values within a range. Such, K^{Trans} was assigned values

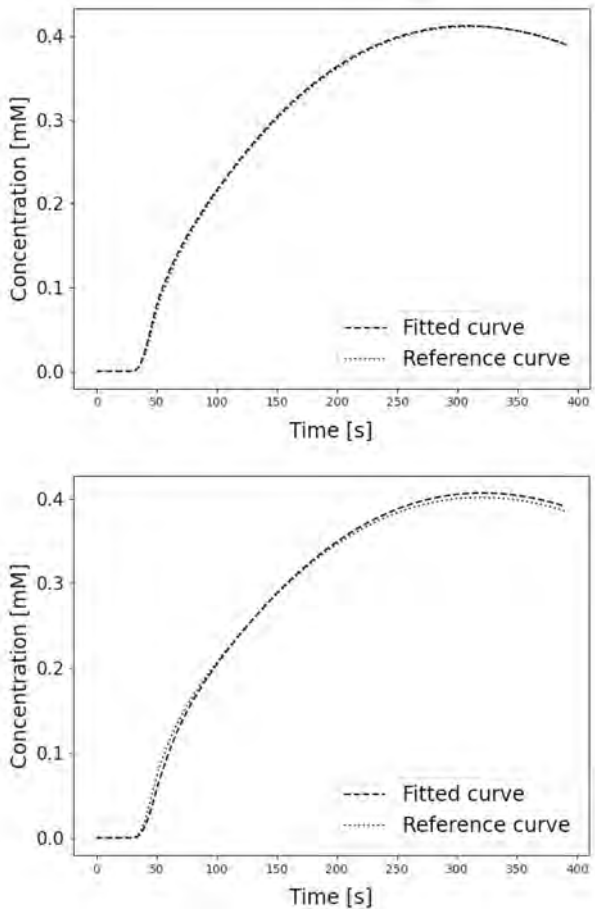

Figure 3.2: Two of the sets of curves (simulated and fitted) correspondent to some of the nodes within the necrotic region of the first simulation of the benchmark problem. The true values for both nodes are: K^{Trans}=0.05 min^{-1}, v_e=0.5 and v_p=0.005. The fitted values are: in the first case, K^{Trans}=0.15 min^{-1}, v_e=0.41 and v_p=0.01; and, in the second case: K^{Trans}=-0.09 min^{-1}, v_e=0.25 and v_p=-0.001. These results demonstrate the convergence of the inverse method to a local minima.

between 0.25 min^{-1} and 0.15 min^{-1} in the rim and between 0.05 min^{-1} and 0 min^{-1} in the core. v_p, on the other hand, was given values between 0.08 and 0.03 in the rim, and between 0.01 and 0 in the core. v_e maintained its original values. The initial seed was the same as in the previous simulation.

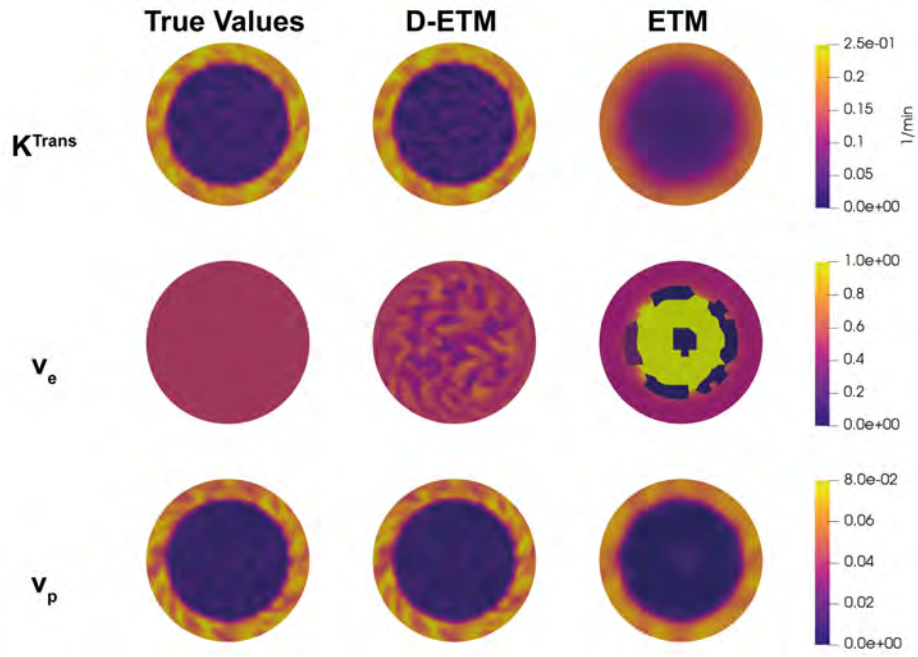

Figure 3.3: Second simulation of the benchmark problem. Comparison between the reference values and the parameters returned by the D-ETM and the ETM. Results show that the D-ETM accurate retrieves the distribution of K^{Trans} and v_p, while the ETM shows an averaging pattern, especially for K^{Trans}. Although not as accurate as the other parameters, the v_e map returned by the D-ETM is within the physiological range [0,1], while the distribution obtained from the ETM reaches values close to infinity in the necrotic core.

Results obtained with the ETM on this simulation are consistent with previous works [40, 41]. The K^{Trans}, mainly, and the v_p maps, to a lesser extent, show an averaging pattern with respect to the reference values. Besides, the v_e map returns unphysical values (v_e>1 and v_e<0) in the necrotic region (Figure 3.3). Even if the K^{Trans} and v_p in the necrotic region are not exactly zero, the enhancement curve of these nodes is completely dependent on diffusion. Thus, these curves cannot be accurately fitted to the Tofts formulation. Besides, the vascularized regions adjacent to the necrotic ones are also influenced by these values, since there is diffusion of CA from the former to the latter. This diffusive process results in a lower CA concentration, which is then fitted to K^{Trans} values below the true ones. v_p is not as affected by this effect as K^{Trans} is, resulting in a better fit for this parameter. The distributions obtained with the D-ETM are very accurate for

Table 3.1: Comparison of error metrics between the D-ETM and the ETM for the benchmark problem. K^{Trans} absolute error is measured in min^{-1}. Results were computed from ten simulations.

	D-ETM				ETM			
	Absolute error		Fraction of nodes error <threshold		Absolute error		Fraction of nodes error <threshold	
	Mean	SD	Mean	SD	Mean	SD	Mean	SD
K^{Trans}	8.14E-03	1.18E-03	71.54%	6.03%	3.71E-02	6.93E-04	19.03%	2.19%
v_e	9.53E-02	4.42E-03	77.58%	1.42%	7.78E+06	5.46E+05	54.57%	0.53%
v_p	3.79E-04	7.45E-05	94.13%	3.02%	7.08E-03	2.71E-04	74.93%	1.35%

K^{Trans} and v_p, while the fitted v_e map shows higher error, especially in the necrotic region. This error is related to the influence of the variable in the global solution. If we take a look at equation 3.11, we can see that the value of this derivative is dependent on the value of K^{Trans} and v_p. Therefore, in those necrotic regions, where these parameters present values close to zero, the derivative depends only on the diffusive term. Due to the definition of this term (equation 2.6), the influence of v_e is limited. Thus, because of its low effect on the global solution, the optimization algorithm is not able to retrieve accurate results for v_e, especially on necrotic regions.

A quantitative comparison between the outcome of both models is presented in Table 3.1. Since both the true and initial values for the simulations are a function of randomness, ten cases with different true and initial sets of parameters were tested to validate the robustness of the method. Considering that reference values for K^{Trans} and v_p reached zero in the necrotic region, the use of relative error metrics is unfeasible. The absolute error, measured as the absolute difference between the fitted and the reference value, was selected to compare the performance of both models.

Different error thresholds were defined to compare the performance of both models. Threshold for K^{Trans} was set to 0.01 min^{-1}, which is the maximum precision of the DP model [40]. Similarly, the threshold for v_p was set at 0.001, a value that can be considered as sufficient precision for this kind of models. Due to the slight impact of v_e maps on the global solution, its threshold was set to 0.15.

The D-ETM clearly outperforms the ETM, especially on K^{Trans} maps. While only 19% of nodes fitted by the ETM are within a 0.01 range from the reference value, 72% of those retrieved by the D-ETM fall into that range. Besides, the K^{Trans} mean absolute error in the ETM is around four times higher than the one

correspondent to the D-ETM.

Due to the great effect of the unphysiological values of v_e returned by the ETM on the absolute error, this metric will not be used to compare the models. The fraction of nodes whose error is below 0.15, however, is not affected by these values. While only 55% of the values obtained using the ETM are within the error range, almost 78% of the ones retrieved by the D-ETM fall into this range. Despite experiencing difficulties retrieving the correct v_e maps, the D-ETM shows a great improvement with respect to the ETM. Besides, all of the v_e values fitted using the D-ETM were within the physiological range [0,1].

The mean absolute error of D-ETM v_p maps is around half the error obtained by the ETM. Nevertheless, this parameter does not seem to be as affected by diffusion as the other two.

Although the error retrieved by suppressing the homogeneity in the distributions of parameters (Figure 3.3) was lower than the error obtained by removing the axial symmetry in geometry (Appendix A.2), these results demonstrate that the combination of both factors was causing the convergence of the algorithm to local minima.

Analysis of the mesh effect

The influence of mesh size on the convergence of both the forward and the inverse models was tested using the benchmark problem geometry. Two different meshes were generated: the first one discretized the geometry using 0.15 mm size elements, while the element size on the second one was half that value. The number of nodes on the two simulations were 339 and 777, respectively. The same type of elements (linear quadrilateral diffusion elements) was used on both models. On both cases, the sets of true and initial values were random distributions between the ranges defined previously. Just as in the benchmark problem, ten different simulations were generated for the finer mesh, to eliminate the influence of randomness on the result.

The results presented in Table 3.2 show that the method reduces the error when refining the mesh. Nevertheless, the slight increase in accuracy does not justify the greater computational cost associated to the finer mesh. The finer mesh model needed twice the time of the original model to fit the curves. Therefore, the element size selected for the simulations was 0.15 mm, a tradeoff between accuracy and computational cost.

Table 3.2: Comparison of error metrics between two different meshes. K^{Trans} absolute error is measured in min^{-1}. Results were computed from ten simulations.

	0.15 mm element				0.075 mm element			
	Absolute error		Fraction of nodes error <threshold		Absolute error		Fraction of nodes error <threshold	
	Mean	SD	Mean	SD	Mean	SD	Mean	SD
K^{Trans}	8.14E-03	1.18E-03	71.54%	6.03%	7.65E-03	7.43E-04	72.5%	4.12%
v_e	9.53E-02	4.42E-03	77.58%	1.42%	9.11E-02	3.96E-03	80.35%	1.41%
v_p	3.79E-04	7.45E-05	94.13%	3.02%	3.24E-04	3.78E-05	97.03%	1.85%

3.4.2 Real tumor geometry

A second set of simulations was generated to test the performance of the D-ETM in real geometries and vascular properties with a heterogeneous distribution. The geometry corresponded to a tumor slice of around 20 mm^2, while the vascular properties were inspired by clinical data [48].

The vascular properties distribution is divided into three different zones: a highly perfused region, an intermediate region and a necrotic region. Depending on the zone, the assigned parameters were: for K^{Trans}, random values between 0.4 and 0.3 min^{-1}, between 0.25 and 0.1 min^{-1} and between 0.05 and 0 min^{-1}, for the three respective regions. v_e values were randomly selected within a range between 0.85 and 0.75 for the necrotic region and 0.6 and 0.4 for the other two. Finally, v_p random distribution ranged from 0.08 to 0.03 for the highly perfused nodes, between 0.05 and 0.03 in the intermediate region and between 0.01 and 0.005 in the necrotic one.

The convergence of the inverse method was tested by providing random distributions of parameters as initial values. The ranges for K^{Trans}, v_e and v_p were the same as in the previous case: [0,0.4] min^{-1}, [0.2,0.8] and [0,0.1], respectively. Following the procedure described in the previous case, ten simulations with different reference and initial values were generated. The heterogeneous reference maps generated clearly expose the limitations of the ETM in accurately capturing the K^{Trans} distributions (Figure 3.4). While the D-ETM provides an almost exact distribution for K^{Trans} and v_p and an acceptable v_e map, the ETM tends to homogenize the K^{Trans}, failing to depict the highly perfused regions, as well as the necrotic ones. This effect is particularly visible in those zones where two of these regions are adjacent.

The error metric employed in this case was the absolute relative difference

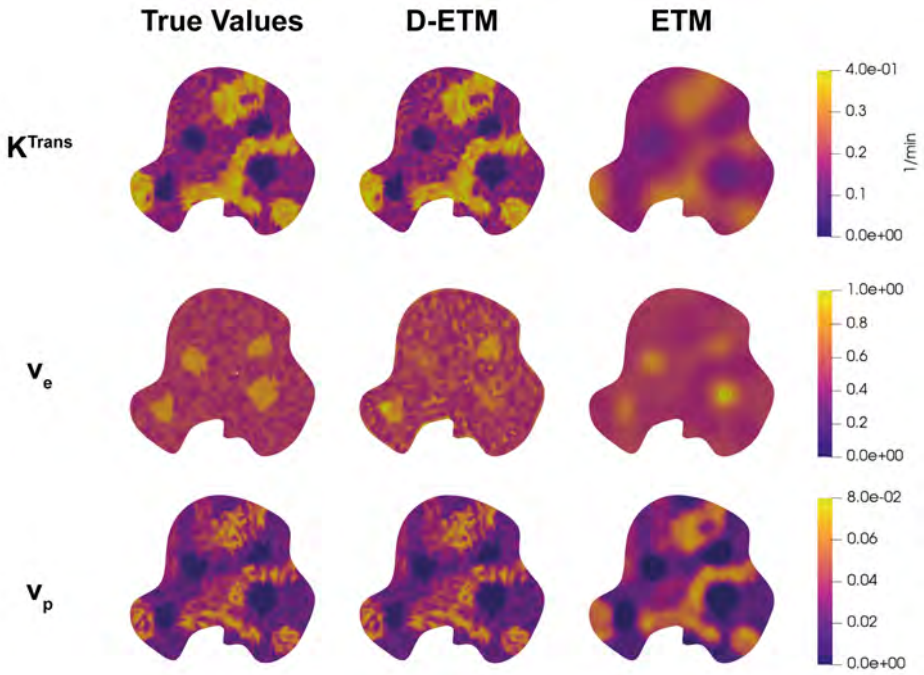

Figure 3.4: Real tumor geometry. Reference values and results of the D-ETM and the ETM for each of the parameters. Result show that the D-ETM accurate captures the heterogeneity of the distribution of parameters, while the ETM tends to average the values. The maps of v_p are the least sensitive to this phenomenon. The v_e distribution obtained from the D-ETM shows a more accurate fit than the one obtained in the benchmark case.

Table 3.3: Error metrics comparison between the D-ETM and the ETM for the second case. Results were computed from ten simulations.

	D-ETM				ETM			
	ARD		Fraction of nodes ARD <20%		ARD		Fraction of nodes ARD <20%	
	Mean	SD	Mean	SD	Mean	SD	Mean	SD
K^{Trans}	16.37%	3.67%	87.21%	2.67%	148.42%	47.37%	39.85%	1.6%
v_e	15.54%	1.02%	76.87%	2.69%	11.36%	0.22%	85.71%	1.07%
v_p	8.59%	4.45%	95.56%	3.02%	194.85%	101.26%	40.13%	1.53%

(ARD), calculated between true and fitted parameters. Table 3.3 shows the metrics correspondent to the average of ten different simulations of the real geometry

case. In this case, where necrotic zones were not as large as in the previous case, the ETM accurately retrieves the v_e map (mean ARD is 11% and 86% percent of nodes have an ARD below 20%), depicting the increase in v_e correspondent to these necrotic regions (Figure 3.4). The D-ETM, on the other hand, gives a good fit for the v_e map (mean ARD is 16% and the ARD is below 20% in 77% of the nodes), although it is not as accurate as the ETM in fitting the v_e values in necrotic nodes (Figure 3.4). K^{Trans} and v_p distributions obtained from the D-ETM are almost an exact representation of the reference maps (Figure 3.4), as evidenced by the metrics obtained (Table 3.3). The mean ARD is 16% and 9% for K^{Trans} and v_p, respectively. The ETM, nonetheless, show higher error for these two parameters (mean ARD of 148% and 195% for K^{Trans} and v_p, correspondingly, and for both maps only 40% of nodes have an ARD below 20%).

In their work, Pellerin *et al.* [40] tested the performance of their model in a simulated case similar to the real geometry case presented in here. The DP model obtained a mean ARD of 16% for K^{Trans} and 17% for v_e, with 73% of the K^{Trans} values and 77% of the v_e values within 20% of the true values. The D-ETM has obtained identical values for v_e and a similar mean ARD for K^{Trans}, improving the fraction of values whose ARD is below 20%.

Influence of noise

To test the robustness of the D-ETM to the addition of noise, several simulations were conducted. Starting from a set of reference values similar to those generated in the last case, experimental levels of noise were added to the generated curves. These levels were defined using a gaussian distribution with a standard deviation (SD) equal to a fraction (1%, 2.5% and 5%) of the highest concentration reached in the curve.

The results of these simulations presented in Figure 3.5 show the effect of noise on both the D-ETM and the ETM. Despite showing higher error for noise-free simulations, the parameters returned by the ETM seem to be unaffected by noise, since the histograms show almost no difference in the distribution of ARD between the cases with different levels of noise. The added noise shows greater influence on the parameters obtained fitting the D-ETM. Noise seems to have the greater effect on v_p and the slighter effect on v_e. K^{Trans}, for its part, shows a slight disturbance when the noise level is low (1% and 2.5%), having more than 70% of its values within a 20% range from the true values. When the added noise reaches the maximum value, this percentage drops dramatically to 30%.

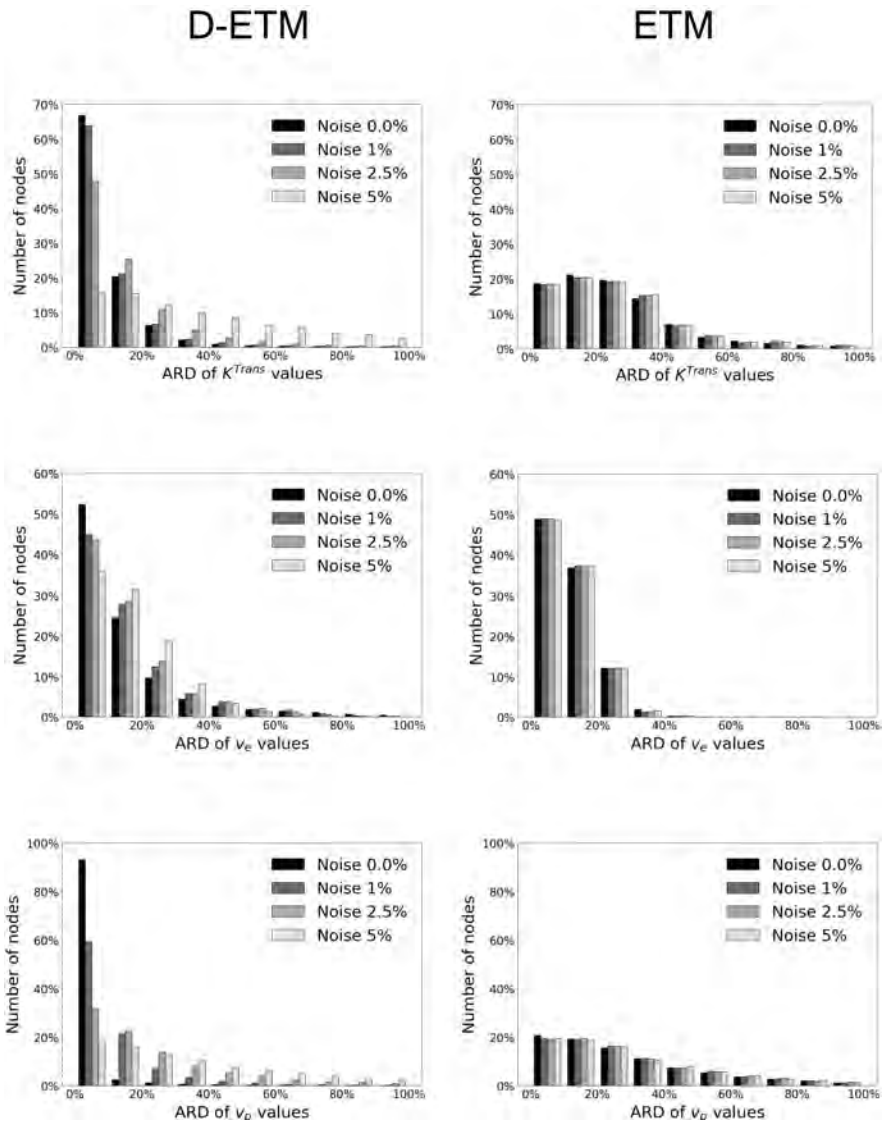

Figure 3.5: Influence of noise on the accuracy of the D-ETM (left) and the ETM (right). Results show that noise has greater influence on the D-ETM, particularly on v_p. Although the ETM seems to be unaffected by noise, for noise values below or equal to 2.5% the D-ETM still performs better. Even for the maximum levels of noise (5%), the error in the D-ETM solution is similar to the one in the ETM.

These results are consistent with those obtained by Pellerin *et al.* [40]. In their work, the authors attributed this different effect of noise on parameters depending on the influence of each parameter on the different parts of the CA curve. Thus, v_e regulates the last part of the curve, where the concentration is close to the maximum and, therefore, it is less sensitive to noise. K^{Trans}, and even more v_p, affect the initial part of the curve. Consequently, the influence of added noise is greater on these parameters.

The great number of variables to be fitted simultaneously makes this model, as well as the model developed by Pellerin *et al.* [40], more sensitive to noise. Therefore, when fitting the model to experimental data it must be ensured that the signal-to-noise ratio (SNR) of the data meets the model requirements.

3.5 Discussion

The use of DCE-MRI sequences to assess the efficacy of antiangiogenic therapies in tumors [53–55] increases the need for PK models that retrieve vascular properties as accurate as possible. Several authors have pointed out the limitations of the widely used standard and extended Tofts models when the CA reaches the ROI through passive delivery [40–44, 46, 47]. These models return an inaccurate estimation of K^{Trans} as well as unphysical values for v_e in those regions within the ROI where the active delivery of CA is low or non-existent (necrotic zones). Different models and methods have been developed to assess the effect of diffusion and to develop PK that accounted for this process [40, 41, 44, 47]. These works exposed the mentioned limitations and proposed different approaches to include the effects of diffusion into the STM and the ETM. Pellerin *et al.* [40] were the first to include a diffusive term into the STM. The DP model proposed showed an improvement in parameter accuracy with respect to the original STM in those regions where passive delivery of CA was significant. One of its major limitations was the high computational cost associated to the simulated annealing algorithm, since the model had to fit all voxels simultaneously. Fluckiger et al [41] added some hypotheses to the DP model (homogeneity in the diffusive coefficient and v_e between neighboring voxels) that allowed them to compute the effects of diffusion while fitting each voxel separately and, therefore, reducing substantially the computational cost. However, this homogeneity hypothesis may not be suitable for some kind of tumors (such as neuroblastoma, which is a type of cancer characterized by its high heterogeneity [81]). Cantrell *et al.* [44] based their formulation of the diffusive term on the one proposed by Pellerin *et al.* [40] and proposed a diffusion-compensated Tofts model (DC-Tofts). Their work consisted

on obtaining the ETM parameters from CA curves, then computing the diffusion contribution from these fitted parameters to generate a new set of curves and, finally, fit again these last curves with the ETM. Although this model was suitable for intracranial aneurysms, the approach used may not be appropriate for other type of lessions where necrotic zones are present, since the initial fit of the ETM would retrieve unphysical values of v_e that would condition the following diffusion computation.

The performance of the D-ETM and the FE-based method here proposed was tested using two different *in silico* cases. The first one, a benchmark problem derived from literature [40, 41], exposed the limitations of the ETM in those regions were passive delivery of CA is the main transport mechanism. Results showed the improved accuracy of the model parameters returned by the D-ETM, which were very close to the reference values (mean absolute error for K^{Trans}, v_e and v_p were 0.008 min^{-1}, 0.095 and 0.0004, respectively). A second case inspired in real tumor geometries and parameters was analysed. Again, the ETM performed poorly, returning an incorrect estimation of K^{Trans}. In both simulations, the K^{Trans} distribution obtained by the ETM appeared averaged with respect to the reference maps, adding significant error to the parameters. D-ETM parameters were almost identical to the true values, accurately depicting the heterogeneous distribution of values. Besides, Figure 3.5 shows that the error obtained by the D-ETM follows a Pareto-like distribution for noise levels below 2.5%, what means that the smallest errors are obtained for most of nodes, while the ETM does not follow this pattern (except for v_e), even for noise-free simulations.

The results obtained from the D-ETM in both cases show lower accuracy in v_e maps with respect to the other variables, especially on necrotic regions, where K^{Trans} values are very close to zero. This is due to the modest influence of v_e on the global solution in these regions. To solve this issue, future works could develop an alternative expression for the effective diffusivity where v_e would have more influence. Nevertheless, the accuracy of the v_e maps obtained from the D-ETM is acceptable, keeping all of their values within the physiological range. Moreover, the v_e maps retrieved by the D-ETM on the real tumor geometry show an accuracy similar to the DP model [40].

Due to the additional variable included in the ETM with respect to the STM (the volume fraction of blood plasma, v_p), the convergence of the optimization algorithm can be affected by the presence of local minima within the solution space. This means that the solution is dependent on the initial seed. Although our model seems to overcome this issue on the simulated cases, the values obtained from the ETM could be used as an initial seed in those cases where the

minimization convergence is severely affected by this issue.

This new formulation is limited by the computational cost associated to the optimization algorithm. Although the method benefits from the computational efficiency of the FEM, the optimization time for the two simulated cases was 1.5h and 10h on average (fitting 360 time points on 339 nodes and 955 nodes, respectively). Despite being faster than the DP model (average of 72h to fit 484 voxels), the execution time cannot be compared to the ETM, which took an average of 5s and 12s, respectively. Future works can be applied to migrate the code from Python to more efficient languages, such as C. One of the bottlenecks of this method is the Jacobian matrix computation, which executes operations on large sparse matrix. This computation could be parallelized to reduce the execution time. Alternatively, the gradient could be computed using the adjoint-based method [82], which has proven to be very efficient when computing the gradient of an objetive function with respect to a large number of parameters, as it is our case.

The described D-ETM is the first diffusion-corrected PK model to be implemented using the FEM. It proposes a new formulation for the diffusive term, based on the concept of effective diffusivity, that simplifies the computation of this term and avoids the inclusion of additional variables to the model. The semi-analytical method formulated to compute the Jacobian matrix opens the door for further gradient-based optimization methods for FE-based PK models. Although previous works [38] have developed a FE implementation of the extended Tofts model, their objective was to expose the effect of intra-voxel CA diffusion on PK analyses. To the best of our knowledge, this is the first FE-based optimization algorithm for the ETM. The results obtained with this model are promising, since it accurately retrieves the reference values, outperforming the ETM. Future works should test this model on real clinical or experimental data.

Chapter 4

Evaluating the use of Physics-Informed Neural Networks to fit the D-ETM to DCE-MRI data

This chapter is based on:

Sainz-DeMena D., Perez, M. A., Garcia-Aznar J. M. *Exploring the potential of Physics-Informed Neural Networks to extract vascularization data from DCE-MRI in the presence of diffusion*

Submitted to *Medical Engineering and Physics* Journal

4.1 Introduction

In the previous chapter, we demonstrated the importance of CA diffusion, especially in necrotic regions in tumors, and showed the increased accuracy of the D-ETM model with respect to the ETM when retrieving the model parameters in the presence of CA diffusion. Nevertheless, due to the ill-posed nature of the problem, the FE-based algorithm faced convergence problems, getting caught in local minima in some cases.

Thanks to the great advances in Machine Learning (ML), and more precisely in DL, in the last years several authors have developed different DL-based methods to retrieve PK model's parameters from DCE-MRI data. Such works mainly focus on the use of convolutional neural networks (CNN) [83–85] and recurrent neural networks (RNN), such as long short-term memory (LSTM) networks [86]. The main drawback of these architectures is that both are purely data-driven approaches. This means that these networks need to be trained on a sufficiently large dataset that includes different patients from distinct clinical centers where diverse protocols may have been applied. Besides, they do not only need the raw clinical data, but also the "ground-truth" for the parameters of the model being fitted. Although in the case of the STM or the ETM these parameter values can be extracted using a fast algorithm such as non-linear least-squares (NLLS) [76] fitting, if we want to include the diffusive term we need to incorporate other optimization algorithms, such as those proposed in [40, 41, 44, 47, 52]. This poses a major challenge, since those algorithms that are fast enough for this task make assumptions that limit their applicability to certain tissues [41, 44] and those which can be widely applied to different tissues are too computationally expensive to fit such a large dataset and struggle to converge to the exact solution in some situations [40, 47, 52]. Thus, it appears that the problem we are addressing requires that the known physical laws that govern the processes of CA transport are included in the network architecture, steering away from purely data-driven approaches.

Recently, PINNs [87–89] have emerged as a promising alternative for solving PDEs and other inverse problems. PINNs combine the flexibility and scalability of neural networks with the physical constraints imposed by the underlying equations, allowing for efficient and accurate solutions even for highly nonlinear and ill-posed problems. Other authors have used this type of NN to fit tracer-kinetic models to DCE-MRI data [90, 91], outperforming current NLLS method. Zapf *et al.* [92] used PINNs to estimate the diffusion coefficient governing the long term spread of molecules in the human brain from diffusion tensor imaging (DTI) MR

data, showing its potential for this task. The results obtained in these works show that PINNs can successfully retrieve PK parameters and solve inverse problems of CA diffusion in biological tissues.

In this chapter, we investigate the potential of using PINNs to fit diffusion-corrected PK models to synthetic DCE-MRI data, with the aim of establishing a robust framework for future analysis. To facilitate our exploration, we focus on 1D spatial domains while highlighting the broader implications of this approach for advancing DCE-MRI data analysis.

With this physics-driven NN architecture we aim to overcome the limitations of traditional solvers and achieve more robust parameter estimation for DCE-MRI analysis, showing the potential of PINNs to extract more accurate vascularization data from this type of MR sequences, even when faced with noisy and incomplete data.

4.2 Methods

This section begins with a brief explanation of the fundamentals of PINNs, followed by a description of the PINN implementation chosen for the specific D-ETM problem.

4.2.1 Physics-Informed Neural Networks

In recent years, the field of biomedical engineering has significantly increased in the use of DL techniques for a wide range of applications, from medical image analysis [93] to drug discovery [94]. DL algorithms have shown great promise in improving the accuracy and efficiency of tasks such as disease diagnosis, prognostication, and treatment planning [95]. However, many of these approaches rely on large amounts of labeled data, which can be challenging to obtain in biomedical settings [96]. This is where PINNs have emerged as a promising alternative, leveraging the underlying physics of the problem to reduce the reliance on labeled data and improve model generalization [97].

PINNs incorporate prior physical knowledge of the problem into the neural network architecture, making them more efficient and accurate than traditional data-driven DL approaches. PINNs can include PDEs to encode the governing physics of the problem, and then use neural networks to approximate the solution to the PDEs.

This combination of physics-based constraints and data-driven learning makes PINNs particularly effective for problems with limited data and complex physical phenomena. In the following sections, we will explain the basic concepts of PINNs and how we used them to solve our specific problem.

Fundamentals

PINNs are based on two main concepts: the Universal Approximation Theorem [98] and Automatic Differentiation (AD) [99].

The Universal Approximation Theorem states that any arbitrary function, no matter its complexity, can be approximated by a NN with only one hidden layer and a finite number of neurons.

Automatic differentiation is a technique for efficiently computing the derivatives of a function specified by a computer program. It works by recursively applying the chain rule of calculus to elementary operations such as addition, multiplication, and elementary functions like exponentials and trigonometric functions. This allows us to compute exact derivatives to machine precision without the need for symbolic manipulation or numerical approximations. In other words, we can obtain the derivatives of a function with the same precision as the function itself.

Therefore, one can train a NN to express solutions of time-dependent linear and non-linear PDEs from a set of inputs. Given a PDE of the form:

$$\frac{\partial u}{\partial t} + \mathcal{N}[u; P] = 0, \quad \boldsymbol{x} \in \Omega \subset \mathbb{R}^D, \quad t \in [0, T] \tag{4.1}$$

where $\mathcal{N}[u; P]$ is a differential operator with parameters P acting on the hidden solution $u(\boldsymbol{x}, t)$. We can approximate the solution of the PDE $u(\boldsymbol{x}, t)$ with a NN such that $u(\boldsymbol{x}, t) \approx NN(\boldsymbol{x}, t; \theta)$, being θ the NN parameters and $(\boldsymbol{x}, t)$ the input variables.

The process of NN training comprises a set of training data, a loss function $\mathcal{L}$ that measures the fitness performance of the NN with respect to the objective, and an optimizer that adjusts the NN parameters to minimize $\mathcal{L}$. In the case of PINNs, we incorporate the PDE as a constraint in $\mathcal{L}$ to ensure that the solution obtained by the NN satisfies the physical laws described by the PDE on a certain set of collocation points $\{\boldsymbol{x}_i, t_i\}_{i=1}^{N_f} \in \Omega \times [0, T]$. In the case of inverse problems, where $u(\boldsymbol{x}, t)$ is known on some set of training points $\{\boldsymbol{x}_i, t_i, u_i\}_{i=1}^{N_u} \in \Omega \times [0, T]$, this loss function is composed by two main terms:

$$\mathcal{L}(\theta, P) = w_d \mathcal{L}_d + w_r \mathcal{L}_r \tag{4.2}$$

where:

$$\mathcal{L}_d = \frac{1}{N_u} \sum_{i=1}^{N_u} \left(u(\boldsymbol{x}_i, t_i) - NN(\boldsymbol{x}_i, t_i; \theta) \right)^2 \tag{4.3}$$

$$\mathcal{L}_r = \frac{1}{N_f} \sum_{i=1}^{N_f} \left(\frac{\partial NN(\boldsymbol{x}, t; \theta)}{\partial t} + \mathcal{N}[NN(\boldsymbol{x}, t; \theta); P] \right)^2 \tag{4.4}$$

and N_u and N_f are the number of training points and collocation points, respectively. The first term of the loss function (Equation 4.3) is the mean squared error (MSE) between the predicted solution and the ground truth solution at the sampled training points. The second term (Equation 4.4) is the MSE of the PDE residual at the collocation points. To compute this term, the derivatives included in the PDE are computed using automatic differentiation. Both terms are scaled by different weighting factors, w_d and w_r that control the relative importance of the data and PDE losses. Additionally, one may add other terms to the loss function related to boundary or initial conditions with their correspondent weighting factors, although they are not mandatory for inverse problems [100].
By minimizing this loss function, the NN learns to approximate the solution of the PDE at the training points while it satisfies the physical laws described by the PDE at the collocation points. For inverse problems this minimization process not only updates the NN weights and biases but also retrieves the unknown PDE parameters P.

Fitting the D-ETM using PINNs

After presenting the general concepts of PINNs, we now shift our focus to the specific implementation used to fit the D-ETM to synthetic DCE-MRI data.
Our implementation is based on previous works [87, 91, 101] that solved similar problems. Therefore we opted for a densely connected forward neural network (FNN) architecture consisting of 8 hidden layers and 100 neurons per layer and the hyperbolic tangent (*tanh*) as the activation function. A normalization layer was included before the hidden layers to normalize the spatial and temporal coordinates to the [-1,1] range, as it is recognized as a safeguard against vanishing

or exploding gradients, as well as a stabilizing factor for the training procedure [87]. The network parameters θ were initialized using Glorot initalization [102] while the D-ETM parameters P were given random values within the physiological range (K^{Trans} between 0.05 and 0.5 min^{-1}; v_e between 0.3 and 1.0 and v_p between 0.01 and 0.3). The original formulation of the loss function presented in Equation 4.2 is modified to include two additional terms:

$$\mathcal{L}(\theta, P) = w_d\mathcal{L}_d + w_r\mathcal{L}_r + w_{IC}\mathcal{L}_{IC} + w_C\mathcal{L}_C \tag{4.5}$$

where $\mathcal{L}_{\text{IC}}$ represents the initial conditions and $\mathcal{L}_{\text{C}}$ is a soft constraint for the PDE parameters and w_{IC} and w_C are their respective weighting factors. These additional terms are defined as:

$$\mathcal{L}_{IC} = \frac{1}{N_{IC}} \sum_{i=1}^{N_{IC}} (NN(\boldsymbol{x}_i, 0; \theta))^2 \tag{4.6}$$

$$\mathcal{L}_C = \sum_{i=1}^{N_p} \left(g(K_i^{Trans}, v_{ei}, v_{p_i}) \right) \tag{4.7}$$

where N_{IC} is the number of points used to evaluate the initial condition, defined as $C_t(\boldsymbol{x}, t) = 0$, and N_p is the number of points where the PDE parameters are evaluated. Given that the three D-ETM parameters (K^{Trans}, v_e and v_p) are spatial distributions, N_p should be equal or greater than the spatial discretization of the data points to achieve sufficient precision. The soft constraint presented in Equation 4.7 is defined as:

$$\begin{aligned} g(K_i^{Trans}, v_{ei}, v_{p_i}) = max(K_i^{Trans}, 0) - K_i^{Trans} + max(v_{ei}, 0) - v_{ei} \\ + max(v_{p_i}, 0) - v_{p_i} + max(v_{ei} + v_{p_i}, 1) - 1 \end{aligned} \tag{4.8}$$

Equation 4.8 sets the lower bound for all three PDE parameters to 0, while the upper bound for the sum of v_e + v_p is set to 1. This constraint ensures that the sum of the intravascular space and the EES does not exceed the total voxel volume. These limits ensure that the parameters obtained are physically plausible. The weighting factors were all set to 1 except w_r, which was given a value of 1000. Based on the different tests conducted, this combination of weights lead to the best results. The loss function defined in Equation 4.5 is minimized using the Adam optimizer [103] with a constant learning rate of 0.001 during 80.000 epochs. A schematic overview of this PINN implementation is presented in Figure 4.1.

The number of training points was obtained from the resolution of the synthetic data, with a total of 360 points in the temporal domain (1 s resolution) and

60 points in the spatial domain (0.1 mm resolution) (Chapter 3). That resulted in a total of 21.600 training points. N_{IC} and N_C were set to 100 and 120, respectively. We found empirically that enhancing the spatial discretization of PDE parameters (N_p) with a factor of 2 with respect to the data resolution increased the accuracy. Finally, 50.000 collocation points were distributed over the whole domain using the Latin Hypercube Sampling (LHS) method [104].

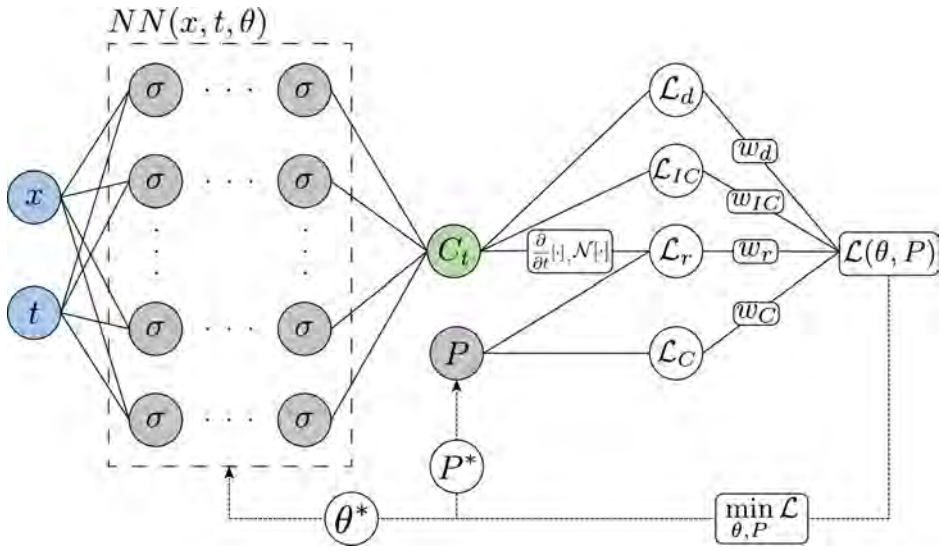

Figure 4.1: Schematic representation of the PINN implementation developed to fit the D-ETM. PINNs take advantage of the computational efficiency of automatic differentiation to get the derivatives of C_t needed for the computation of $\mathcal{L}_r$. As in any other inverse problem, the optimizer not only updates the NN parameters (θ^*) but also the PDE parameters (P^*).

The implementation shown so far includes most of the features described in the original work that laid the foundations for PINNs [87]. However, the results obtained with this implementation showed that, although the network was able to fit the data curves accurately, the error in the PDE parameters, particularly v_e, was too high. To retrieve more accurate PDE parameters, we introduced the residual based adaptive refinement (RAR) method [105]. The idea behind this method is to improve the distribution of collocation points during training. After a certain number of epochs (E_{RAR}), the collocation points are ranked by their mean $\mathcal{L}_\mathrm{r}$ value. Then the top k points are appended to the list of collocation points. This technique helps the NN focus on those regions where the PDE residual is higher, enhancing the gradients corresponding to the PDE parameters in that regions.

Furthermore, our tests showed that modifying only the temporal coordinate of the collocation point with a random noise of 1% of its value increased the accuracy of the results. This is probably related to the higher spatial resolution of the initial collocation points obtained with the LHS method with respect to their temporal resolution. Therefore, slightly modifying the temporal coordinate enhanced this temporal resolution. Through successive tests, the RAR parameters were set to E_{RAR} = 500 and k = 500.

It is important to note that all these hyperparameters were manually calibrated until we obtained satisfactory results. Moreover, it should be emphasized that before applying our methodology to more complex 2D cases, a proper tuning of the hyperparameters is necessary to understand and measure how each hyperparameter affect the results.

4.3 Examples of application

To assess the effectiveness of PINNs in accurately determining the D-ETM parameters in comparison to previous optimization algorithms described in Chapter 3, two distinct *in silico* cases were devised. Both cases were based on a 1D spatial domain that corresponds to a cross-section of a circular tumor with two different regions: a necrotic core and a highly vascularized rim, similar to the benchmark case used in Chapter 3 and also in previous studies [40, 41, 52]. The objective of this benchmark case was to highlight the effect of diffusion in CA transport, therefore pointing out the limitations of the ETM. The different sets of synthetic CA concentration time courses were generated using the forward implementation of the D-ETM in *ANSYS*, as described in Chapter 3. In all cases the diffusion coefficient for CA in free medium, D, was set to 2.6E-04 mm^2/s [37, 43]; while the AIF was the same as the one used in the previous chapter.

In the first case the distribution of K^{Trans} and v_p is homogeneous through each of the regions, taking values of 0.3 min^{-1} and 0.1 in the vascularized rim and 0.05 min^{-1} and 0.01 along the necrotic core, respectively. The second case, on the other hand, is based on a heterogeneous distribution of these two vascularization parameters: K^{Trans} and v_p defined in the ranges [0.2, 0.3] min^{-1} and [0.07, 0.13], respectively, along the vascularized rim and K^{Trans} taking values between 0.02 and 0.07 min^{-1} and v_p ranging between 0.0 and 0.05 in the necrotic core. In both cases, v_e was set to 0.5 through the whole domain, as in previous works [40, 41, 52]. We employed the ARD metric to quantify the error in the fitted parameters for each model.

Additionally, each case was fitted with the two original models: the ETM [35] and the D-ETM. The latter was fitted using two different optimization methods: the FE-based algorithm presented in Chapter 3 (D-ETM FE) and the PINN approach presented in this work (D-ETM PINN).

4.3.1 Homogenoeus distribution of parameters

As stated before, in the D-ETM PINN the D-ETM parameters were initialized using random values within their physiological ranges. In the case of the D-ETM FE the output from the ETM fitting was used as initial seed. This was done to reduce the complexity of the minimization process, trying to avoid local minima. Nevertheless, as Figure 4.2 and Table 4.1 show, this initial seed was not sufficient to prevent the D-ETM FE to converge to a local minimum in the homogeneous case. In fact, it shows a greater error than the ETM for the K^{Trans} distribution (87% of nodes fitted by the ETM have an ARD error lower than 20%, while the D-ETM has only 73% below that threshold). This outcome was expected, since the limitations of this D-ETM FE when dealing with homogeneous distributions were first discovered in the previous chapter.

Table 4.1: Error metrics comparison between the D-ETM (FE and PINN methods) and the ETM for the homogeneous case. The two metrics computed are the mean ARD and the fraction of nodes whose ARD is below the defined threshold of 20%.

	D-ETM PINN		D-ETM FE		ETM	
	ARD (%)	Fraction of nodes ARD <20%	ARD (%)	Fraction of nodes ARD <20%	ARD (%)	Fraction of nodes ARD <20%
K^{Trans}	1.48	99.18	20.66	73.77	14.96	86.88
v_e	1.15	100	11.86	83.61	15.07	83.61
v_p	5.63	97.54	11.06	86.88	15.6	86.88

In comparison, this test proved the robustness of the D-ETM PINN when facing ill-posed problems, getting 99% of the nodes below the ARD threshold with a mean ARD of only 1.5%, 10 times lower than the ETM.

A key point of these results is the ability of PINNs to accurately adjust v_e values in necrotic zones, where K^{Trans} takes values close to zero. Previous models and algorithms [40, 52] failed to retrieve accurately the distribution of v_e in those regions. This was caused by the vanishing effect observed in the gradient of C_t with respect to v_e, since this gradient was dependent on the K^{Trans} value. Therefore, when K^{Trans} tends to zero, the gradient does the same, causing the algorithm to converge to a local minimum. Thanks to the RAR method, PINNs are able to

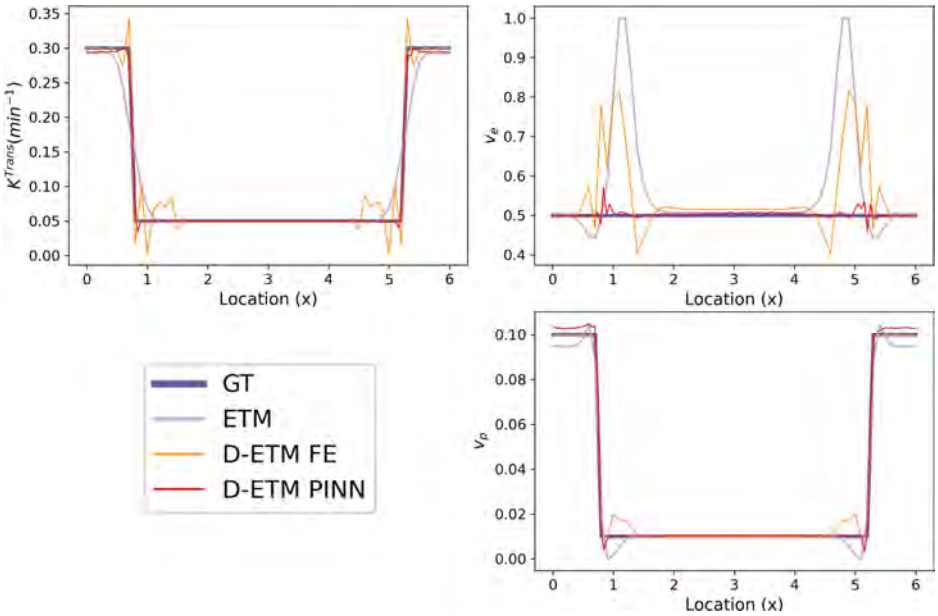

Figure 4.2: Homogeneous case, location values expressed in mm. Reference values and results of the D-ETM (with both methods, FE and PINN) and the ETM fitting. Results highlight the limitation of the ETM when faced with significant diffusion gradients, tending to average the K^{Trans} along that region. They also show the improved accuracy of the D-ETM PINN with respect to the D-ETM FE. While the latter converges to a local minimum, as described in the previous chapter, the former retrieves accurately the distribution of parameters.

reduce this vanishing effect, overcoming the convergence issues and achieving great accuracy for v_e in necrotic regions.

4.3.2 Heterogeneous distribution of parameters

The second set of simulations corresponded to the same 1D domain of a circular tumor, but defining heterogeneous distributions of parameters. This case aims to resemble more closely to a real tumor where some degree of heterogeneity is present.

Results obtained are consistent with previous works [40, 41, 52]: the ETM tends to average the parameters distribution, failing to capture the heterogeneity shown in Figure 4.3, while the two implementations of the D-ETM (FE and PINN)

accurately depict this heterogeneity (Table 4.2).

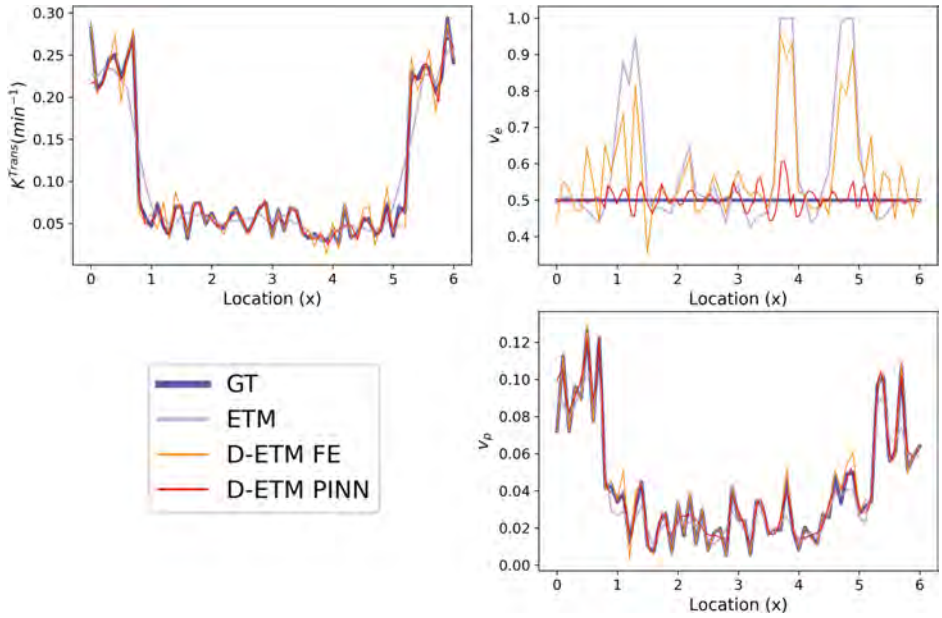

Figure 4.3: Heterogeneous case, location values expressed in mm. Reference values and results of the D-ETM (with both methods, FE and PINN) and the ETM fitting.

This effect is of particular significance in the case of the v_p, where only 46% of nodes fitted by the ETM show an ARD lower than 20%. This metric raises to 84% and 91% in the case of the PINN and FE implementations of the D-ETM. While the PINN method shows a slightly greater error for v_p, it outperforms the D-ETM FE in the case of K^{Trans}, with 94% of nodes below the ARD threshold versus 78% in the case of the D-ETM FE. The averaging effect shown by the ETM has a clear impact on the K^{Trans} error metrics, having only 52% of nodes with and ARD below 20%.

Regarding v_e, results are similar to the homogeneous case: both the ETM and the D-ETM FE fail to retrieve the v_e distribution. Although around three quarters of nodes are below the ARD threshold, Figure 4.3 shows that in some nodes the ARD value is close to 100%. This can be explained by the vanishing effect explained previously, which prevents the D-ETM FE to converge to the solution. Again, the D-ETM PINN overcomes this issue and gets more than 98% of values below the ARD threshold, keeping the maximum ARD value below 25%.

It is worth noting that despite this good error metrics, the D-ETM PINN shows

Table 4.2: Error metrics comparison between the D-ETM (FE and PINN methods) and the ETM for the heterogeneous case. The two metrics computed are the mean ARD and the fraction of nodes whose ARD is below the defined threshold of 20%. These metrics were computed from a set of 10 simulations with different heterogeneous distributions of parameters.

	D-ETM PINN		D-ETM FE		ETM	
	ARD (%)	Fraction of nodes ARD <20%	ARD (%)	Fraction of nodes ARD <20%	ARD (%)	Fraction of nodes ARD <20%
K^{Trans}	6.68	94.26	13.53	78.33	25.5	52.46
v_e	3.52	98.36	18.74	72.13	22.04	77.05
v_p	11.20	84.43	5.76	91.8	34.02	45.9

some kind of smoothing or averaging patterns in some regions of the spatial domain, especially for v_p. This is probably due to the different effect these parameters have on the cost function depending on the algorithm. While in the case of the D-ETM FE the C_t curves depended on the parameters value through a forward FE simulation (see Chapter 3 for further details), therefore increasing the impact of PDE parameters (mainly v_p) on the cost function; in the case of the D-ETM PINN the PDE parameters only impact part of the loss function ($\mathcal{L}_\mathrm{r}$ and $\mathcal{L}_\mathrm{C}$). Therefore, there can be small errors on the PDE parameters distribution while the total loss value $\mathcal{L}$ is minimized, since the data loss ($\mathcal{L}_\mathrm{d}$) is being reduced by updating the NN parameters (θ).

4.4 Testing the robustness of the PINN method against noisy and incomplete data

After demonstrating the increased accuracy of the D-ETM PINN with respect to the D-ETM FE, we test its robustness when faced with noise and incomplete temporal data.

4.4.1 Influence of noise

Initially, a set of 1D heterogeneous distributions of parameters similar to those presented in Figure 4.3 were generated. Next, experimental noise was added to the generated C_t data curves using a Gaussian distribution with an SD equal to a fraction (2.5%, and 5%) of the highest concentration value reached in the whole domain, as in the previous chapter. [40, 52].

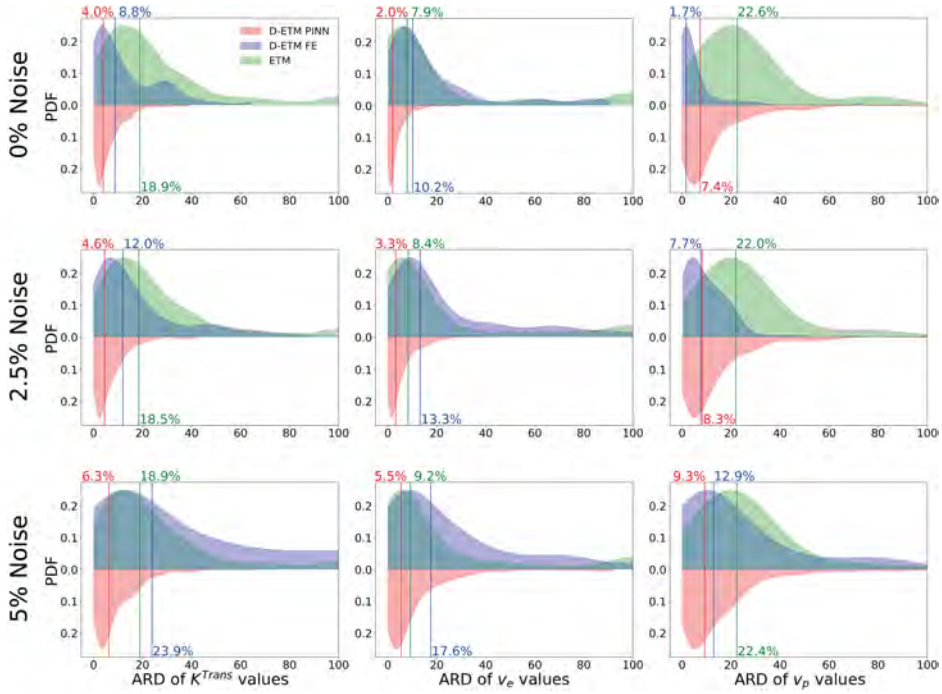

Figure 4.4: Violin plots comparing the ARD probability density function (PDF) of each of the parameters for each of the models and three different level of noise: 0%, 2.5% and 5%. Vertical lines correspond to the median of the ARD distributions. The D-ETM PINN is much more robust to noise compared to the D-ETM FE, while the ETM does not seem affected by noise.

The ARD distributions for each of the parameters and each model are shown in Figure 4.4. These results show that the D-ETM PINN is much more robust to noise than the D-ETM FE, even in the case of v_p. When faced with medium levels of noise, both methods show similar ARD for this variable. However, when the noise level reaches 5%, the D-ETM PINN is more accurate than the D-ETM FE.

The results of the other two variables follow this same trend: the influence of noise is much lower in the case of the D-ETM PINN compared to the D-ETM FE. The ETM, however, seems to be unaffected by noise, reaching a similar accuracy to the D-ETM FE for high noise levels (5%).

4.4.2 Temporal undersampling

In this final subsection, we investigated the impact of incomplete data on the accuracy of the ETM, the D-ETM FE, and D-ETM PINN. To achieve this, we conducted a temporal undersampling analysis on both the concentration data curves and the AIF. Specifically, we considered two scenarios where the temporal resolution was reduced to 5 seconds and 10 seconds, respectively. The aim of this analysis was to simulate realistic situations in which the temporal resolution may deviate from the ideal resolution of 1 second used in our previous tests.

Table 4.3: Error metrics comparison between the D-ETM (FE and PINN methods) and the ETM for the case with a temporal resolution of 10s. The two metrics computed are the mean ARD and the fraction of nodes whose ARD is below the defined threshold of 20%. distributions of parameters.

	D-ETM PINN		D-ETM FE		ETM	
	ARD (%)	Fraction of nodes ARD <20%	ARD (%)	Fraction of nodes ARD <20%	ARD (%)	Fraction of nodes ARD <20%
K^{Trans}	8.02	93.44	44.34	40.98	46.23	52.46
v_e	8.44	89.34	35.22	50.82	17.07	80.32
v_p	18.56	67.20	55.52	18.03	46.23	14.75

Our results, presented in Figure 4.5, revealed that the ETM was almost unaffected by the undersampling, except for the v_p variable, which was more sensitive to it. Conversely, the D-ETM FE performed well at a temporal resolution of 5s, but its performance degraded when the temporal resolution was further reduced to 10s, resulting in higher errors than the ETM.

Interestingly, the D-ETM PINN demonstrated superior performance, even under the worst-case scenario of a 10s temporal resolution. As shown in Table 4.3, the D-ETM PINN outperformed both the D-ETM FE and the ETM, with 93% and 89% of nodes having an ARD lower than the 20% threshold for K^{Trans} and v_e, respectively. This was almost twice the proportion observed for the ETM and the D-ETM FE. Even in the case of the sensitive v_p variable, the D-ETM PINN maintained a relatively high proportion (67%) of values below the ARD threshold, in comparison to the D-ETM FE (18%) and the ETM (15%).

In summary, our findings suggest that the D-ETM PINN is more robust to incomplete data and performs better than both the ETM and D-ETM FE under these conditions. The ETM performs reasonably well except for the v_p variable, while the D-ETM FE shows good performance at a 5s temporal resolution but underperforms with further undersampling.

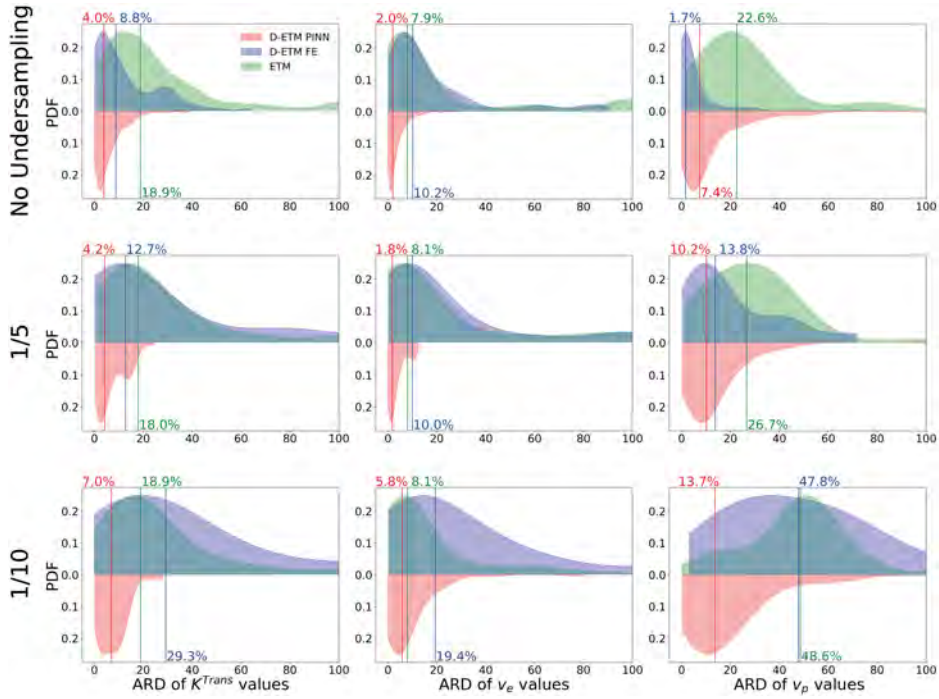

Figure 4.5: Violin plots comparing the ARD probability density function (PDF) of each of the parameters for each of the models over three different time resolutions: 1s (No undersampling), 5s (1/5) and 10s (1/10). Vertical lines correspond to the median of the ARD distributions. The D-ETM PINN outperforms the other two, showing great robustness even in the worst scenario.

4.5 Discussion

DCE-MRI is a powerful imaging technique widely used in clinical practice, particularly in oncology, to assess the vascular properties of tissues. The ability to obtain functional information about tumors using DCE-MRI has been proven to be useful for diagnosing, staging, and monitoring tumors' response to antiangiogenic therapies [53–55]. However, accurately retrieving physiological parameters from DCE-MRI is a challenging task due to the complex and nonlinear nature of the underlying pharmacokinetic models. Traditional models, such as the STM and the ETM, have been widely used to estimate these parameters but are known to produce inaccurate results in regions where passive delivery of CA plays an important role [40–44, 46, 47, 52]. Other authors have proposed different ap-

proaches that include the diffusion of CA and have developed several methods to fit their models to DCE-MRI data. Nevertheless, these models and methods either have a limited applicability due to the hypothesis and assumptions considered or due the convergence issues and the computational cost of the algorithms. Therefore, there is a critical need for new methods that can retrieve more accurate parameters from DCE-MRI data.

The main objective of this chapter was to explore the use of PINNs as an alternative to other traditional algorithms to fit one of the models that include the diffusion term: the D-ETM. To do so, we tested the performance of this PINN approach versus the FE-based optimization algorithm presented in the previous chapter. Both methods were compared to the ETM to highlight the importance of diffusion in CA delivery.

These three approaches were tested on a 1D domain that was inspired in literature and whose design resembles a slice-cut of a circular tumor with a highly vascularized rim and a necrotic core. This geometry aims to highlight the effects of CA diffusion, creating large spatial gradients of CA concentration between the two regions.

Our results indicate that PINNs are a promising tool to solve the ill-posed inverse problems associated with the fitting of the D-ETM to DCE-MRI data. The PINN-based approach kept almost all nodes in the domain below the acceptable error threshold. Previous algorithms, such as the FE-based presented in Chapter 3, failed to retrieve the v_e distribution in necrotic regions, due to a low influence of this parameter on the global solution. However, the use of PINNs along with the RAR method overcome this limitation, keeping almost all the nodes within the acceptable error range, outperforming traditional algorithms. Even in the homogeneous case, where the FE algorithm converged to a local minimum, the PINN approach depicted accurately the distribution of all the parameters.

To further demonstrate the robustness of PINNs to solve this ill-posed inverse problem, we tested its performance in the presence of noisy and incomplete data. The results obtained show that the PINN was affected to a much lower extent than the FE algorithm, retrieving very accurate distributions of D-ETM parameters. Taking a look at the error distribution for each of the three approaches tested we could conclude that PINNs combine (and even increase) the precision of the FE algorithm with the robustness of the ETM against noisy and incomplete data.

Despite the promising results obtained with the PINN approach, there is still room for improvement. First, in this study we did not perform a comprehensive hyperparameter tuning, which may have resulted in suboptimal performance.

Future studies should focus on optimizing the PINN hyperparameters to further improve its performance [106]. Second, there are other additional features of PINNs that have been described in the literature that were not included in our study. These may include the use of gradient-enhanced PINNs [105], the inclusion of annealing algorithms to update each loss weight (w_i) or new NN architectures optimized for PINNs [107]. Incorporating these features in future studies may further enhance the accuracy and robustness of the PINN approach while reducing the training time.

The main limitation of our methodology is the lengthy training time required for the PINN. Our simulations were conducted on a PC equipped with a NVIDIA RTX 3070 GPU, 32 GB RAM, and an Intel i7-11700K CPU, with an average training time of approximately 1 hour. This is much slower than the current FE algorithm, which only took an average of 20 minutes on the same PC. Meanwhile, the NLLS algorithm used for the ETM required only a few seconds to fit all nodes in the domain, so it cannot be directly compared to either of our methods. To address this limitation, proper calibration of the PINN may help to reduce the training time. Additionally, transfer-learning techniques [108, 109] can be applied to further lower the computational cost.

This study demonstrates the capability of PINNs to overcome convergence issues when fitting the D-ETM to DCE-MRI data, outperforming previous algorithms. This work lays the foundation for further research that improves our implementation and optimizes it for its application to 2D cases.

Chapter 5

im2mesh: A Python library to reconstruct 3D meshes from scattered data and 2D segmentations

This chapter is based on:

D. Sainz-DeMena et al. "Im2mesh: A Python Library to Reconstruct 3D Meshes from Scattered Data and 2D Segmentations, Application to Patient-Specific Neuroblastoma Tumour Image Sequences". In: *Applied Sciences 2022* 12.22 (Nov. 2022), p. 11557

5.1 Introduction

Personalized medicine [111] is based on the idea that inter-individual variability conditions define how a certain disease affects each person and that specific actions can be tailored to the patients based on their predicted response or risks. In recent years, there has been a continuous growth in this field thanks in part to the improvements on medical imaging techniques, genetic data acquisition and clinical tools for disease diagnosis and prognosis [112–114].

In parallel, there has also been a notable development in *in silico* medicine, also known as "computational medicine", due to the huge technical advances and the availability of improved software and hardware that allows the simulation of increasingly complex and demanding problems. In the biomedical field, these simulations aim to provide additional information that helps to understand the intricacies of biological processes, which may be useful to develop tools to support clinical decisions [115]. Given the importance of personalized medicine, in particular for the treatment of cancer, researchers keep developing new *in silico* tools that account for individualized data, a field of expertise known as patient-specific modeling. These models simulate biological processes, often related to disease, using particular data from the patient. This combination of mathematical models and individualized parameters holds the key to a future, where digital twins might be used to improve the diagnosis and select the best possible treatment for a specific condition [49, 116, 117].

Despite the aforementioned advances made in its diagnosis and treatment, cancer is still the second most common cause of death in the world, being responsible for about one sixth of the total deaths [12]. It is a very complex and heterogeneous disease, due to the great number of biological and mechanical factors that control tumor growth, treatment efficacy and metastasis, among other processes. Differences arise not only between different types of cancer, but also among individuals afflicted by the same type.

Within this context of heterogeneity, patient-specific models constitute a great option to support decision making in the clinical management of the disease. There are several examples of tumor growth models that incorporate personalized data, often derived from imaging sequences, which can be MRI, computed tomography (CT), etc. [118–120]. Examples of these sequences include DWI and DCE in the case of MRI or dual energy computed tomography (DECT) for CT. They can be used to obtain insightful knowledge of the cellularity level (DWI) and vascularization (DCE and DECT) of the tissue, which are the main inputs for most of these tumor growth models.

To include this imaging data into a model, the first step is to incorporate the geometry of the tumor and, if available, of surrounding organs. Therefore, one should start by segmenting the ROI in one of the imaging series and then registering the other sequences to this segmented series, which is critical to have all imaging data (geometry, cellularity and vascularization data) in the same coordinate system. Regarding the segmentation task, there are several ways to segment the different tissues [121]. The first and most traditional way is manual or partially-assisted segmentation, where a professional (a radiologist in clinical practice) delineates the ROIs and generates the masks in every individual slice. Although very accurate, the process is time consuming and often infeasible when the number of cases is too large, which often leads to partial segmentations, where particular slices are skipped (i.e., when the object of interest presents no abrupt changes with respect to the previous segmented slice and the mask would be almost identical). This can be alleviated to some extent via semi-automatic segmentation, which applies statistical and ML methods to propose masks that need to be revised and manually corrected by an experienced professional [122, 123]. In recent years, the boom of artificial intelligence for image applications has laid the foundation for the development of algorithms that apply the power of DL to automate the task of segmentation with very promising results [124].

Regardless of the segmentation method used, the next step is reconstructing the original 3D geometry from the stack of segmented slices. This volume generation might be included in the own architecture of the DL network (such as U-Net [125]. Otherwise, a subsequent step of 3D reconstruction is needed. There is a wide range of methods to perform volume generation from a set of 2D slices [126, 127], some of them already included as features of popular software such as *3D Slicer* [128]. This process of segmentation and volume reconstruction culminates with the interpolation of the different image sequence data to the generated volumetric mesh. These interpolated maps together with the geometry constitute the necessary inputs for the construction of the patient-specific models previously described.

To illustrate this methodology, we present a practical use case within the PRIMAGE project (PRedictive In-silico Multiscale Analytics to support cancer personalized diaGnosis and prognosis, Empowered by imaging biomarkers) [129, 130], where the described workflow was used to generate patient-specific models in a large number of clinical cases

To put it into context, PRIMAGE is currently one of the largest and more ambitious European research projects in medical imaging, artificial intelligence and childhood cancer, in particular, Neuroblastoma (NB) and the Diffuse Intrin-

sic Pontine Glioma (DIPG). Its main goal is to develop a decision support system combining retrospective clinical information and incorporating it into the diagnostic pipeline using AI and computational models. One of the peculiarities of this project is the availability of tumor segmentations from hundreds of patients, which need to be processed and incorporated into an automatized workflow to simulate the tumor progression with patient-specific data. This decision support system will be integrated in an online platform and used by clinicians in their day-to-day practice, hence the necessity of self-contained tools (i.e., no extra software or technical parameter handling needed) that can be used via regular browsers. With this idea in mind, we developed *im2mesh*, which has no particular requirements other than an environment supporting Python 3.9 and can be executed both in bash mode (therefore integrated, for example, into an automatized cloud-based platform) and with a minimal user interface when used for research purposes. We would like to emphasize that *im2mesh* aims to be a tool for a very specific task: transforming segmented slices into 3D meshes (with or without interpolated data), that can be used as a connecting component between image data and simulations. Certainly, there are other well-established tools, such as *3D Slicer* (open software) or *Mimics* (Materialise, Leuven, Belgium), with big communities and a wide range of functionalities and versatility, but which are designed to be used as visual user-interactive tools rather than "black box" functions for automatization.

In this chapter, we describe in detail the proposed methodology. Then, we compare our 3D reconstruction with that obtained with *3D Slicer*, we analyse mesh quality, and we study the effect of downsampling (decreased number of slices) on geometry details. Finally, we analyse a clinical example taken from the PRIMAGE platform, corresponding to a NB tumor.

5.2 Materials and methods

In this section, we provide a summary of the developed workflow, describing in detail the algorithms and methods used for surface and volume generation. Finally, we provide the sources for the code, its documentation, and the data presented in this chapter.

5.2.1 Workflow

Our library accepts multiple image formats and input parameters that are prompted to the user either via command (bash-mode) or via visual interfaces. In par-

ticular, typical medical image formats such as NIfTI (.nii), DICOM and DICOM-SEG (.dcm), as well as regular image formats supported by *OpenCV* [131] can be used. The input stack, composed of any number (N) of slices or layers (previously segmented), is processed from bottom to top, interpolating shapes between every pair of layers. The contours of the original layers, plus the interpolated (virtual) ones, are stored for the surface mesh generation. Note that the inside points of the top and bottom layers of the whole stack are also included to obtain a closed surface, which is used later to obtain a 3D tetrahedral mesh. Optionally, a cloud of values (position coordinates plus scalar value) can be extracted from the medical files, or provided by the user, to be interpolated to the elements of this mesh. We include a last step that allows exporting the generated mesh to different formats appropriate for commercial Finite Element software commonly used in engineering such as *ABAQUS* (Dassault Systèmes, France) or *ANSYS*. A schematic representation of the workflow is shown in Figure 5.1.

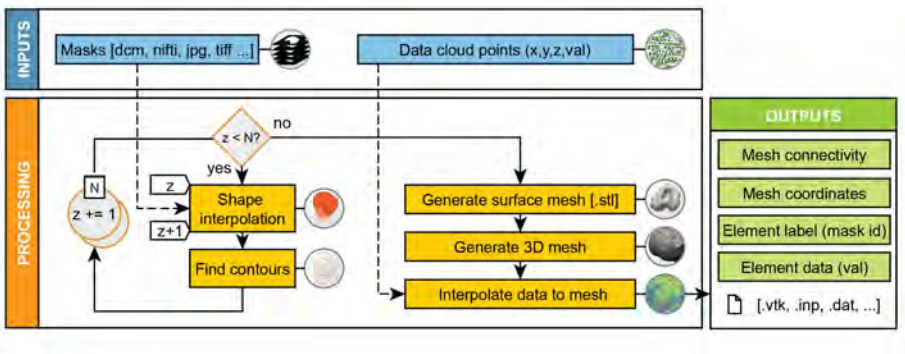

Figure 5.1: *im2mesh* workflow. Image files of multiple formats containing the segmentation masks are accepted as input for the mesh generation. For every pair of layers, starting from the bottom, shapes are interpolated using any number of intermediate positions. Afterwards, the contours of these shapes are computed and stored for later stages. When the interpolation is complete, a surface mesh with the desired number of faces is created (.stl) and further processed to obtain a volumetric 3D mesh in which scalar data is automatically interpolated if available (optional). Useful information (e.g., element labels, connectivity, coordinates, etc.) and already formatted mesh files are exported for further analysis.

5.2.2 Shape interpolation

Shape interpolation is performed by following the steps illustrated in the benchmark example shown in Figure 5.2, using the methodology described in [132]. The necessary inputs to interpolate between two layers are just the binarized representations (BW) of each layer. Firstly, the contour or perimeter of each layer is computed (BW_{per}), and the signed Euclidean distance (S_{edist}) between each pixel and the perimeter is calculated. This distance is equivalent to the regular Euclidean distance, but considered negative for pixels outside the perimeter, and positive for those inside (Figure 5.2A). Once the signed distances are computed for both layers, their values are linearly interpolated to any number of intermediate layers (Figure 5.2B left). The new layers are converted back to a binary image by thresholding negative values (Figure 5.2B right). This procedure is repeated between every pair of consecutive layers until the whole stack has been processed (Figure 5.2C). Finally, the contours of each of the binary layers are extracted using the *OpenCV* library [131] and their coordinates stored to form the superficial point cloud.

5.2.3 Mesh generation

Surface meshes (Figure 5.2D left) are generated via the Python library *PyMeshLab*, that in turn interfaces to the popular open-source application *MeshLab* [133], using as input a cloud of 3D points coming from the contours computed by the shape interpolation algorithm. To enhance the robustness of the algorithm (e.g., avoiding over-sensitivity of convergence due to a wrong ratio of the number of pixels per layer and number of intermediate interpolations), the cloud points are randomly sampled following the Poisson Disk sampling method [134], ensuring homogeneous spatial distribution. This algorithm takes as inputs an estimation of the number of points sampled, which is defined as a fraction of the number of points in the original cloud. Then, the algorithm computes the normals for the sampled point cloud and finally generates a closed surface based on these normals using the Screened Poisson surface reconstruction method [135]. To improve the quality of the volumetric mesh to be generated afterwards, a decimating filter is added after the surface reconstruction. This filter is based on the quadric based edge-collapsed strategy [136]. Additionally, the generated surface can be smoothed (user-defined option) to simplify complex geometries that could be problematic for the subsequent volumetric meshing. We employ the HC Laplacian Smoothing [137] algorithm for this purpose. Three-dimensional meshes (Figure 5.2D middle) are then generated from the surface files (.stl) using

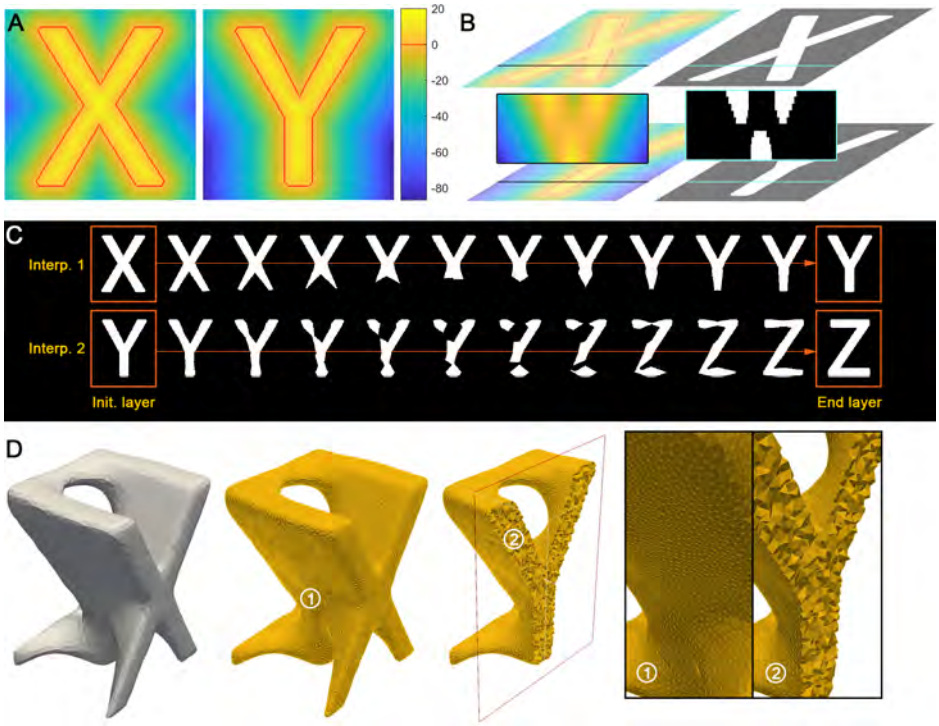

Figure 5.2: A whole-process demonstration example with an input of three binary layers representing the X, Y, Z letters. **A**. Signed Euclidean Distance map of the first two masks (X and Y shapes). Pixels inside the perimeter (red line) present positive distances, whereas exterior pixels are assigned negative values. **B**. Distance maps are interpolated in any number of intermediate layers (left vertical cut) and thresholded to return a binarized volume (1 if distance > 0; 0 otherwise). **C**. Interpolation of 10 intermediate positions (equally distributed) between input and output layers. **D**. Surface mesh reconstruction (.stl format) (left panel), and 3D tetrahedral mesh generated with a transversal cut (middle panel). Insets 1 and 2 show the smoothness and good quality of the elements (right panel).

the open-source library *Gmsh* [138] which provides a great flexibility.

5.2.4 Evaluation metrics

To prove the robustness and accuracy of our algorithm with respect to other well-established software [128], we compare the surface meshes generated. The metric used for this comparison is the Intersection over Union (IoU), defined as:

$$IoU = (A \cap B)/(A \cup B) \tag{5.1}$$

Where A and B are two different volumes enclosed by the generated surface meshes. The IoU is 1 when both objects are equal and overlap totally. It should be noted that, unlike in the computer vision field, the registration step can be skipped since our volumes are aligned in the 3 spatial axes, which simplifies the computation of the IoU considerably. We also perform an analysis of the quality of the volumetric mesh obtained from *Gmsh*. For this purpose, we have chosen two arbitrary metrics: the Aspect Ratio (AR) and the Aspect Frobenius (AF) [139], which compute how far the analysed mesh is from an ideal mesh. The AR is defined as the ratio of the maximum edge with respect to the radius of the element's inscribed sphere:

$$AR = max(x_1, x_2, ..., x_6)/2 * \sqrt{6} * r \tag{5.2}$$

Where x_1 to x_6 are the length of the edges in a tetrahedron and r is the radius of the sphere inscribed in the tetrahedral element. The AF of an element is the normalized Frobenius condition number of matrix A_0. The mathematical expression for the Frobenius condition number of an element is:

$$|A_0|_F = \sqrt{(tr(A_0^T A_0))} \tag{5.3}$$

Where $A_0 = T_0 W^{-1}$. T_0 is the edge matrix of the tetrahedral element and W is the edge matrix of the reference regular tetrahedron. Both metrics are normalized, i.e., they equal to one when the element analysed is the ideal regular element. According to other authors [139], acceptable ranges are [1,3] and [1,1.3] for the AR and AF, respectively.

5.2.5 Data interpolation

Once the FE mesh is generated, the additional imaging data that may be available must be interpolated to this mesh. Most patient-specific models, especially tumor growth models, need as inputs not only the geometry, but also other spatial

distributions of properties that describe the heterogeneous characteristics of tumors. In the case of PRIMAGE, this additional data was obtained from DWI and DCE sequences, respectively. These MRI sequences are commonly used in clinical practice to evaluate the cellularity and vascularization of the tumors. The cellularity values are derived from the Apparent Diffusion Coefficient maps generated from DWI sequences [140], while the vascularization is obtained from the analysis of DCE sequences, as we have explained in previous chapters. Apart from these sequences, there are many other techniques to obtain different imaging data that might be included in the FE mesh. Therefore, our code includes a script to read any kind of data derived from imaging that is stored in NIfTI and DICOM formats and interpolate it to any FE mesh given. The interpolation process begins by transforming the imaging data to be interpolated from voxel coordinates to global coordinates using the affine matrix of each imaging sequence. Then, we use the *Scipy* [141] python library to interpolate the spatial data to the elemental centroids of the mesh generated previously, exporting this interpolated data to an additional file that can be used as input for subsequent computational models.

5.3 Results

This section is divided into three different parts. In the first one, we compare our library to *3D Slicer* software by reconstructing a human pelvis using both methods and measuring the differences. The next part covers the effects of reducing the number of available slices in the segmentation (what we define as *downsampling*) using the same example. Finally, we show the application of the workflow summarized in Figure 5.1 on one of the NB cases available in the PRIMAGE project dataset.

5.3.1 Volume reconstruction

In this section, our library is used to reconstruct a pelvis (plus part of the femurs) from a partial segmentation obtained from the Cancer Imaging Archive public repository and compare it to that obtained using the software *3D Slicer*. Figure 5.3 shows the surface volume reconstructed after processing a 512x512x300 volumetric image both with *im2mesh* (Fig 5.3A orange, left) and *3D Slicer* (Fig 5.3A blue, right). Visual differences between both surfaces are minimal (Fig 5.3B), as confirmed by a IoU score of 98.6%. Note that the overlap is not perfect due to slight differences in triangulation and surface smoothing. In fact, our library uses a decimation filter that decreases the number of surface triangles to reduce the

computational cost of the volumetric meshing algorithm applied afterwards. Figure 5.3C shows the visual effect of decimation: 5M triangles (left) vs 50k (right). The IoU score attained between the enclosed volumes was 97.3%.

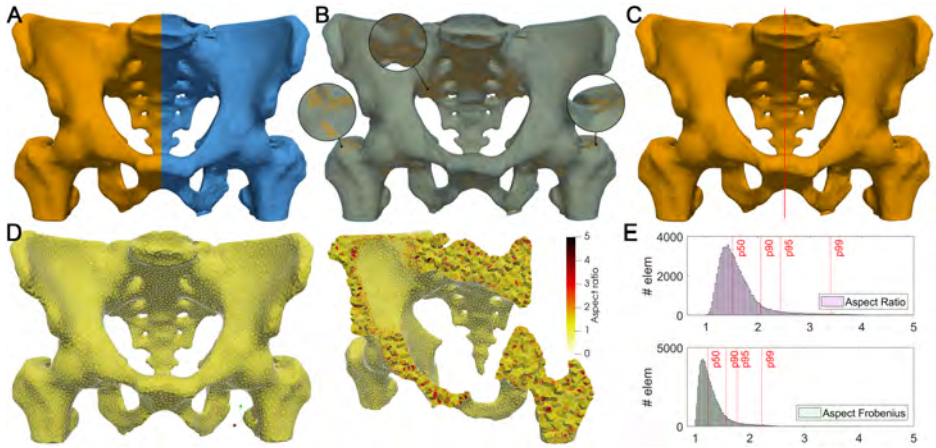

Figure 5.3: Reconstruction of the partial segmentation of a human pelvis. **A**. Reconstruction of the pelvis using *im2mesh* (left, orange) and *3D Slicer* (right, blue). **B**. Volumetric overlap of the two reconstructions with decreased opacity for better visualization (same colors). Insets highlight the zones where differences are more noticeable, corresponding with rough areas where the smoothing and triangulation algorithms play a bigger role. Nonetheless, the IoU score attained was 98.6%. **C**. Effect of decimating on the triangulated surface mesh: 5M triangles (left) vs 50K (right). Despite visually reducing the smoothness, the IoU score attained (50k vs 5M) was 97.8%. **D**. Volumetric mesh generated with 5 mm objective element size (total number of elements: 72694), colored by AR, showing very high quality (>90% of the elements in the 1-2 range). **E**. Value distribution of the AR and AF metrics for mesh quality assessment. Vertical red lines mark the 50, 90, 95 and 99 percentiles respectively. Additional mesh quality metrics of the pelvis mesh are presented in Table 5.1.

Finally, the closed surface obtained from *im2mesh* is meshed using linear tetrahedrons with 5 mm objective element size (Figure 5.3D). The mesh quality was evaluated using the Verdict geometric quality library [139], obtaining the results presented in Table 5.1. The analysis shows that most of the elements are within the recommended range for the metrics. Note that the suggested range is indicative and does not mean that elements out of the range would prevent the use of the mesh for FE simulations. Only 1% of elements show an AF more than 50% above the maximum recommended value and 10% are less than 50% above this limit. These results are acceptable, given the complexity and coarseness of

the mesh. Besides, the metrics were proven consistent over different parameterizations of the algorithm and different geometries.

Table 5.1: Mesh quality metrics of the pelvis mesh shown in Figure 5.3D obtained using the Verdict library. The first three columns correspond to the mean, standard deviation and median of each metric over the whole mesh. The next three columns are the 90%, 95% and 99% percentiles of each metric, respectively. Finally, the last two columns show the minimum and maximum limits of the recommended intervals for each metric.

Metric	Mean	Std. Dev.	Median	p90	p95	p99	Rec. Min	Rec. Max.
Aspect Frobenius	1.289	0.2338	1.225	1.566	1.76	2.216	1	1.3
Aspect Gamma	1.48	0.4319	1.356	1.96	2.335	3.298	1	3
Aspect Ratio	1.616	0.42	1.514	2.054	2.434	3.3397	1	3
Condition	1.323	0.3268	1.226	1.65	1.985	2.785	1	3
Edge Ratio	1.712	0.3086	1.647	2.141	2.293	2.595	1	3
Jacobian	131.8	53.75	125.4	205.1	230.4	279.6	1E-30	1E30
Min. Dihedral Angle	49.11	12.12	50.36	63.63	67.04	73.56	40	70.53
Aspect Beta	1.381	0.3495	1.28	1.759	2.065	2.888	1	3
Scaled Jacobian	0.5656	0.1535	0.5736	0.7632	0.8064	0.8777	0.5	0.7071
Shape	0.7962	0.1156	0.8161	0.9273	0.9477	0.9744	0.3	1

The distributions of AR and AF metrics on this mesh (Figure 5.3E) show that more than 95% of the elements are within the acceptable range for AR and about 65% of them fall inside the acceptable range of AF. Given the complexity of the geometry and the size of the elements, these metrics confirm the good performance of the *Gmsh* mesher on the reconstructed volume. Additional mesh quality metrics of the pelvis mesh are presented in Table 5.1.

5.3.2 Effect of downsampling

The main advantage of slice interpolation is the lower number of segmentations required to reasonably reconstruct a volume, at the price of losing detail at specific zones that might be important in the post-processing. We reconstructed the same geometry described in the previous section but using just 10% and 5% of the available slices (that is, 30 and 15 slices from 300 respectively, equally spaced). Despite significantly reducing the number of slices, our algorithm could reconstruct the bone structures with reasonable accuracy (Figure 5.4A). Note that a certain degree of detail loss due to downsampling is unavoidable, since the features defined in the removed slices cannot be reconstructed (Figures 4B to 4D). We computed the IoU metric over the original and downsampled reconstructions of the pelvis to measure the accuracy of our algorithm when the number of slices is reduced. The IoUs obtained were 97.4% and 96% for the 10% and 5% downsam-

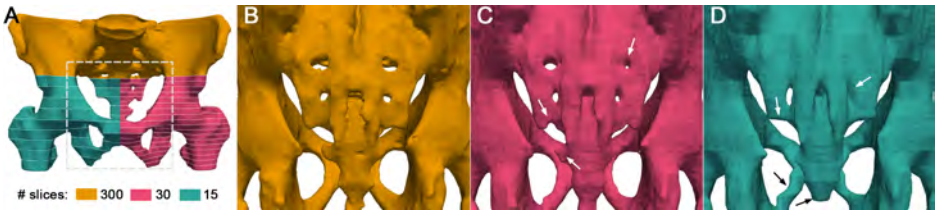

Figure 5.4: Effects of downsampling on the human pelvis example. **A**. A visual comparison of the reconstruction using all the slices (top, orange) versus a downsampling of 10% (30/300 slices used) (bottom right, pink) and a downsampling of 5% (15/300 slices used) (bottom left, blue). The dotted white square marks the region where we extract the detail for **B** to **D** after flipping the view for better visualization. **B**. Reconstruction of the coccyx without downsampling, downsampling of 10% (**C**) and 5% (**D**). Arrows on **C** and **D** highlight the loss of features with respect to **B** due to downsampling.

pling, respectively. This shows both the power and limitations of slice interpolation when dealing with cases with a reduced number of segmented slices or a very coarse slicing, which will ultimately depend on the practical case.

5.3.3 Application case

In this section, we apply the full workflow followed to prepare a real patient of NB tumor taken from the PRIMAGE platform to be used as input for a FE simulation. The patient presented a tumoral mass surrounding the mesenteric artery (Figure 5.5A) that was diagnosed via MRI. Additionally, the cellularity and vascularization maps for the tumor growth models subsequently developed were provided via DW- and DCE-MRI, respectively.

The tumor segmentation was firstly retrieved from the platform in a common medical image format, in this particular case, a NIfTI (.nii) file with 50 slices. Specifically, the size of the image volume was 512x512x50 voxels with a pixel size of 0.49x0.49 mm and a slice thickness of 5.5 mm. It is worth noting that the tumor was contained within 17 slices out of the 50, further restricting the geometric information available. The segmented stack was automatically processed to transform the slices into a cloud of points defining the surface of the tumor, using 10 intermediate positions to interpolate between slices.

This was enough to obtain smooth transitions and preserve fine details, such as the interior vases when obtaining the surface mesh (Figure 5.5B). It is worth

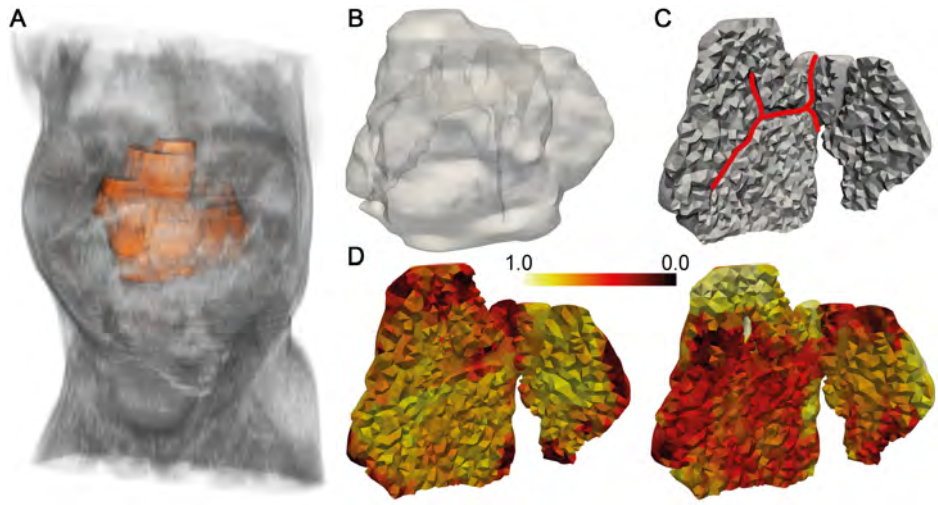

Figure 5.5: Application of the *im2mesh* library to one of the cases from the PRIMAGE dataset. **A**. Reconstruction of the tumor and the abdominal region of the patient using *3D Slicer* (whole stack of 50 slices). **B**. Surface mesh of the tumor generated using our library from the 17 slices containing the tumor. Through the semi-transparent surface, the mesenteric artery and some of its branches can be seen passing through the tumor. **C**. Volumetric mesh of the tumor with the aforementioned vessels highlighted in red. **D**. Normalized cellularity (left) and vascularization (right) maps interpolated from DWI and DCE sequences to the volumetric mesh presented in **C**.

noting that the reconstruction of the surface via *3D Slicer* in this particular case was suboptimal using the default values (see Figure 5.5A and Figure 5.6), as opposed to *im2mesh* which generated a smoother surface. The 3D mesh was subsequently computed (Figure 5.5C), and the cellularity and perfusion maps interpolated to its elements (Figure 5.5D), closing the process and readying the necessary files to be further processed by any FE software.

We evaluated the performance of the algorithm and workflow proposed using different combinations of parameters on the neuroblastoma geometry. The code was executed in a workstation with the following technical specifications: Intel(R) Core(TM) i7-5820K CPU @3.30GHz, 32GB RAM. We selected three main parameters to analyse their influence: mesh element size, number of interpolation steps between slices (number of intermediate virtual slices) and number of faces on the STL surface mesh (Table 5.2). The higher these values, the more refined mesh and smooth geometry it is achieved, at a cost of longer processing times (Figure 5.7).

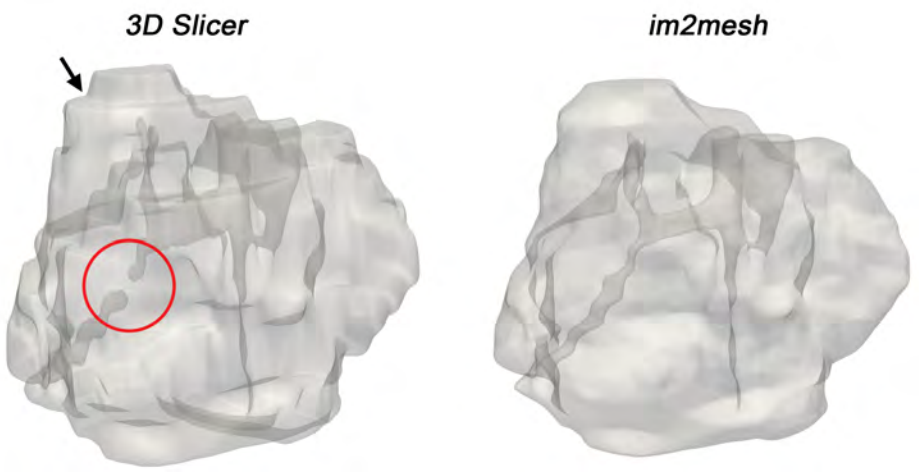

Figure 5.6: NB tumor reconstruction from 17 slices using *3D Slicer* (default values, no filters applied) and *im2mesh*. Note that without any user intervention (i.e. mask correction, filter application) *3D Slicer* produces a more staggered geometry (black arrows). This is due to the morphological contour interpolation algorithm used by the software which was developed to avoid over-smoothing and preserve the exact topological details of the geometry. This algorithm works therefore very well when the slice thickness is low (higher density of slices) but is less suitable when the number of slices is scarce, as it is the case of most of the data available within the PRIMAGE dataset.

Table 5.2: Combinations of parameters used for the eight test cases generated for the timing analysis of the proposed workflow. The third column is not an input but the number of elements contained in the mesh automatically generated using the goal size specified by the second column. The fourth column is the goal number of faces specified (the final number of faces may deviate slightly from this number).

Test Case	Element Size	No. of Elements	STL Faces	No. of Interpolation Steps
Test 1	1.5 mm	422,699	50,000	15
Test 2	1.5 mm	432,399	100,000	15
Test 3	1.5 mm	438,848	50,000	25
Test 4	1.5 mm	434,337	100,000	25
Test 5	3 mm	64,324	50,000	15
Test 6	3 mm	65,667	100,000	15
Test 7	3 mm	68,665	50,000	25
Test 8	3 mm	69,002	100,000	25

In summary, the results obtained show that the bottleneck occurs at the extraction of mesh element centroids in those cases where the number of elements is higher (cases 1-4). This is due to the fact that element (connectivity) and nodal data (coordinates) must be combined in an inefficient iterative process that does not scale linearly. It must be noted, however, that centroid extraction is optional and only needed if the user wants to interpolate data to the mesh. If the user only needs to retrieve the meshed geometry from the images, they can skip this step and complete the whole execution in less than 2 minutes.

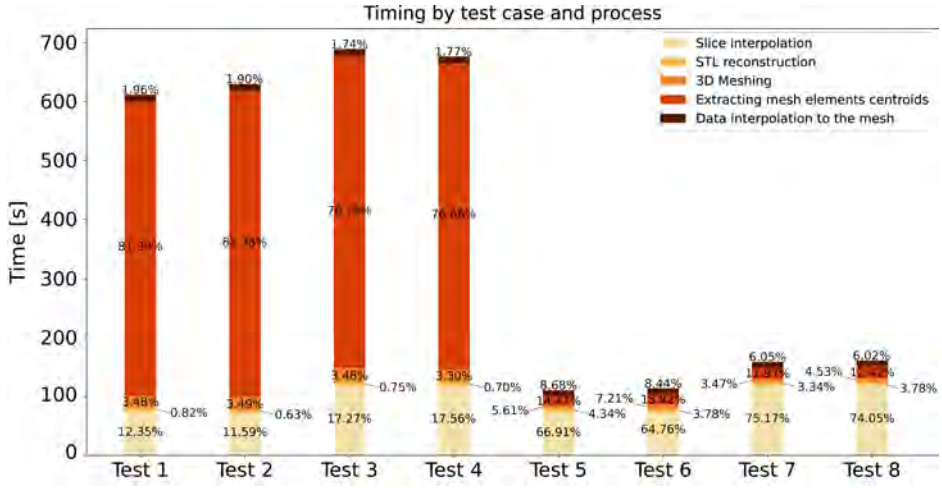

Figure 5.7: Analysis of the computation time for each test case separated by each of the processes. First four cases correspond to the finer mesh (around 430,000 elements) and the last four correspond to the coarser mesh (around 65,000 elements). These results clearly show that the extraction of the centroids of the elements is the bottleneck in the case of the finer meshes, accounting for more than 75% of the total computational time.

5.4 Discussion

The increasing importance of patient-specific models in the study of different pathologies reveals the need of simple and effective methods to generate inputs appropriate for these models. There is a wide range of software, both commercial and open-source, that can reconstruct surface meshes from segmentations, some of them providing tools to perform semi-automatic or automatic segmentations of a given set of images [128, 142, 143]. These programs and libraries, although powerful, cannot be easily included in automatic pipelines that aim to

process large sets of cases to generate inputs for computational models, most of them lacking the modules needed to generate volumetric meshes. To the best of our knowledge, there is only one open-source library that performs the full reconstruction from imaging data to volumetric mesh: the *dicom2fem* library [144, 145].

It includes semi-automatic segmentation prior to reconstruction, however, it is limited to DICOM files, lacking the option to use other formats or already-segmented sets of images. Our library does not include a segmentation module as we consider that such a problem-specific task (e.g. hard vs soft tissue, different image acquisition techniques, etc.) can be performed using more powerful tools (i.e. AI based), nowadays in constant improvement and development. We believe that being able to easily blend with these tools as a piece of a grander scheme may be very useful in the near future of personalized medicine. For this reason, we have developed *im2mesh* putting together different functionalities based on open-source libraries with the aim of facilitating the process of input generation for computational models from segmented images. This out-of-the-box solution automatically creates the desired files without user intervention, making it ideal for its integration into complex workflows.

We have shown the robustness of the tool as well as the potential and limitations of volume reconstruction from segmented slices. In fact, our methodology is able to reconstruct volumes almost identical to those obtained with the well-established and powerful tool *3D Slicer*. For now, *im2mesh* is limited to interpolation in the z-direction, which is the most common case in biomedical imaging, although interpolation in the other directions could be easily added in a future release. It is worth mentioning that slice interpolation is an ill-posed problem, firstly because there is no unique solution to it and secondly because there is no metric to quantify the accuracy of an interpolated sequence unless the objective volume is known beforehand, which would make the interpolation unnecessary. Nonetheless, the technique is very effective especially when the anatomy change vs slice density ratio is low (i.e., when adjacent slices are similar). In some instances where the geometry is extremely heterogeneous and the image resolution is limited (such as the NB tumor cases available within the PRIMAGE project), slice interpolation is just the simplest and most practical solution. In sum, our method has proved to be effective for automating the generation of inputs for tumor growth computational models, facilitating the integration of patient-specific simulations on the PRIMAGE web-based platform, in which *im2mesh* acts as a "black box" function that connects the patient's data with the simulation framework without user intervention. However, the proposed workflow can be easily generalized to other datasets, since the basic input needed by our library is the

path to the folder containing the image files. In fact, *im2mesh* is being used in another ongoing project, ProCanAid (PLEC2021-007709), which aims to create digital twins for the *in silico* study of prostate cancer. In this project, the tumor zone and different parts of the prostate are segmented using both automatic and semi-automatic methods. This difference in the input format (multiple masks within the image file) is easily overcome by tweaking some of the library parameters.

Our library is oriented and limited to work with already segmented images but its modularity allows a straightforward connection, for example, to a pre-processing pipeline of automatic segmentation based on DL or any other sophisticated and problem-tailored methodology.

5.5 Conclusions

It is clear that the future of personalized medicine lies in the development of increasingly sophisticated digital twins, where the patient-specific data can be used to assess not only the current state of a disease, but also its possible progression via predictive computational models. Although there are plenty of great available tools to curate and manipulate medical image data that serves as input of such models, the reality of this research field is that final users, the clinicians, don't have nor access nor the time to deal with complex workflows that rely on multiple software. Hence, all-in-one approaches serving as connectors in broader pipelines, such as the library presented in this chapter, will be a necessity for future platforms that aim to be integrated in the day-to-day clinical practice. In particular, *im2mesh* is currently integrated within the PRIMAGE web-based platform, but a standalone ready to use version is available, both in our GitHub and the community Python distribution repository (callable via pip) for public use and straightforward connection to any pre-existing pipeline.

Chapter 6

Conclusions

6.1 General conclusions

This chapter presents the key findings that have emerged from the development of this dissertation and outlines the possible future directions that could build upon the work carried out in this study.

The main objectives of this dissertation have been the development of new models and methods to improve the precision of vascularization data extracted from DCE-MRI sequences and the implementation of a new tool that automates the creation of patient-specific models from imaging data. With this purpose, we have first proposed a new formulation for a PK model that includes CA diffusion into the analysis of DCE-MRI sequences. Then, two different approaches have been developed to solve the inverse problem of fitting this new model to DCE-MRI data. The first of them proposes a gradient-based method that uses the FEM to calculate the gradient semi-analytically, surpassing by far the efficiency of numerical methods for the calculation of the gradient. The second approach studies the potential of DL techniques to solve this inverse problem. More specifically, the use of PINNs was evaluated, obtaining promising results. Finally, a new Python library was developed to automate the process of generating 3D FE meshes for patient-specific modeling and the integration of clinical imaging data in them.

The main conclusions are grouped by chapters and can be summarized as follows:

- **Chapter 2**: The diffusion-corrected Extended Tofts Model
  - As opposed to most of previous models, this new formulation does not assume that CA diffuses freely through the RVE face. In this model we consider that depending on cellularity, this diffusion may be limited to a fraction of this face.
  - By using the concept of effective diffusivity to define the diffusive term of the model, we pose diffusivity as an unknown and heterogeneous coefficient, which can take a different value in each RVE. Thanks to this approach, we can define the coefficient as a function of another variables already existing in the model, so we do not increase the number of unknown parameters.
- **Chapter 3**: A FE-based optimization algorithm
  - Dynamic contrast-enhanced MRI (DCE-MRI) is a useful imaging technique for assessing the vascular properties of tissues, particularly in oncology. Accurately retrieving physiological parameters from DCE-MRI is challenging due to the complex nature of PK models.
  - The simulations confirmed that the STM and ETM have limitations in estimating K^{Trans} and v_e accurately when CA reaches the ROI through passive delivery, and in regions where the active delivery of CA is low or non-existent.
  - The D-ETM used in this study shows improved accuracy in estimating K^{Trans} and v_e parameters, accurately depicting the heterogeneous distribution of values, and with smaller errors obtained for most of the nodes compared to the ETM model.
  - In comparison with previous works that used stochastic algorithms to solve the inverse problem [40], this method is several times faster, avoiding any additional simplification that reduce its range of application.
  - Despite its good results, this model shows a lower accuracy in the v_e maps, as in the case of the DP model [40]. This effect is particularly visible in necrotic areas, where there is hardly any vascularization. This means that v_e has almost no influence on the solution, and therefore on the gradient, causing it to fit poorly.
- **Chapter 4**: Exploring the potential of PINNs
  - The PINN approach outperformed the FE-based algorithm proposed in Chapter 3 in retrieving accurate parameter distributions. This new

approach showed an increased robustness in the presence of noisy and incomplete data with respect to the FE-based method.
  - The PINN approach was able to accurately fit the v_e distribution within the necrotic regions, overcoming the limitations of previous methods, both stochastic and gradient-based.
  - The initial formulation of PINNs proposed by Raisi *et al.* [87] was insufficient for this inverse problem. Additional features, such as loss weighting and residual based adaptive refinement (RAR) had to be included to improve its accuracy.

- **Chapter 5**: A Python library to reconstruct 3D meshes from clinical data
  - Patient-specific models are becoming increasingly important in studying different pathologies, requiring simple and effective methods to generate appropriate inputs for these models.
  - *im2mesh* is an out-of-the-box solution that automates the process of input generation for computational models from segmented images and creates the desired files without user intervention, making it ideal for integration into complex workflows.
  - All-in-one approaches serving as connectors in broader pipelines will be necessary for future platforms that aim to be integrated into day-to-day clinical practice. Although *im2mesh* is currently integrated within the PRIMAGE web-based platform, it is also available as a standalone ready-to-use version for public use and straightforward connection to any pre-existing pipeline.

6.2 Future lines of work

The findings presented in this work highlight the increasing importance of patient-specific models and the need for simple and effective methods to generate accurate inputs for these models. With this in mind, there are several potential model extensions and future avenues of research that could be explored. The possible lines of research are grouped in two sections: the first one is related to extracting more accurate parameters from DCE-MRI and the second one deals with the development of new tools for the generation of patient-specific models.

- Including CA diffusion into the analysis of DCE-MRI

  Regarding the formulation of the model, the definition of the diffusion coefficient should be revised to enhance the influence of v_e on the gradient.

Thus, the gradient-based approach will be able to compensate for the fading effect observed in necrotic areas that limited the accuracy when fitting this variable. Besides, in order to extend the range of application of the model and improve its accuracy, a convective term should be incorporated into the formulation in the future. To reduce the complexity of the model and facilitate the convergence of curve fitting methods, it would be possible to start from an estimated value of interstitial fluid velocity, avoiding the adjustment of this additional variable.

To further reduce the computational cost associated with the gradient computation, alternative methods could be implemented instead of the semi-analytical approach presented in Chapter 3. The best alternative is most likely the adjoint-state method to efficiently perform the inversion of the D-ETM equation. This method is particularly suitable for those cases where the gradient has to be calculated with respect to a large number of variables.

As an alternative to gradient-based methods, we have proposed a new approach based on PINNs. Despite the good results obtained on the synthetic cases tested, further work needs to be done to optimize the method and scale it to 2D *in silico* and clinical cases. Firstly, proper hyperparameter tuning is necessary to accurately calibrate the NN parameters, using either grid search methods, Bayesian optimization, or evolutionary algorithms. To minimize the computational cost of the training step, transfer learning techniques could be used to make this step more efficient by leveraging pre-existing knowledge from similar physics problems.

- Automated tools to inform patient-specific models

  The generated library is very useful for handling large datasets of segmented cases, but it currently lacks an option for including raw data that is not annotated. Therefore, future work should focus on integrating our library with other automatic or semi-automatic segmentation tools.

6.3 Contributions

As a result of the research work carried out in this dissertation, several journal publications have been published and others are under review or in preparation. Additionally, this work has also resulted in three podium presentations at international congresses and another one at a local conference:

6.3.1 Publications in peer-reviewed journals

1. **Sainz-DeMena D.**, Ye W., Pérez M. A., García-Aznar J. M. *A finite element based optimization algorithm to include diffusion into the analysis of DCE-MRI.* Engineering with Computers 38, 3849–3865 (2022) https://doi.org/10.1007/s00366-022-01667-w

2. **Sainz-DeMena D.**, García-Aznar J. M., Pérez M. A., Borau C. *Im2mesh: A Python Library to Reconstruct 3D Meshes from Scattered Data and 2D Segmentations, Application to Patient-Specific Neuroblastoma Tumour Image Sequences.* Applied Sciences 12 (2022) https://doi.org/10.3390/app122211557

Submitted:

1. **Sainz-DeMena D.**, Pérez, M. A., García-Aznar J. M. *Exploring the potential of Physics-Informed Neural Networks to extract vascularization data from DCE-MRI in the presence of diffusion*

   Submitted to *Medical Engineering and Physics*

2. Juma V., **Sainz-DeMena D.**, Sánchez, M. T., García-Aznar J. M. *Effects of tumour heterogeneous properties on modelling the transport of radiative particles*

   Submitted to *International Journal of Numerical Methods in Biomedical Engineering*

3. Borau C., Wertheim, K. Y., Hervás-Raluy S., **Sainz-DeMena D.**, Walker D., Chisholm R., Richmond P., Varella V., Viceconti M., Montero A., Gregori-Puigjané E., Mestres J., Kasztelnik M., García-Aznar J. M. *A multiscale orchestrated computational framework to reveal emergent phenomena in neuroblastoma*

   Submitted to *Computer Methods and Programs in Biomedicine*

In preparation:

1. Hervás-Raluy S., **Sainz-DeMena D.**, Gómez-Benito, M. J., García-Aznar J. M. *Image-based biomarkers for engineering neuroblastoma patient specific computational models*

6.3.2 Congress and conference contributions

The following communications have been presented during the development of this dissertation:

1. 17th International Symposium on Computer Methods in Biomechanics and Biomedical Engineering. *A continuum approach for the diffusion compensated ETM model and its application on Neuroblastoma clinical data.* Bonn (Germany), hybrid (in the context of the COVID-19 pandemic), September 7-9, 2021.

2. 8th European Congress on Computational Methods in Applied Sciences and Engineering. *A Finite Element method to incorporate the effects of diffusion to the Extended Tofts Model.* Oslo (Norway), June 5-9, 2022.

3. 11th Conference of Young Researchers of the Engineering Research Institute of Aragon. *A Finite Element Based Optimization Algorithm to Include Diffusion into the Analysis of DCE-MRI.* Zaragoza (Spain), June 16, 2022.

4. 7th Conference on Virtual Physiological Human (VPH). *Patient-specific models in tumor growth: integrating organoids and image-based biomarkers.* Porto (Portugal), September 6-9, 2022.

5. 17th U. S. National Congress on Computational Mechanics. *Physics-Informed Neural Networks for incorporating contrast agent diffusion in the Extended Tofts Model.* Albuquerque, NM (USA), July 23-27, 2023.

6.3.3 Teaching

The author has co-supervised one Bachelor's thesis in Mechanical Engineering, entitled *Computational simulation of solid tumor vascularization of solid tumors using the Finite Element Method* by Sergio Ibor Castel.

The author has also taught practical courses in Mechanical Engineering Bachelor (Continuum Mechanics) and Chemical Engineering Bachelor (Strength of Materials).

6.4 Funding

The author would like to acknowledge the Spanish Ministry of Science, Education and Universities (FPU18/04541).

Chapter 7

Conclusiones

7.1 Conclusiones finales

En este capítulo se presentan las principales conclusiones extraídas de esta tesis doctoral y las futuras líneas de investigación que se abren a partir del trabajo realizado.

El principal objetivo de esta tesis ha sido, por un lado, el desarrollo de nuevos modelos y métodos para mejorar la precisión de los datos de vascularización obtenidos a partir de las secuencias DCE-MRI y, por otro, la creación de una herramienta que automatice la creación de modelos de paciente-específico a partir de datos de imagen. Para el primer objetivo, se ha planteado la formulación de un nuevo modelo farmacocinético en el que se incluye el proceso de difusión de agente de contraste. Para resolver el problema inverso que surge al tratar de ajustar este modelo a los datos obtenidos de las secuencias DCE-MRI, se han empleado dos enfoques distintos. El primero de ellos se ha basado en el método del descenso del gradiente, usando el método de los elementos finitos para obtener dicho gradiente de una forma mucho más eficiente que las alternativas numéricas, como el método de las diferencias finitas. En el segundo enfoque se ha explorado el potencial de los métodos de aprendizaje profundo para resolver este problema inverso. En concreto, se han empleado las redes neuronales informadas por la física (PINNs), obteniendo unos resultados prometedores en los casos estudiados. Por otro lado, se ha creado una biblioteca en *Python* para simplificar y automatizar la creación de modelos 3D de elementos finitos y la integración de datos de imagen en estos modelos.

Las principales conclusiones se han agrupado por capítulos:

- **Capítulo 2**: El modelo extendido de Tofts incorporando la difusión
  - A diferencia de la mayoría de los modelos anteriores, esta nueva formulación no asume que el agente de contraste se difunda libremente a través de la cara del elemento. En este nuevo modelo consideramos que, dependiendo del nivel de celularidad del elemento, la superficie libre para la difusión del contraste puede ser una fracción de la cara del elemento.
  - Al definir el término difusivo en función del concepto de difusividad efectiva, se incluye la difusividad como una incógnita adicional y que puede tomar distintos valores en cada uno de los elementos. A través de este enfoque se puede definir el coeficiente de difusión en función de otras variables del modelo, evitando así incrementar el número total de incógnitas del modelo.
- **Capítulo 3**: El algortimo de optimización basado en el método de los elementos finitos
  - La resonancia magnética dinámica con contraste es una técnica de imagen médica muy útil para evaluar el estado de vascularización de los tejidos, especialmente en oncología. Sin embargo, debido a la complejidad de los modelos farmacocinéticos, es complicado obtener de forma precisa los parámetros que describen la vascularización.
  - Las simulaciones llevadas a cabo confirman las limitaciones de los modelos estándar y extendido de Tofts al estimar los parámetros K^{Trans} y v_e con precisión cuando el agente de contraste llega al tejido a través de fenómenos de trasnporte pasivo, como la difusión.
  - El modelo D-ETM propuesto ha demostrado una mayor precisión al ajustar los parámetros K^{Trans} y v_e. Este modelo ha capturado con exactitud la heterogeneidad en la distribución de estos parámetros, obteniendo menores errores que el modelo extendido de Tofts.
  - En comparación con estudios previos [40], en los que usaron algoritmos estocásticos para resolver el problema inverso, el método propuesto en este capítulo es notablemente más rápido, evitando así ciertas simplificaciones que limitan el rango de aplicación del modelo.
  - A pesar de los buenos resultados obtenidos, el modelo D-ETM ajusta con menor precisión el parámetro v_e en comparación con el modelo

DP [40]. Esto se nota especialmente en las zonas necróticas, donde apenas hay vascularización. Indirectamente, esto implica que el parámetro v_e apenas influye en la solución, lo que hace que el valor de su gradiente sea muy bajo y no se pueda ajustar con precisión.

- **Capítulo 4**: Explorando el potencial de las PINNs
  - El enfoque basado en las PINNs ha superado al algortimo presentado en el capítulo anterior en cuanto a precisión en los parámetros ajustados. Además, este nuevo método ha demostrado una mayor robustez ante la presencia de ruido o la falta de datos.
  - Este nuevo enfoque ha ajustado con precisión el parámetro v_e a lo largo de las zonas necróticas, superando las limitaciones tanto de los métodos basados en el gradiente como de los métodos estocásticos [40].
  - La formulación original de las PINNs propuesta por Raissi *et al.* [87] no era suficiente para el ajuste del D-ETM. Ha sido necesario incluir otras características, como el uso de pesos ponderados y el refinado adaptativo basado en los residuos (RAR, por sus siglas en inglés), para poder obtener los parámetros con precisión.
- **Capítulo 5**: Una biblioteca de *Python* para reconstruir mallas 3D a partir de datos clínicos
  - Los modelos de paciente-específico están ganando cada vez más importancia en el estudio de distintas patologías y necesitan de métodos sencillos y eficaces que generen los datos de entrada necesarios para los mismos.
  - *im2mesh* es una solución que automatiza el proceso de generación de estos datos de entrada a partir de imágenes segmentadas y crea los archivos necesarios sin la intervención del usuario, lo que la hace ideal para su integración en entornos de trabajo más complejos.
  - Los enfoques del tipo "todo en uno" que pueden conectar los distintos elementos de un entorno de trabajo serán necesarios para las futuras plataformas que se integren en la práctica clínica. Actualmente *im2mesh* está integrada en la plataforma web del proyecto PRIMAGE, aunque también está disponible como un paquete independiente para ser descargado por cualquier usuario que la quiera usar en su entorno de trabajo.

7.2 Líneas futuras

Los resultados presentados en esta tesis ponen de relieve la creciente importancia de los modelos de paciente-específico y la necesidad de nuevos métodos que obtengan datos precisos de las imágenes médicas y los incluyan de forma sencilla en los modelos.

- Incorporar la difusión de agente de contraste en el análisis de las secuencias DCE-MRI

  Respecto a la formulación del D-ETM, es necesario revisar la definición del término difusivo para tratar de aumentar la influencia de la variable v_e en el mismo. De este modo, el peso del gradiente de esta variable en las zonas necróticas aumentará, facilitando la convergencia de los algortimos de optimización. Además, para poder ampliar el rango de aplicación del modelo y aumentar la precisión del mismo, futuros trabajos deberían incorporar el término convectivo en la formulación. Para tratar de reducir la complejidad del modelo al añadir el término, sería posible comenzar fijando el valor de la velocidad intersticial del fluido en base a valores tomados de la literatura, evitando así una incógnita adicional.

  Existen métodos alternativos para calcular el gradiente que pueden minimizar el coste computacional asociado a este cálculo. La mejor alternativa es el método del estado adjunto, ya que el coste computacional del método no depende del número de variables del problema.

  Como alternativa a los métodos basados en el descenso del gradiente, se ha propuesto un enfoque basado en las PINNs. A pesar de los buenos resultados obtenidos en los casos 1D simulados, es necesario seguir trabajando en esta línea para optimizar el método y poder escalarlo a casos 2D. En primer lugar, es necesario hacer una calibración de los hiperparámetros, bien a través de algoritmos de búsqueda, algoritmos evolutivos u optimización Bayesiana. Es también necesario reducir el coste computacional del entrenamiento de la red. Para ello se pueden emplear técnicas de transferencia de aprendizaje, que aprovechan el conocimiento existente de problemas físicos similares.

- Métodos para automatizar la creación de modelos de paciente-específico

  Aunque la bilioteca desarrollada ha demostrado ser sumamente útil para trabajar con grandes conjuntos de casos ya segmentados, carece de funciones que permitan incluir casos sin segmentar. Por ello, el siguiente paso

debería ir en la dirección de integrar esta biblioteca con otras herramientas de segmentación automática o semi-automática.

7.3 Contribuciones

Como resultado del trabajo realizado en esta tesis doctoral, se han publicado varios trabajos en revistas y otros están en revisión o en preparación. Además, este trabajo también ha dado lugar a tres presentaciones orales en congresos internacionales y otra en una conferencia local:

7.3.1 Publicaciones en revistas

1. **Sainz-DeMena D.**, Ye W., Pérez M. A., García-Aznar J. M. *A finite element based optimization algorithm to include diffusion into the analysis of DCE-MRI.* Engineering with Computers 38, 3849–3865 (2022) https://doi.org/10.1007/s00366-022-01667-w

2. **Sainz-DeMena D.**, García-Aznar J. M., Pérez M. A., Borau C. *Im2mesh: A Python Library to Reconstruct 3D Meshes from Scattered Data and 2D Segmentations, Application to Patient-Specific Neuroblastoma Tumour Image Sequences.* Applied Sciences 12 (2022) https://doi.org/10.3390/app122211557

Enviadas:

1. **Sainz-DeMena D.**, Pérez, M. A., García-Aznar J. M. *Exploring the potential of Physics-Informed Neural Networks to extract vascularization data from DCE-MRI in the presence of diffusion*

   Enviada a *Medical Engineering and Physics*

2. Juma V., **Sainz-DeMena D.**, Sánchez, M. T., García-Aznar J. M. *Effects of tumour heterogeneous properties on modelling the transport of radiative particles*

   Enviada a *International Journal of Numerical Methods in Biomedical Engineering*

3. Borau C., Wertheim, K. Y., Hervás-Raluy S., **Sainz-DeMena D.**, Walker D., Chisholm R., Richmond P., Varella V., Viceconti M., Montero A., Gregori-Puigjané E., Mestres J., Kasztelnik M., García-Aznar J. M. *A multiscale or-*

chestrated computational framework to reveal emergent phenomena in neuroblastoma

Enviada a *Computer Methods and Programs in Biomedicine*

En preparación:

1. Hervás-Raluy S., **Sainz-DeMena D.**, Gomez-Benito, M. J., García-Aznar J. M. *Image-based biomarkers for engineering neuroblastoma patient specific computational models*

7.3.2 Comunicaciones en congresos y conferencias

Durante el desarrollo de esta tesis se han presentado las siguientes comunicaciones:

1. 17th International Symposium on Computer Methods in Biomechanics and Biomedical Engineering. *A continuum approach for the diffusion compensated ETM model and its application on Neuroblastoma clinical data.* Bonn (Alemania), híbrido (en el contexto de la pandemia de COVID-19), Septiembre, 2021.

2. 8th European Congress on Computational Methods in Applied Sciences and Engineering. *A Finite Element method to incorporate the effects of diffusion to the Extended Tofts Model.* Oslo (Noruega), Junio, 2022.

3. 11ª Jornada de Jóvenes Investigadores del Instituto de Investigación en Ingeniería de Aragón. *A Finite Element Based Optimization Algorithm to Include Diffusion into the Analysis of DCE-MRI.* Zaragoza (España), Junio, 2022.

4. 7th Conference on Virtual Physiological Human (VPH). *Patient-specific models in tumor growth: integrating organoids and image-based biomarkers.* Porto (Portugal), Septiembre, 2022.

5. 17th U. S. National Congress on Computational Mechanics. *Physics-Informed Neural Networks for incorporating contrast agent diffusion in the Extended Tofts Model.* Albuquerque, Nuevo México (EEUU), Julio, 2023.

7.3.3 Docencia

El autor ha codirigido un Trabajo de Final de Grado en Ingeniería Mecánica, titulado *Simulación computacional de la vascularización de tumores sólidos utilizando el Método de los Elementos Finitos*, por Sergio Ibor Castel.

Además, el autor ha impartido clases prácticas en el Grado en Ingeniería Mecánica (Mecánica de sólidos deformables) y en el Grado en Ingeniería Química (Resistencia de materiales).

7.4 Financiación

El autor de esta tesis agradece al Ministerio de Ciencia, Educación y Universidades la financiación recibida a través del programa FPU (FPU18/04541).

Appendices

Appendix A

A.1 Comparison between the semi-analytical and numerical methods to compute the Jacobian matrix

A small model (36 nodes and 120 timepoints) was created to compute its Jacobian matrix using the numerical approach based on the finite differences method, obtaining matrix $\boldsymbol{J_N}$, and the semi-analytical method proposed in section 3.3 (equations 3.10-3.12), obtaining matrix $\boldsymbol{J_A}$. The numerical matrix $\boldsymbol{J_N}$ was considered as ground truth.

Given that most of values in the Jacobian matrix are zero or close to zero, we define a new error metric, ARD_{max}. This variable is defined as the quotient of the absolute difference between the Jacobian retrieved by each method and the maximum value of the numerical Jacobian. To improve the accuracy of the metric, we evaluate it for every nodal concentration for each nodal variable and each timepoint (equation A.1). E.g., for K^{Trans}, we compute this metric for every nodal concentration for a certain timepoint (t_i) for a certain nodal variable ($K_j{}^{Trans}$):

$$ARD_{max}{}_j^{t_i} = \frac{\|{J_A}_j^{t_i} - {J_N}_j^{t_i}\|}{Max({J_N}_j^{t_i})} \tag{A.1}$$

Figure A.1 shows the error distribution of the semi-analytical method with respect to the numerical one. The K^{Trans} and v_p Jacobian matrices show below 0.5% of error and 97% of the elements in the v_e matrix show an error below 2%, what proves the accuracy of the semi-analytical method.

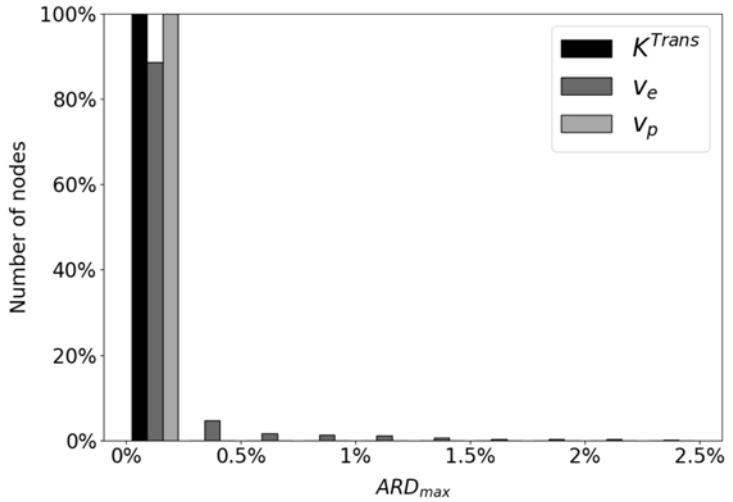

Figure A.1: Histogram of the metric ARD_{max} measured in the small model proposed. For K^{Trans} and v_p, the error is below 0.5%, while around 97% of the values for v_e are below 2%.

A.2 Benchmark problem: influence of the axisymmetric geometry

To further investigate the impact of the axisymmetric geometry on the convergence issues discussed in section 3.4.1, an additional simulation was conducted. The objective was to examine how eliminating the symmetry in the geometry affected the convergence behavior. In this experiment, the geometry was adjusted to remove the axisymmetric feature, while maintaining the consistent distributions of parameters. The specific parameter values used were as follows: K^{Trans} was set to 0.2 min^{-1} in the rim and 0.05 in the core; a constant value of v_e was uniformly applied as 0.5 throughout the entire model; and v_p was assigned a value of 0.05 in the rim and 0.005 in the core.

The initial seed for this simulation consisted of a random distribution of values, which resembled the one described in section 3.4.1. For K^{Trans}, the initial values ranged between 0.4 min^{-1} and 0. Similarly, for v_e, the values ranged between 0.2 and 0.8. Lastly, for v_p, the initial values ranged from 0 to 0.1. Ten different simulations were computed to evaluate the influence of the initial seed on the results. All of them converged to very similar values, validating the results

obtained (Table A.1).

Table A.1: Comparison of error metrics between the D-ETM and the ETM for the non symmetric geometry of the benchmark problem. The absolute error corresponds to the mean value of the model. K^{Trans} absolute error is measured in min^{-1}.

	D-ETM		ETM	
	Absolute error	Fraction of nodes error < threshold	Absolute error	Fraction of nodes error < threshold
K^{Trans}	1.14E-02	64.58%	2.69E-02	45.03%
v_e	1.02E-01	56.14%	1.73E+06	71.07%
v_p	8.45E-04	78.79%	5.56E-03	77.71%

Despite the fact that the D-ETM exhibits higher error metrics in Table A.1 compared to those in Table 3.1, it still demonstrates superior performance over the ETM, particularly in relation to the K^{Trans} map. On the contrary, the ETM shows lower error values in this particular scenario.

This observation can be attributed to the homogeneity observed in the parameter maps depicted in Figure A.2. In the benchmark problem, represented by Figure 3.3, the reference maps exhibited heterogeneity, resulting in concentration gradients between neighboring elements within the vascularized region. These concentration gradients induced diffusion fluxes, which in turn affected the parameters estimated by the ETM, as elaborated in section 3.4.1. However, in the current case, the homogeneity in the parameter distributions eliminates the influence of diffusion in the vascularized rim, thereby benefiting the ETM.

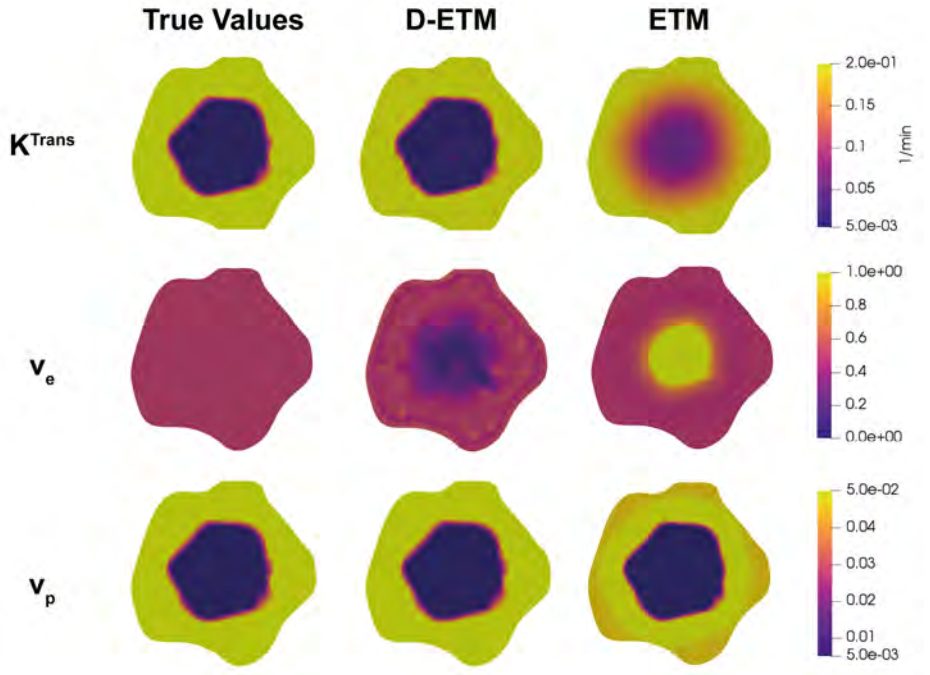

Figure A.2: Third simulation of the benchmark problem, modifying the axisymmetric geometry. Comparison between the reference values and the parameters returned by the D-ETM and the ETM. Although the maps retrieved by the D-ETM are not as accurate as the ones obtained in section 3.4.1, it outperforms the ETM, especially on the sharp contours of K^{Trans} and v_p maps.

Bibliography

[1] M. N. Kamel Boulos and P. Zhang. "Digital Twins: From Personalised Medicine to Precision Public Health". In: *Journal of Personalized Medicine 2021, Vol. 11, Page 745* 11.8 (July 2021), p. 745 (cit. on p. 1).

[2] J. G. Chase et al. "Next-generation, personalised, model-based critical care medicine: a state-of-the art review of in silico virtual patient models, methods, and cohorts, and how to validation them". In: *BioMedical Engineering OnLine* 17.1 (Feb. 2018), pp. 1–29 (cit. on p. 1).

[3] H. K. Brittain, R. Scott, and E. Thomas. "The rise of the genome and personalised medicine". In: *Clinical Medicine* 17.6 (Dec. 2017), p. 545 (cit. on p. 1).

[4] T. O. Yau. "Precision treatment in colorectal cancer: Now and the future". In: *JGH Open: An Open Access Journal of Gastroenterology and Hepatology* 3.5 (Oct. 2019), p. 361 (cit. on p. 1).

[5] K. W. Lee, A. M. Bode, and Z. Dong. "Molecular targets of phytochemicals for cancer prevention". In: *Nature Reviews Cancer* 11.3 (Feb. 2011), pp. 211–218 (cit. on p. 1).

[6] B. Shaker, S. Ahmad, J. Lee, C. Jung, and D. Na. "In silico methods and tools for drug discovery". In: *Computers in Biology and Medicine* 137 (Oct. 2021), p. 104851 (cit. on p. 2).

[7] M. Viceconti, F. Pappalardo, B. Rodriguez, M. Horner, J. Bischoff, and F. Musuamba Tshinanu. "In silico trials: Verification, validation and uncertainty quantification of predictive models used in the regulatory evaluation of biomedical products". In: *Methods* 185 (Jan. 2021), pp. 120–127 (cit. on p. 2).

[8] X. Chen, K. Men, Y. Li, J. Yi, and J. Dai. "A feasibility study on an automated method to generate patient-specific dose distributions for radiotherapy using deep learning". In: *Medical Physics* 46.1 (Jan. 2019), pp. 56–64 (cit. on p. 2).

[9] G. Valdes, C. B. Simone, J. Chen, A. Lin, S. S. Yom, A. J. Pattison, C. M. Carpenter, and T. D. Solberg. "Clinical decision support of radiotherapy treatment planning: A data-driven machine learning strategy for patient-

specific dosimetric decision making". In: *Radiotherapy and Oncology* 125.3 (Dec. 2017), pp. 392–397 (cit. on p. 2).

[10] K. C. Wong. "3D-printed patient-specific applications in orthopedics". In: *Orthopedic Research and Reviews* 8 (2016), p. 57 (cit. on p. 2).

[11] O. Abdelaal, S. Darwish, H. El-Hofy, and Y. Saito. "Patient-specific design process and evaluation of a hip prosthesis femoral stem". In: *The International Journal of Artificial Organs* 42.6 (Dec. 2018), pp. 271–290 (cit. on p. 2).

[12] World Health Organization. *Cancer*. 2022 (cit. on pp. 2, 64).

[13] P. M. Altrock, L. L. Liu, and F. Michor. "The mathematics of cancer: integrating quantitative models". In: *Nature Reviews Cancer* 15.12 (Nov. 2015), pp. 730–745 (cit. on p. 2).

[14] C. Borau, K. Wertheim, S. Hervas-Raluy, D. Sainz-DeMena, D. Walker, R. Chisholm, P. Richmond, V. Varella, M. Viceconti, A. Montero, et al. *A Multiscale Orchestrated Computational Framework to Reveal Emergent Phenomena in Neuroblastoma* (cit. on pp. 2, 11).

[15] M. H. Zangooei, R. Margolis, and K. Hoyt. "Multiscale computational modeling of cancer growth using features derived from microCT images". In: *Scientific Reports* 11.1 (Sept. 2021), pp. 1–17 (cit. on p. 2).

[16] R. E. Coleman, J. Brown, and I. Holen. "Bone Metastases". In: *Abeloff's Clinical Oncology* (Jan. 2020), 809–830.e3 (cit. on p. 2).

[17] M. D. Farwell, D. A. Pryma, and D. A. Mankoff. "PET/CT imaging in cancer: Current applications and future directions". In: *Cancer* 120.22 (Nov. 2014), pp. 3433–3445 (cit. on p. 2).

[18] A. Wadhwa, A. Bhardwaj, and V. Singh Verma. "A review on brain tumor segmentation of MRI images". In: *Magnetic Resonance Imaging* 61 (Sept. 2019), pp. 247–259 (cit. on p. 3).

[19] J. Chapiro, M. Lin, R. Duran, R. E. Schernthaner, and J. F. Geschwind. "Assessing tumor response after loco-regional liver cancer therapies: the role of 3D MRI". In: *Expert Review of Anticancer Therapy* 15.2 (Feb. 2015), pp. 199–205 (cit. on p. 3).

[20] G. Murphy, M. Haider, S. Ghai, and B. Sreeharsha. "The expanding role of MRI in prostate cancer". In: *AJR. American journal of roentgenology* 201.6 (Dec. 2013), pp. 1229–1238 (cit. on p. 3).

[21] S. Ghai and M. A. Haider. “Multiparametric-MRI in diagnosis of prostate cancer”. In: *Indian Journal of Urology : IJU : Journal of the Urological Society of India* 31.3 (July 2015), p. 194 (cit. on p. 3).

[22] N. Schieda, C. S. Lim, F. Zabihollahy, J. Abreu-Gomez, S. Krishna, S. Woo, G. Melkus, E. Ukwatta, and B. Turkbey. “Quantitative Prostate MRI”. In: *Journal of Magnetic Resonance Imaging* 53.6 (June 2021), pp. 1632–1645 (cit. on p. 3).

[23] Y. Gordon, S. Partovi, M. Müller-Eschner, E. Amarteifio, T. Bäuerle, M.-A. Weber, H.-U. Kauczor, and F. Rengier. “Dynamic contrast-enhanced magnetic resonance imaging: fundamentals and application to the evaluation of the peripheral perfusion.” In: *Cardiovascular diagnosis and therapy* 4.2 (2014), pp. 147–14764 (cit. on p. 4).

[24] G. Brix, W. Schreiber, U. Hoffmann, F. Gückel, H. Hawighorst, and M. V. Knopp. “Methodological approaches to quantitative evaluation of microcirculation in tissues with dynamic magnetic resonance tomography”. In: *Der Radiologe* 37.6 (1997), pp. 470–480 (cit. on p. 4).

[25] G. Brix, F. Kiessling, R. Lucht, S. Darai, K. Wasser, S. Delorme, and J. Griebel. “Microcirculation and microvasculature in breast tumors: Pharmacokinetic analysis of dynamic MR image series”. In: *Magnetic Resonance in Medicine* 52.2 (Aug. 2004), pp. 420–429 (cit. on p. 4).

[26] T. E. Yankeelov and J. C. Gore. “Dynamic Contrast Enhanced Magnetic Resonance Imaging in Oncology: Theory, Data Acquisition, Analysis, and Examples”. In: *Current medical imaging reviews* 3.2 (May 2009), p. 91 (cit. on p. 5).

[27] T. Fritz-Hansen, E. Rostrup, H. B. Larsson, L. Søndergaard, P. Ring, and O. Henriksen. “Measurement of the arterial concentration of Gd-DTPA using MRI: a step toward quantitative perfusion imaging”. In: *Magnetic resonance in medicine* 36.2 (1996), pp. 225–231 (cit. on p. 5).

[28] D. J. McIntyre, C. Ludwig, A. Pasan, and J. R. Griffiths. “A method for interleaved acquisition of a vascular input function for dynamic contrast-enhanced MRI in experimental rat tumours”. In: *NMR in Biomedicine* 17.3 (May 2004), pp. 132–143 (cit. on p. 5).

[29] R. Zhou, S. Pickup, T. E. Yankeelov, C. S. Springer, and J. D. Glickson. "Simultaneous measurement of arterial input function and tumor pharmacokinetics in mice by dynamic contrast enhanced imaging: Effects of transcytolemmal water exchange". In: *Magnetic Resonance in Medicine* 52.2 (Aug. 2004), pp. 248–257 (cit. on p. 5).

[30] D. A. Kovar, M. Lewis, and G. S. Karczmar. "A new method for imaging perfusion and contrast extraction fraction: Input functions derived from reference tissues". In: *Journal of Magnetic Resonance Imaging* 8.5 (Sept. 1998), pp. 1126–1134 (cit. on p. 5).

[31] T. E. Yankeelov, J. J. Luci, M. Lepage, R. Li, L. Debusk, P. C. Lin, R. R. Price, and J. C. Gore. "Quantitative pharmacokinetic analysis of DCE-MRI data without an arterial input function: a reference region model". In: *Magnetic Resonance Imaging* 23.4 (May 2005), pp. 519–529 (cit. on p. 5).

[32] R. B. Thompson, R. J. Aviles, A. Z. Faranesh, V. K. Raman, V. Wright, R. S. Balaban, E. R. McVeigh, and R. J. Lederman. "Measurement of skeletal muscle perfusion during postischemic reactive hyperemia using contrast-enhanced MRI with a step-input function". In: *Magnetic resonance in medicine* 54.2 (2005), pp. 289–298 (cit. on p. 5).

[33] M. Beaumont, M. G. DuVal, Y. Loai, W. A. Farhat, G. K. Sándor, and H. L. M. Cheng. "Monitoring angiogenesis in soft-tissue engineered constructs for calvarium bone regeneration: an in vivo longitudinal DCE-MRI study". In: *NMR in Biomedicine* 23.1 (Jan. 2010), pp. 48–55 (cit. on p. 5).

[34] P. S. Tofts and A. G. Kermode. "Measurement of the blood-brain barrier permeability and leakage space using dynamic MR imaging. 1. Fundamental concepts". In: *Magnetic Resonance in Medicine* 17.2 (1991), pp. 357–367 (cit. on pp. 6, 16, 20, 27).

[35] "Estimating Kinetic Parameters From Dynamic Contrast-Enhanced T 1-Weighted MRI of a Diffusable Tracer: Standardized Quantities and Symbols". In: 10 (1999), pp. 223–232 (cit. on pp. 6, 16, 19, 27, 53).

[36] S. P. Sourbron and D. L. Buckley. "On the scope and interpretation of the Tofts models for DCE-MRI". In: *Magnetic Resonance in Medicine* 66.3 (2011), pp. 735–745 (cit. on p. 6).

[37] M. J. Gordon, K. C. Chu, A. Margaritis, A. J. Martin, C. Ross Ethier, and B. K. Rutt. "Measurement of Gd-DTPA Diffusion Through PVA Hydrogel Using a Novel Magnetic Resonance Imaging Method". In: *Biotechnology and Bioengineering* 65 (1999), pp. 459–467 (cit. on pp. 7, 32, 52).

[38] R. T. Woodall, S. L. Barnes, D. A. Hormuth, et al. "The effects of intra-voxel contrast agent diffusion on the analysis of DCE-MRI data in realistic tissue domains". In: *Magnetic Resonance in Medicine* 80.1 (2018), pp. 330–340 (cit. on pp. 7, 32, 44).

[39] S. L. Barnes, C. C. Quarles, and T. E. Yankeelov. "Modeling the effect of intra-voxel diffusion of contrast agent on the quantitative analysis of dynamic contrast enhanced magnetic resonance imaging". In: *Program in Chemical and Physical Biology* 7.10 (2014), p. 108726 (cit. on p. 7).

[40] M. Pellerin, T. E. Yankeelov, and M. Lepage. "Incorporating contrast agent diffusion into the analysis of DCE-MRI data". In: *Magnetic Resonance in Medicine* 58.6 (2007), pp. 1124–1134 (cit. on pp. 8, 16, 20, 22, 24, 27, 30, 32, 35, 36, 40, 42, 43, 46, 52–54, 56, 59, 82, 90, 91).

[41] J. U. Fluckiger, M. E. Loveless, S. L. Barnes, M. Lepage, and T. E. Yankeelov. "A diffusion-compensated model for the analysis of DCE-MRI data: theory, simulations, and experimental results". In: *Physics in Medicine and Biology* 58.6 (2013), pp. 1983–1998 (cit. on pp. 8, 16, 20, 22, 27, 31–33, 35, 42, 43, 46, 52, 54, 59).

[42] G. Jia, C. O'Dell, J. T. Heverhagen, et al. "Colorectal liver metastases: Contrast agent diffusion coefficient for quantification of contrast enhancement heterogeneity at MR imaging". In: *Radiology* 248.3 (2008), pp. 901–909 (cit. on pp. 8, 16, 42, 59).

[43] T. S. Koh, S. Hartono, C. H. Thng, T. K. H. Lim, L. Martarello, and Q. S. Ng. "In vivo measurement of gadolinium diffusivity by dynamic contrast-enhanced MRI: A preclinical study of human xenografts". In: *Magnetic Resonance in Medicine* 69.1 (Jan. 2013), pp. 269–276 (cit. on pp. 8, 16, 22, 32, 42, 52, 59).

[44] C. G. Cantrell, P. Vakil, Y. Jeong, S. A. Ansari, and T. J. Carroll. "Diffusion-compensated tofts model suggests contrast leakage through aneurysm wall". In: *Magnetic Resonance in Medicine* 78.6 (2017), pp. 2388–2398 (cit. on pp. 8, 16, 20, 22, 42, 46, 59).

[45] S. Stapleton, M. Milosevic, C. Allen, J. Zheng, M. Dunne, I. Yeung, and D. A. Jaffray. "A Mathematical Model of the Enhanced Permeability and Retention Effect for Liposome Transport in Solid Tumors". In: *PLOS ONE* 8.12 (Dec. 2013), e81157 (cit. on p. 8).

[46] S. Sourbron. "A tracer-kinetic field theory for medical imaging". In: *IEEE Transactions on Medical Imaging* 33.4 (2014), pp. 935–946 (cit. on pp. 8, 16, 42, 59).

[47] N. Sinno, E. Taylor, M. Milosevic, D. A. Jaffray, and C. Coolens. "Incorporating cross-voxel exchange into the analysis of dynamic contrast-enhanced imaging data: theory, simulations and experimental results". In: *Physics in Medicine and Biology* 66.20 (Oct. 2021), p. 205018 (cit. on pp. 9, 16, 20, 22, 42, 46, 59).

[48] J. A. Vossen, M. Buijs, J.-F. H. Geschwind, et al. "Diffusion-Weighted and Gd-EOB-DTPA–Contrast-Enhanced Magnetic Resonance Imaging for Characterization of Tumor Necrosis in an Animal Model". In: *Journal of Computer Assisted Tomography* 33.4 (2009), pp. 626–630 (cit. on pp. 11, 31, 32, 38).

[49] S. Hervas-Raluy, B. Wirthl, P. E. Guerrero, G. Robalo Rei, J. Nitzler, E. Coronado, J. Font de Mora Sainz, B. A. Schrefler, M. J. Gomez-Benito, J. M. Garcia-Aznar, and W. A. Wall. "Tumour growth: An approach to calibrate parameters of a multiphase porous media model based on in vitro observations of Neuroblastoma spheroid growth in a hydrogel microenvironment". In: *Computers in Biology and Medicine* 159 (June 2023), p. 106895 (cit. on pp. 11, 64).

[50] B. de Melo Quintela, S. Hervas-Raluy, J. M. Garcia-Aznar, D. Walker, K. Y. Wertheim, and M. Viceconti. "A theoretical analysis of the scale separation in a model to predict solid tumour growth". In: *Journal of Theoretical Biology* 547 (Aug. 2022), p. 111173 (cit. on p. 11).

[51] M. Italia, K. Y. Wertheim, S. Taschner-Mandl, D. Walker, and F. Dercole. "Mathematical Model of Clonal Evolution Proposes a Personalised Multi-Modal Therapy for High-Risk Neuroblastoma". In: *Cancers* 15.7 (Apr. 2023), p. 1986 (cit. on p. 11).

[52] D. Sainz-DeMena, W. Ye, M. Á. Pérez, and J. M. García-Aznar. "A finite element based optimization algorithm to include diffusion into the analysis

of DCE-MRI". In: *Engineering with Computers* 38.5 (Oct. 2022), pp. 3849–3865 (cit. on pp. 15, 23, 46, 52–54, 56, 59).

[53] T. Barrett, M. Brechbiel, M. Bernardo, and P. L. Choyke. "MRI of tumor angiogenesis". In: *Journal of Magnetic Resonance Imaging* 26.2 (2007), pp. 235–249 (cit. on pp. 16, 42, 59).

[54] K. Zormpas-Petridis, N. P. Jerome, et al. "MRI imaging of the hemodynamic vasculature of neuroblastoma predicts response to antiangiogenic treatment". In: *Cancer Research* 79.11 (June 2019), pp. 2978–2991 (cit. on pp. 16, 42, 59).

[55] J. P. B. O'Connor, E. O. Aboagye, J. E. Adams, et al. "Imaging biomarker roadmap for cancer studies". In: *Nature Publishing Group* 14 (2017), pp. 169–186 (cit. on pp. 16, 42, 59).

[56] C. A. Cuenod and D. Balvay. "Perfusion and vascular permeability: Basic concepts and measurement in DCE-CT and DCE-MRI". In: *Diagnostic and Interventional Imaging* 94.12 (Dec. 2013), pp. 1187–1204 (cit. on p. 16).

[57] N. Wake, H. Chandarana, H. Rusinek, et al. "Accuracy and precision of quantitative DCE-MRI parameters: How should one estimate contrast concentration?" In: *Magnetic resonance imaging* 52 (Oct. 2018), pp. 16–23 (cit. on p. 16).

[58] F. Khalifa, A. Soliman, A. El-Baz, et al. "Models and methods for analyzing DCE-MRI: A review". In: *Medical Physics* 41.12 (Nov. 2014), p. 124301 (cit. on p. 16).

[59] S. P. Sourbron and D. L. Buckley. "On the scope and interpretation of the Tofts models for DCE-MRI". In: *Magnetic Resonance in Medicine* 66.3 (Sept. 2011), pp. 735–745 (cit. on p. 16).

[60] C. Nicholson and J. M. Phillips. "Ion diffusion modified by tortuosity and volume fraction in the extracellular microenvironment of the rat cerebellum." In: *The Journal of Physiology* 321.1 (Dec. 1981), pp. 225–257 (cit. on p. 17).

[61] C. Nicholson and M. E. Rice. "The Migration of Substances in the Neuronal Microenvironment". In: *Annals of the New York Academy of Sciences* 481 (1986), pp. 55–68 (cit. on p. 17).

[62] C. Nicholson. “Diffusion and related transport mechanisms in brain tissue”. In: *Reports on Progress in Physics* 64.7 (2001), pp. 815–884 (cit. on pp. 17, 19, 20, 22).

[63] E. Syková and C. Nicholson. “Diffusion in Brain Extracellular Space”. In: *Physiological reviews* 88.4 (Oct. 2008), pp. 1277–1340 (cit. on p. 17).

[64] C. Nicholson and E. Syková. “Extracellular space structure revealed by diffusion analysis”. In: *Trends in Neurosciences* 21.5 (May 1998), pp. 207–215 (cit. on p. 17).

[65] L. Tao and C. Nicholson. “Maximum geometrical hindrance to diffusion in brain extracellular space surrounding uniformly spaced convex cells”. In: *Journal of Theoretical Biology* 229.1 (July 2004), pp. 59–68 (cit. on pp. 17, 19, 20).

[66] A. C. Saez, J. C. Perfetti, and I. Rusinek. “Prediction of Effective Diffusivities in Porous Media using Spatially Periodic Models”. In: *Transport in Porous Media* 6 (1991), pp. 143–157 (cit. on pp. 17, 19, 22).

[67] M. Huysmans and A. Dassargues. “Equivalent diffusion coefficient and equivalent diffusion accessible porosity of a stratified porous medium”. In: *Transport in Porous Media* 66.3 (Feb. 2007), pp. 421–438 (cit. on pp. 17, 19, 22).

[68] D. M. Tartakovsky, M. Dentz, D. M. Tartakovsky, and M. Dentz. “Diffusion in porous media: phenomena and mechanisms”. In: *Transport in Porous Media* 130 (2019), pp. 105–127 (cit. on pp. 17, 19, 22).

[69] D. A. Mu Zhong-Sheng Liu AE Cheng Huang AE Ned Djilali. “Prediction of the effective diffusion coefficient in random porous media using the finite element method”. In: *Journal of Porous Materials* 14 (2007), pp. 49–54 (cit. on pp. 19, 20).

[70] H. L. Weissberg. “Effective Diffusion Coefficient in Porous Media Effective Diffusion Coefficient in Porous Media”. In: *Journal of Applied Physics* 34.9 (1963), p. 2636 (cit. on p. 20).

[71] J. R. Kalnin, E. A. Kotomin, and J. Maier. “Calculations of the effective diffusion coefficient for inhomogeneous media”. In: *Journal of Physics and Chemistry of Solids* 63.3 (Mar. 2002), pp. 449–456 (cit. on p. 20).

[72] E. J. Harris and G. P. Burn. “The transfer of sodium and potassium ions between muscle and the surrounding medium”. In: *Transactions of the Faraday Society* 45.0 (Jan. 1949), pp. 508–528 (cit. on p. 20).

[73] S. Katoch, S. S. Chauhan, and V. Kumar. “A review on genetic algorithm: past, present, and future”. In: *Multimedia Tools and Applications* 80.5 (Feb. 2021), p. 8091 (cit. on p. 24).

[74] B. Shahriari, K. Swersky, Z. Wang, R. P. Adams, and N. De Freitas. “Taking the human out of the loop: A review of Bayesian optimization”. In: *Proceedings of the IEEE* 104.1 (Jan. 2016), pp. 148–175 (cit. on p. 24).

[75] *ANSYS Theory Reference Manual.* ANSYS Inc., 2019 (cit. on p. 25).

[76] P. Teunissen. “Nonlinear least-squares”. In: *Manuscripta Geodaetica* 15 (Jan. 1990), pp. 137–150 (cit. on pp. 27, 46).

[77] M. A. Branch, T. F. Coleman, and Y. Li. “A Subspace, Interior, and Conjugate Gradient Method for Large-Scale Bound-Constrained Minimization Problems”. In: *SIAM Journal on Scientific Computing* 21.1 (July 2006), pp. 1–23 (cit. on pp. 30, 31).

[78] J. J. Moré. “The Levenberg-Marquardt algorithm: Implementation and theory”. In: *Numerical Analysis* (1978), pp. 105–116 (cit. on p. 30).

[79] P. Virtanen, R. Gommers, T. E. Oliphant, et al. “SciPy 1.0: fundamental algorithms for scientific computing in Python”. In: *Nature Methods* 17.3 (Feb. 2020), pp. 261–272 (cit. on p. 30).

[80] *ANSYS Element Reference Manual.* ANSYS Inc., 2019 (cit. on p. 32).

[81] A. Sottoriva, I. Spiteri, S. G. Piccirillo, et al. “Intratumor heterogeneity in human glioblastoma reflects cancer evolutionary dynamics”. In: *Proceedings of the National Academy of Sciences of the United States of America* 110.10 (2013), pp. 4009–4014 (cit. on p. 42).

[82] D. Givoli. “A tutorial on the adjoint method for inverse problems”. In: *Computer Methods in Applied Mechanics and Engineering* 380 (2021), p. 113810 (cit. on p. 44).

[83] K. Fang et al. “Convolutional neural network for accelerating the computation of the extended Tofts model in dynamic contrast-enhanced magnetic resonance imaging”. In: *Journal of Magnetic Resonance Imaging* 53.6 (June 2021), pp. 1898–1910 (cit. on p. 46).

[84] C. Ulas, G. Tetteh, M. J. Thrippleton, P. A. Armitage, S. D. Makin, J. M. Wardlaw, M. E. Davies, and B. H. Menze. "Direct estimation of pharmacokinetic parameters from DCE-MRI using deep CNN with forward physical model loss". In: *Lecture Notes in Computer Science* 11070 LNCS (2018), pp. 39–47 (cit. on p. 46).

[85] C. Ulas, D. Das, M. J. Thrippleton, M. d. C. Valdés Hernández, P. A. Armitage, S. D. Makin, J. M. Wardlaw, and B. H. Menze. "Convolutional Neural Networks for Direct Inference of Pharmacokinetic Parameters: Application to Stroke Dynamic Contrast-Enhanced MRI". In: *Frontiers in Neurology* 0.1 (2019), p. 1147 (cit. on p. 46).

[86] J. Zou, J. M. Balter, and Y. Cao. "Estimation of Pharmacokinetic Parameters from DCE-MRI by Extracting Long and Short Time-dependent Features Using an LSTM Network". In: *Medical physics* 47.8 (Aug. 2020), p. 3447 (cit. on p. 46).

[87] M. Raissi, P. Perdikaris, and G. E. Karniadakis. "Physics-informed neural networks: A deep learning framework for solving forward and inverse problems involving nonlinear partial differential equations". In: *Journal of Computational Physics* 378 (Feb. 2019), pp. 686–707 (cit. on pp. 46, 49–51, 83, 91).

[88] G. E. Karniadakis, I. G. Kevrekidis, L. Lu, P. Perdikaris, S. Wang, and L. Yang. "Physics-informed machine learning". In: *Nature Reviews Physics 2021 3:6* 3.6 (May 2021), pp. 422–440 (cit. on p. 46).

[89] J. Blechschmidt and O. G. Ernst. "Three ways to solve partial differential equations with neural networks — A review". In: *GAMM-Mitteilungen* 44.2 (June 2021), e202100006 (cit. on p. 46).

[90] T. Ottens, S. Barbieri, M. R. Orton, R. Klaassen, H. W. van Laarhoven, H. Crezee, A. J. Nederveen, X. Zhen, and O. J. Gurney-Champion. "Deep learning DCE-MRI parameter estimation: Application in pancreatic cancer". In: *Medical Image Analysis* 80 (Aug. 2022), p. 102512 (cit. on p. 46).

[91] R. L. van Herten, A. Chiribiri, M. Breeuwer, M. Veta, and C. M. Scannell. "Physics-informed neural networks for myocardial perfusion MRI quantification". In: *Medical Image Analysis* 78 (May 2022), p. 102399 (cit. on pp. 46, 49).

[92] B. Zapf, J. Haubner, M. Kuchta, G. Ringstad, P. K. Eide, and K. A. Mardal. "Supp. Material: Investigating molecular transport in the human brain from MRI with physics-informed neural networks". In: *Scientific Reports* 12.1 (2022), pp. 1–11 (cit. on p. 46).

[93] D. Shen, G. Wu, and H. I. Suk. "Deep Learning in Medical Image Analysis". In: *Annual review of biomedical engineering* 19 (June 2017), p. 221 (cit. on p. 47).

[94] H. Chen, O. Engkvist, Y. Wang, M. Olivecrona, and T. Blaschke. "The rise of deep learning in drug discovery". In: *Drug Discovery Today* 23.6 (June 2018), pp. 1241–1250 (cit. on p. 47).

[95] A. S. Lundervold and A. Lundervold. "An overview of deep learning in medical imaging focusing on MRI". In: *Zeitschrift für Medizinische Physik* 29.2 (May 2019), pp. 102–127 (cit. on p. 47).

[96] A. R. Luca, T. F. Ursuleanu, L. Gheorghe, R. Grigorovici, S. Iancu, M. Hlusneac, and A. Grigorovici. "Impact of quality, type and volume of data used by deep learning models in the analysis of medical images". In: *Informatics in Medicine Unlocked* 29 (Jan. 2022), p. 100911 (cit. on p. 47).

[97] S. Cuomo, V. S. Di Cola, F. Giampaolo, G. Rozza, M. Raissi, and F. Piccialli. "Scientific Machine Learning Through Physics–Informed Neural Networks: Where we are and What's Next". In: *Journal of Scientific Computing 2022 92:3* 92.3 (July 2022), pp. 1–62 (cit. on p. 47).

[98] K. Hornik, M. Stinchcombe, and H. White. "Multilayer feedforward networks are universal approximators". In: *Neural Networks* 2.5 (Jan. 1989), pp. 359–366 (cit. on p. 48).

[99] A. G. Baydin, B. A. Pearlmutter, A. A. Radul, and J. M. Siskind. *Automatic differentiation in machine learning: a survey*. 2018 (cit. on p. 48).

[100] M. Raissi, A. Yazdani, and G. E. Karniadakis. "Hidden Fluid Mechanics: A Navier-Stokes Informed Deep Learning Framework for Assimilating Flow Visualization Data". In: (2018) (cit. on p. 49).

[101] K. F. Iversen. *Informed Neural Networks for Inverse Advection-Diffusion Problems* (cit. on p. 49).

[102] X. Glorot and Y. Bengio. “Understanding the difficulty of training deep feedforward neural networks”. In: *Proceedings of the thirteenth international conference on artificial intelligence and statistics*. JMLR Workshop and Conference Proceedings. 2010, pp. 249–256 (cit. on p. 50).

[103] D. P. Kingma and J. Ba. *Adam: A Method for Stochastic Optimization*. 2017 (cit. on p. 50).

[104] M. Stein. “Large Sample Properties of Simulations Using Latin Hypercube Sampling”. In: *Technometrics* 29.2 (May 1987), p. 143 (cit. on p. 51).

[105] L. Lu, X. Meng, Z. Mao, and G. E. Karniadakis. “DeepXDE: A Deep Learning Library for Solving Differential Equations”. In: *SIAM Review* 63.1 (Feb. 2021), pp. 208–228 (cit. on pp. 51, 61).

[106] Y. Wang, X. Han, C.-Y. Chang, D. Zha, U. Braga-Neto, and X. Hu. *Auto-PINN: Understanding and Optimizing Physics-Informed Neural Architecture*. 2022 (cit. on p. 61).

[107] S. Wang, Y. Teng, and P. Perdikaris. “Understanding and mitigating gradient flow pathologies in physics-informed neural networks”. In: *SIAM Journal on Scientific Computing* 43.5 (2021), pp. 3055–3081 (cit. on p. 61).

[108] C. Xu, B. T. Cao, Y. Yuan, and G. Meschke. “Transfer learning based physics-informed neural networks for solving inverse problems in engineering structures under different loading scenarios”. In: *Computer Methods in Applied Mechanics and Engineering* 405 (Feb. 2023), p. 115852 (cit. on p. 61).

[109] K. Weiss, T. M. Khoshgoftaar, and D. D. Wang. “A survey of transfer learning”. In: *Journal of Big Data* 3.1 (Dec. 2016), pp. 1–40 (cit. on p. 61).

[110] D. Sainz-DeMena, J. Manuel García-Aznar, M. Ángeles Pérez, and C. Borau. “Im2mesh: A Python Library to Reconstruct 3D Meshes from Scattered Data and 2D Segmentations, Application to Patient-Specific Neuroblastoma Tumour Image Sequences”. In: *Applied Sciences 2022* 12.22 (Nov. 2022), p. 11557 (cit. on p. 63).

[111] L. H. Goetz and N. J. Schork. “Personalized medicine: motivation, challenges, and progress”. In: *Fertility and sterility* 109.6 (June 2018), pp. 952–963 (cit. on p. 64).

[112] M. Koenigkam Santos, J. Raniery Ferreira Júnior, D. Tadao Wada, A. Priscilla Magalhães Tenório, M. Henrique Nogueira Barbosa, and P. Mazzoncini De Azevedo Marques. "Artificial intelligence, machine learning, computer-aided diagnosis, and radiomics: advances in imaging towards to precision medicine". In: *Radiologia Brasileira* 52.6 (Nov. 2019), p. 387 (cit. on p. 64).

[113] B. Grignon, L. Mainard, M. Delion, C. Hodez, and G. Oldrini. "Recent advances in medical imaging: anatomical and clinical applications". In: *Surgical and radiologic anatomy : SRA* 34.8 (Oct. 2012), pp. 675–686 (cit. on p. 64).

[114] A. Sturchio, L. Marsili, A. Mahajan, M. B. Grimberg, M. A. Kauffman, and A. J. Espay. "How have advances in genetic technology modified movement disorder nosology?" In: *European journal of neurology* 27.8 (Aug. 2020), pp. 1461–1470 (cit. on p. 64).

[115] F. Merino-Casallo, M. J. Gomez-Benito, Y. Juste-Lanas, R. Martinez-Cantin, and J. M. Garcia-Aznar. "Integration of in vitro and in silico Models Using Bayesian Optimization With an Application to Stochastic Modeling of Mesenchymal 3D Cell Migration". In: *Frontiers in physiology* 9.9 (Sept. 2018) (cit. on p. 64).

[116] M. Hadjicharalambous, P. A. Wijeratne, and V. Vavourakis. "From tumour perfusion to drug delivery and clinical translation of in silico cancer models". In: *Methods (San Diego, Calif.)* 185 (Jan. 2021), pp. 82–93 (cit. on p. 64).

[117] E. A. Lima, D. Faghihi, R. Philley, J. Yang, J. Virostko, C. M. Phillips, and T. E. Yankeelov. "Bayesian calibration of a stochastic, multiscale agent-based model for predicting in vitro tumor growth". In: *PLOS Computational Biology* 17.11 (Nov. 2021), e1008845 (cit. on p. 64).

[118] S. Angeli, K. E. Emblem, P. Due-Tonnessen, and T. Stylianopoulos. "Towards patient-specific modeling of brain tumor growth and formation of secondary nodes guided by DTI-MRI". In: *NeuroImage: Clinical* (2018) (cit. on p. 64).

[119] A. M. Jarrett, D. A. Hormuth, S. L. Barnes, X. Feng, W. Huang, and T. E. Yankeelov. "Incorporating drug delivery into an imaging-driven, mechanics-coupled reaction diffusion model for predicting the response of breast cancer to neoadjuvant chemotherapy: Theory and preliminary clinical results". In: *Physics in Medicine and Biology* 63.10 (May 2018) (cit. on p. 64).

[120] M. Gabelloni, L. Faggioni, R. Borgheresi, G. Restante, J. Shortrede, L. Tumminello, C. Scapicchio, F. Coppola, D. Cioni, I. Gómez-Rico, L. Martí-Bonmatí, and E. Neri. "Bridging gaps between images and data: a systematic update on imaging biobanks". In: *European radiology* 32.5 (May 2022), pp. 3173–3186 (cit. on p. 64).

[121] J. Li, M. Erdt, F. Janoos, T.-c. Chang, and J. Egger. "Medical image segmentation in oral-maxillofacial surgery". In: *Computer-Aided Oral and Maxillofacial Surgery*. Ed. by J. Egger and X. Chen. Academic Press, 2021, pp. 1–27 (cit. on p. 65).

[122] H. Wang, P. Prasanna, and T. Syeda-Mahmood. "Rapid annotation of 3D medical imaging datasets using registration-based interpolation and adaptive slice selection". In: *Proceedings - International Symposium on Biomedical Imaging* 2018-April (May 2018), pp. 1340–1343 (cit. on p. 65).

[123] S. Ravikumar, L. Wisse, Y. Gao, G. Gerig, and P. Yushkevich. "Facilitating manual segmentation of 3d datasets using contour and intensity guided interpolation". In: *Proceedings - International Symposium on Biomedical Imaging* 2019-April (Apr. 2019), pp. 714–718 (cit. on p. 65).

[124] R. Wang, T. Lei, R. Cui, B. Zhang, H. Meng, and A. K. Nandi. "Medical Image Segmentation Using Deep Learning: A Survey". In: *IET Image Processing* 16.5 (Sept. 2020), pp. 1243–1267 (cit. on p. 65).

[125] O. Ronneberger, P. Fischer, and T. Brox. "U-Net: Convolutional Networks for Biomedical Image Segmentation". In: *IEEE Access* 9 (May 2015), pp. 16591–16603 (cit. on p. 65).

[126] A. B. Albu, T. Beugeling, and D. Laurendeau. "A morphology-based approach for interslice interpolation of anatomical slices from volumetric images". In: *IEEE Transactions on Biomedical Engineering* 55.8 (Aug. 2008), pp. 2022–2038 (cit. on p. 65).

[127] C. Zhao, Y. Duan, and D. Yang. "A Deep Learning Approach for Contour Interpolation". In: *Proceedings - Applied Imagery Pattern Recognition Workshop* (2021) (cit. on p. 65).

[128] A. Fedorov et al. "3D Slicer as an image computing platform for the Quantitative Imaging Network". In: *Magnetic resonance imaging* 30.9 (Nov. 2012), pp. 1323–1341 (cit. on pp. 65, 70, 77).

[129] L. Martí-Bonmatí et al. “PRIMAGE project: predictive in silico multiscale analytics to support childhood cancer personalised evaluation empowered by imaging biomarkers”. In: *European radiology experimental* 4.1 (Dec. 2020) (cit. on p. 65).

[130] C. Scapicchio, M. Gabelloni, S. M. Forte, L. C. Alberich, L. Faggioni, R. Borgheresi, P. Erba, F. Paiar, L. M. Bonmati, and E. Neri. “DICOM-MIABIS integration model for biobanks: a use case of the EU PRIMAGE project”. In: *European Radiology Experimental* 5.1 (Dec. 2021), pp. 1–12 (cit. on p. 65).

[131] G. Bradski. “The OpenCV library”. In: *Dr. Dobb’s Journal* 25.11 (2000), pp. 120–125 (cit. on pp. 67, 68).

[132] A. Schenk, G. Prause, and H. O. Peitgen. “Efficient semiautomatic segmentation of 3D objects in medical images”. In: *Lecture Notes in Computer Science* 1935 (2000), pp. 186–195 (cit. on p. 68).

[133] P. Cignoni, M. Callieri, M. Corsini, M. Dellepiane, F. Ganovelli, and G. Ranzuglia. “MeshLab: an Open-Source Mesh Processing Tool”. In: *Eurographics Italian Chapter Conference*. Ed. by V. Scarano, R. De Chiara, and U. Erra. The Eurographics Association, 2008, pp. 129–136 (cit. on p. 68).

[134] R. Bridson. “Fast poisson disk sampling in arbitrary dimensions”. In: *ACM SIGGRAPH* (2007) (cit. on p. 68).

[135] M. Kazhdan and H. Hoppe. “Screened poisson surface reconstruction”. In: *ACM Transactions on Graphics* 32.3 (July 2013) (cit. on p. 68).

[136] M. Garland and P. S. Heckbert. “Surface simplification using quadric error metrics”. In: *Proceedings of the 24th Annual Conference on Computer Graphics and Interactive Techniques* (Aug. 1997), pp. 209–216 (cit. on p. 68).

[137] J. Vollmer, R. Mencl, and H. Müller. “Improved Laplacian Smoothing of Noisy Surface Meshes”. In: *Computer Graphics Forum* 18.3 (Sept. 1999), pp. 131–138 (cit. on p. 68).

[138] C. Geuzaine and J. F. Remacle. “Gmsh: A 3-D finite element mesh generator with built-in pre- and post-processing facilities”. In: *International Journal for Numerical Methods in Engineering* 79.11 (Sept. 2009), pp. 1309–1331 (cit. on p. 70).

[139] P. M. Knupp, C. Ernst, D. C. Thompson, C. Stimpson, and P. P. Pebay. *The verdict geometric quality library*. Albuquerque, NM, and Livermore, CA (United States), Mar. 2006 (cit. on pp. 70, 72).

[140] N. C. Atuegwu, L. R. Arlinghaus, X. Li, A. Chakravarthy, V. Abramson, M. Sanders, and T. Yankeelov. “Parameterizing the logistic model of tumor growth by DW-MRI and DCE-MRI data to predict treatment response and changes in breast cancer cellularity during neoadjuvant chemotherapy”. In: *Translational Oncology* 6.3 (2013), pp. 256–264 (cit. on p. 71).

[141] P. Virtanen et al. “SciPy 1.0: fundamental algorithms for scientific computing in Python”. In: *Nature Methods* 17.3 (Feb. 2020), pp. 261–272 (cit. on p. 71).

[142] T. F. De Moraes, P. H. J. Amorim, F. Azevedo, and J. V. L. da Silva. “InVesalius—An open-source imaging application”. In: *World Journal of Urology* 30 (2012), pp. 687–691 (cit. on p. 77).

[143] Scientific Computing and Imaging Institute (SCI). *Seg3D: Volumetric Image Segmentation and Visualization*. 2016 (cit. on p. 77).

[144] V. Lukeš. *dicom2fem*. 2014 (cit. on p. 78).

[145] V. Lukeš, M. Jiřík, A. Jonášová, E. Rohan, O. Bublík, and R. Cimrman. “Numerical simulation of liver perfusion: from CT scans to FE model”. In: *Proceedings of the 7th European Conference on Python* (2014), p. 79 (cit. on p. 78).